UC Berkeley
UC Berkeley Electronic Theses and Dissertations

Title

Thermal Radiation Modulation Structures Based on Vanadium Dioxide

Permalink

https://escholarship.org/uc/item/19k3653m

Author

Li, Jiachen

Publication Date

2022

Peer reviewed|Thesis/dissertation

eScholarship.org Powered by the California Digital Library
University of California

Thermal Radiation Modulation Structures Based on Vanadium Dioxide

By

Jiachen Li

A dissertation submitted in partial satisfaction of the

requirements for the degree of

Doctor of Philosophy

in

Engineering – Applied Science and Technology

in the

Graduate Division

of the

University of the California, Berkeley

Committee in charge:

Professor Junqiao Wu, Chair

Professor Jie Yao

Professor Van P. Carey

Fall 2022

Thermal Radiation Modulation Structures Based on Vanadium Dioxide

Copyright © 2022 by Jiachen Li. All Rights Reserved.

Abstract

Thermal Radiation Modulation Structures Based on Vanadium Dioxide

By

Jiachen Li

Doctor of Philosophy in Engineering – Applied Science and Technology

University of California, Berkeley

Professor Junqiao Wu, Chair

Thermal Radiation is intrinsic emission of electromagnetic waves from all matter that has a temperature greater than zero Kelvin. In the past decades, many applications related to thermal radiation have been studied and developed. However, most of these applications are based on materials with static emissivity, which is limited to the range from 0 to 1. Due to the fast development of material science and fabrication techniques, the emissivity of latest thermal infrared (IR) materials is already very close to unity. Thus, thermal performance with constant emissivity is saturated. In recent years, thermal radiation modulation materials have opened a new page in thermal radiation research and applications by breaking the performance limit and overcoming the intrinsic disadvantages of conventional, constant-emissivity materials. In this dissertation, multiple innovative thermal radiation modulation materials and structures based on the phase transition material, vanadium dioxide, are presented.

For thermography applications, infrared (IR) camera reads the surface temperature by assuming a constant high emissivity (~0.9) of the target objects. Thus, if the emissivity of the target is different from 0.9, IR camera will be deceived, and the temperature readout (T_{IR}) will differ from the real surface temperature (T_s). In chapter 2-3, we demonstrate that by modulating the emissivity, we can achieve novel T_{IR}- T_s relations which enable applications that are impossible with conventional materials. By modulating the emissivity to nearly $1/T^4$ dependence with graded W-doping in VO_2 thin films, we achieve a temperature-insensitive T_{IR} at different values over a wide temperature range. The T-insensitive T_{IR} can be utilized for IR camouflage and IR decoy applications. We also develop a thermal imaging sensitizer (TIS) that has sharp emissivity increase during the phase transition of W-doped vanadium oxide ($W_xV_{1-x}O_2$). The resultant high dT_{IR}/dT_s can bring more than 15 times of enhancement to the sensitivity of conventional IR cameras. The TIS may find its applications in electronics, building construction and medical diagnostics.

In chapter 4-5, we discuss our research effort on energy-saving in building temperature regulations. As the emissivity of conventional cool roof materials has reached the physical limit in recent years, we further improved the energy saving potential by developing a temperature-adaptive radiative coating (TARC) with switchable emissivity. TARC acts as a high-emittance radiative cooler coating at (and only at) high temperatures, while retaining heat under the surface at low temperatures. Simulations and experiments showed that the TARC may outperform all conventional roof materials in terms of cutting energy consumption for households.

To tackle the critical problems of the building application of TARC, such as scalability, durability and color tunability, we explore a scalable temperature-adaptive radiative coating (STARC) produced with a roll-to-roll method. With the new polymer-based structure, STARC have lower cost and longer lifetime. Moreover, the color of STARC can be tuned with IR-transparent pigments for the needs of aesthetic and solar absorption optimization. A field with carefully designed mock-up houses directly proved the temperature regulation ability of STARC. The application of STARC and TARC can also be expanded to a wider scope, such as tents, vehicles, clothes, space objects and mobile electronics.

Table of Contents

List of Figures ..... **vi**

List of Tables ..... **xiv**

Acknowledgements ..... **xv**

1. Introduction **1**

1.1. Thermal Radiation: Physics and Applications 1

1.1.1. Physics of Thermal Radiation 1

1.1.2. Applications Related to Thermal Radiation 3

1.2. Physical Properties of the Phase-Transition Material Vanadium Dioxide (VO_2) 4

1.3. Outline of the Dissertation 5

2. Thermal Radiation Modulation of Graded Tungsten-Doped VO_2 Films **6**

2.1. Introduction 6

2.2. Design and Preparation of the Multilayer Structure 8

2.3. Numerical Simulation of the Emissivity 10

2.4. Modulation of Thermal Radiation Power: Two Unique Functions 11

2.4.1. IR camouflage 11

2.4.2. IR decoy 15

2.5. Summary 17

3. Thermal Imaging Sensitizer (TIS) Driven by the Metal-Insulator Transition of VO_2 ..... **18**

3.1. Introduction 18

3.2. Structural Design and Characterization of TIS 20

3.2.1. Working Principle of the ε Switching 20

3.2.2. Fabrication 20

3.2.3. Setup of IR Camera Measurements 21

3.2.4. IR camera Characterization 22

3.2.5. Robustness Against Viewing Direction and Nonuniformity 25

3.3. Operando Electronics Analysis (oEA) Applications 26

3.3.1. Thermography for Integrated Circuit Packages 27

3.3.2. Electric Operation Parameters Probing 29
3.4. Medical Thermography 32
3.4.1. Cancer Screening 32
3.4.2. Experimental Details for in Vivo Tumor Growth 33
3.4.3. More on Medical Thermography 34
3.5. Summary 35

4. Temperature-adaptive Radiative Coating (TARC) for Year-round Energy Saving 36
4.1. Introduction 36
4.1.1. Cool Roofs and Their Limitations 36
4.1.2. Solutions to the Overcooling 37
4.2. Working Principle of TARC 38
4.3. Fabrication Process 39
4.4. Experimental Characterizations 40
4.4.1. Spectrally Resolved Absorptance/Emissivity Measurements 40
4.4.2. Cooling Power Measurement 41
4.5. Outdoor Demonstration of Thermal Regulation Performance of TARC 43
4.6. Energy Saving Potential of TARC by EnergyPlus simulation 46
4.6.1. Surface Temperature Simulation 47
4.6.2. Energy Saving Comparison Between TARC and Conventional Materials 49
4.6.3. Example: Energy Saving Performance of TARC in Baltimore, MD 49
4.7. Conclusion and Remarks 50

5. Scalable Temperature Adaptive Radiative Coating (STARC) with Optimized Solar Absorption 52
5.1. Challenges for the Applications of Thermal Radiation Modulation Materials 52
5.2. Design of STARC and Manufacturing Process 52
5.2.1. Structure Design of STARC 53
5.2.2. Design of the Production Line for STARC 55
5.2.3. Fabrication of the Reusable Imprinting Template 55
5.3. Colored Variations of STARC for Optimal Solar Absorption 56
5.4. Field Test with a Mock-Up of Residential House 57
5.4.1. Experimental Setup 57

5.4.2. Result of the Field Test 58
5.5. Conclusion and Remarks 59

6. Summary and Outlook 60
6.1. Future works 60
6.1.1. Improvement of current devices 60
6.1.2. Broader applications and research directions 61

Appendix 62
A.1. Estimation of space-heating source energy saving ($\mathbf{\Delta}S_h$) and space cooling source energy saving (ΔS_c) 62
A.2. Space-conditioning source energy savings of TARC across the U.S. 64
A.3. Coefficients Used in EnergyPlus Calculation 65
A.4. Schematic illustration of the manufacturing process for a STARC. 69
A.5. schematic illustration of the manufacturing process of the imprint template. 70

References 71

List of Figures

Figure 1.1. Hemispherical spectral emissive power B(λ, T) of a blackbody at different temperatures. 1

Figure 1.2. (a) Crystal structure of the low-temperature monoclinic insulating phase and high-temperature rutile metallic phase of VO_2 [15]. (b) Refractive index, n and extinction coefficient, k of a 40nm thick VO_2 film as a function of wavelength measured at 300K and 373K [16]. 4

Figure 2.1. Engineering thermal IR emissivity by grading metal (M)–insulator (I) transition. (a) Schematic illustrating the temperature dependence of integrated emissivity (ε_{int}) within the shaded area using graded W-doped VO_2. Three arbitrarily designed emissivity curves are denoted by i, ii, and iii. The behavior of typical materials is also shown for comparison. (b) Spectral emissivity of a graded $W_xV_{1-x}O_2$ structure (schematic in inset) measured over a broad range of temperatures. The solid and dashed curves correspond to data collected during heating and cooling, respectively. (c) Design of W doping profile x(Z) (dashed line, left-bottom axes) to generate the desired $\varepsilon_{int}(T)$ relation (solid line, right-top axes). The boxes represent the actual nominal doping profile used in the $W_xV_{1-x}O_2$ film deposition, and the data points are the experimentally measured $\varepsilon_{int}(T)$ from this film. (d) Schematic showing that by rational design of the W doping profile (x along thickness direction) of $W_xV_{1-x}O_2$, emissivity can be programmed to regulate thermal radiation (P_{rad}) for distinctly different behavior from the T^4 law. 7

Figure 2.2. Thickness measurements and doping profile characterization of VO_2 films. The VO_2 film was deposited on a sapphire substrate by PLD, and then patterned by photolithography and selective dry etching. (a) The thickness of VO_2 extracted from the step heights in the surface line profiles of AFM. Given the deposition time of 90 mins, the result indicates a growth rate of ~ 2.0 nm/min. Similar deposition rate was obtained for $W_xV_{1-x}O_2$ films, with x ranging from 0 to 3.0%. (b) A cross section view of a graded $W_xV_{1-x}O_2$ film by SEM. (c) Depth profile of W fraction (x) across the thickness of a multilayer, obtained by XPS with controlled sputtering. The gradual change of W fraction across different layers supports the smoothly graded W-doped structure of $W_xV_{1-x}O_2$. 9

Figure 2.3. Schematics of the process to transfer $W_xV_{1-x}O_2$ onto a flexible PE tape. $W_xV_{1-x}O_2$ thin films grown on quartz substrates were transferred to PE tapes by sticking the $W_xV_{1-x}O_2$ side to the adhesive tape, and then etching off the 170 μm thick quartz substrate by dipping in 49% Hydrofluoric (HF) acid for 5 mins. The samples with transferred $W_xV_{1-x}O_2$ were then rinsed in deionized water for 3 mins and gently blown dry with a N2 gun. 10

Figure 2.4. (a) Resistance-temperature data of uniformly doped $W_xV_{1-x}O_2$ thin films with different W fractions, measured by standard four-probe method. The abrupt drop in resistivity occurs at the T_{MIT} of each film. The resistance of a graded doped $W_xV_{1-x}O_2$ film (red curve) is also plotted for comparison, showing that its MIT is spread over a wide temperature range. The lack of kinks and abrupt changes in the electrical sheet resistance of the multilayer indicates that it becomes a

smoothly graded W-doped structure. (b) Numerical simulation of three graded $W_xV_{1-x}O_2$ samples on PE tape. The symbols are experimental data, and the lines correspond to best-fit results. 11

Figure 2.5. Mechanically flexible, power-free, and ∇T- and dT/dt-immune camouflage based on the graded $W_xV_{1-x}O_2$. (a) Schematic illustrating constant thermal radiance over a wide range of temperature from the camouflage, in stark contrast to the Stefan–Boltzmann T^4 law from conventional materials. (b) Thermal radiance and integrated emissivity of the film as a function of temperature, showing that the negative temperature coefficient of emissivity counteracts the T^4 law to yield a temperature-independent thermal radiation power. The solid and dashed curves are for measurements during heating and cooling, respectively. (c) Optical image of a graded $W_xV_{1-x}O_2$ film transferred onto a PE tape showing high mechanical flexibility. The visible color of the sample is related to the $W_xV_{1-x}O_2$ thickness and lighting on surface. The fingertip is hidden from the IR camera when covered with the camouflage. (d) Camouflaging an object with large spatial temperature variation from ≈25 to 65 °C, showing immunity to ∇T. (e) Camouflaging an object with drastic temperature surge, showing immunity to dT/dt. As shown in (f), the actual temperature of the camouflage (represented by the IR temperature of the control that is a high-emissivity tape placed near the sample) rises rapidly by the heating pulse, while the IR temperature of the camouflage stays nearly flat. The IR temperature was measured by averaging the camera reading in the center 1 × 1 cm^2 region of each film (dashed boxes), and the error bars are comparable to the symbols in size. 13

Figure 2.6. Reliability test for graded $W_xV_{1-x}O_2$ camouflage. (a). A high emissivity coating (control) and our graded $W_xV_{1-x}O_2$ camouflage attached to each side of a wing-shape heater, which ramps the temperature between ~15 °C and ~65°C with cycles of 40s. (b). An IR image during the temperature ramping. The black box and red box denote the region where IR temperature measurements are averaged for the control and sample, respectively. c. Measured IR temperature for control and sample over cycles 0-5 compared to cycles 100-105. The IR camouflage performance shows no degradation after over 100 heating/cooling cycles through the working temperature range..... 14

Figure 2.7. Demonstration of temperature-independent thermal IR decoy. (a) IR temperature (T_{IR}) versus actual temperature (T) of five flexible structures, where the graded $W_xV_{1-x}O_2$ configuration is designed to yield T-independent, but different values of desired T_{IR} within the working range of T. Details of these samples are shown in Table 2.4.The error bars are comparable to the symbols in size. (b) Optical and (c) IR images, using the samples 1, 3, and 5, respectively. A pattern of "CAL" is made to show "C" at constant T_{IR} ≈ 5 °C, "A" at T_{IR} ≈ 15 °C, and "L" at T_{IR} ≈ 25 °C, regardless of T varying to 65, 50, or 35 °C. The three samples are all 1 × 1 cm^2 in size. 15

Figure 2.8. A monolithic decoy prepared by encoding the decoy pattern during the film deposition, by adding an extra layer of $W_{0.03}V_{0.97}O_2$ in areas that need colder IR temperature (T_{IR} = 10 - 15ºC), while the rest is designed to be at higher T_{IR} = 25 - 30ºC. The performance shows the T-independent T_{IR} images consistent with the design. 16

Figure 2.9. Normal-incidence spectral reflectance from 2 μm to 16 μm measured by FTIR of a graded doped $W_xV_{1-x}O_2$ film transferred onto the PE tape. The sample is the sample 3 in Table 2.4. 17

Figure 3.1. Roadmap of NEDT for state-of-the-art commercial uncooled bolometers [41-44]. Little advance was made in the past two decades, with the value currently saturated at 20 -40 mK. The working bandwidth is 20 –60 Hz. 18

Figure 3.2. Thermal imaging sensitized by MIT. (a) Schematic illustration of boosted temperature resolution of thermography by the thermal imaging sensitizer (TIS) and its working mechanism. As the object (covered with TIS) is heated up across the MIT, the TIS switches from a reflector (hence, low absorbance and low emissivity) in the insulating (I) phase to a resonator (hence, high absorbance and high emissivity) in the metallic (M) phase for mid-IR waves. (b) In contrast to conventional materials or black body, the sharp increase in thermal emissivity (ε) at the MIT of $W_xV_{1-x}O_2$ introduces a high amplification (>15) of ΔT to ΔT_{IR} and thus reduction in NEDT. (c) Representative temperature resolution required for ambient thermography in various applications with paradigmatic feature sizes. TIS pushes boundaries of these applications and generates new markets. 19

Figure 3.3. Schematics and picture for the fabrication of the TIS. 20

Figure 3.4. Schematics for the setups to minimize impact of IR signals from surrounding environment to optimize sensitizing effects. (a) Schematic and equations to demonstrate the impact of environmental radiation, which is denoted as S_{env}. (b) Setups to minimize the impact from S_{env}, either by doing the experiment in an outdoor environment with a clear sky or using a "cold ceiling" setup. The "cold ceiling" is made by a ~1 mm thick copper plate with high-emissivity coating facing the target object and cooled by cryogen such as dry ice. These two setups were applied throughout the IR camera measurement in this work and were comparable in the effect of optimizing sensitizing performance. 21

Figure 3.5. (a) Optical image of a fabricated TIS, showing high flexibility. (b) False-colored cross section of the TIS film imaged by scanning electron microscopy (SEM) before transfer. (c) IR temperature and temperature amplification as a function of actual temperature for TIS with three selected compositions (fractions of W in the $W_xV_{1-x}O_2$ layer). (d) Schematics and directly captured IR images of two closely placed (1-mm gap) small heaters imaged without and with TIS. (e) Calibrated temperature profiles along the dashed lines in (d). The twin-heater feature is distinctly resolved in the TIS-assisted imaging because of the ~15 times improvement of the experimental thermal sensitivity. 22

Figure 3.6. Emissivity of TIS measured by Fourier-transform infrared spectroscopy (FTIR) and the IR camera. (a) Spectral emissivity of a TIS measured by FTIR at different temperatures. An abrupt increase of emissivity is observed when the temperature increases above 35 °C, which is the metal-insulator transition (MIT) temperature of the $W_xV_{1-x}O_2$ (x = 1.3%) in this TIS. (b) The

integrated emissivity over the 8-14 μm wavelengths (air transparency window) from the FTIR results, together with the results directly obtained by the IR camera. The higher emissivity extracted from the IR camera measurement is probably caused by signals contributed from environmental radiation, which is minimized but cannot be completely eliminated in the experiments (similar minimization effect between the outdoor and the cold ceiling setup). 23

Figure 3.7. Improvement of IR imaging on a general thermal gradient by TIS. (a) Schematic and IR image of a high-emissivity coating (w/o TIS) placed next to a TIS film (with TIS) on a surface with known temperature gradient. Note that the "w/o TIS" and "with TIS" areas have the same real temperature gradient. (b) Temperature profile on the surface by IR imaging without TIS, with TIS, and locally read by platinum resistance temperature detectors (Heraeus Sensor Technology). The Pt thermocouples readouts served as verification of the temperature gradient in IR images. TIS enables much finer measurement of the temperature distribution, eliminating the artificial step feature caused by the experimental IR camera sensitivity limit (~ 45 mK). 24

Figure 3.8. IR temperature (T_{IR}) as a function of real temperature (T) for two TIS samples imaged from different angles. (a) IR images of the two TIS samples with x = 1.5% and x = 1.3% in the $W_xV_{1-x}O_2$ layer, taken from different viewing angles. (b)-(c) T_{IR} (viewed from different angles) plotted as a function of T for the TIS with x = 1.5% and x = 1.3%, showing angular independence of the $T_{IR}(T)$ curves. 25

Figure 3.9. Temperature calibration for a TIS with significant defects and nonuniformity. (a) Actual temperature profile (obtained by conventional IR imaging) and an IR image assisted by a defective TIS of a surface with a rod-shaped thermal feature. (b) Collection of reference images for temperature calibration. Note that only a part of the sampled T_{IR} images was presented in this panel for simplicity. (c) Calibration result. 26

Figure 3.10. (a) Enhancement of thermographic contrast on a processor by TIS, allowing differentiation of various working modes. (b) Maximal surface temperature of the processor unit as a function of the working frequency measured in (a). 27

Figure 3.11. A SPDT switching chip with various input currents, imaged without and with TIS. Imaging with TIS coating enables accurate observation and detailed evaluation of vague thermal profile on the chip caused by weak Joule heating that are otherwise undetectable. 28

Figure 3.12. (a) Optical and IR mappings of temperature rise because of currents flowing in adjacent circuit traces on a printed circuit board (PCB), imaged without and with TIS. (b) Extracted current versus real current in the traces. The dashed line and the shadow correspond to the ideal current extraction and ±10% deviation, respectively. The experimental error bars for the data points are comparable to the size of the points. (c) Cross-sectional view of the model with partial geometric parameters used in the simulation. The total thickness of the polymer layer (representing scotch tape, glue, soldermask, etc.) is calculated based on the individual thickness of each material.

The copper traces are 35 μm thick and 0.5 mm wide, with a 0.5 mm gap between adjacent traces. 29

Figure 3.13. Calibration of the model based on thermal profiles of a single circuit trace, and extraction of the currents for 3-trace heating experiments. (a) Optical and IR images of current flowing through a single trace in PCB (IR images were taken with TIS coating). (b) Comparison between simulated and experimental thermal profiles in Y-direction. Note that the experimental thermal profiles were obtained by averaging over the X-direction through the IR images shown in (a). (c) IR images for three different experiments without and with TIS. (d). Representative current extraction in those three traces by fitting the simulated thermal profile to the experimental results. 31

Figure 3.14. TIS applied to cancer screening. (a) RMA cells were injected at two adjacent spots to initiate the tumor growth in mice, which was then tracked by optical imaging, IR imaging without TIS, and with TIS. (b) TIS imaging reveals the two tumors in early stage after the injection when they are not yet detectable visibly or by conventional thermography. The white curves are temperature profiles across the center of the two tumors in each IR image, labeled with the amplitude of T_{IR} variation in each curve..... 32

Figure 3.15. Supplementary results for the enhancement of IR imaging of tumors in mice. (a) Imaging of a tumor induced by injecting B16-F10 cells, which is a melanoma cell line distinct from the type applied in Figure 3.14. TIS demonstrates similar advantages in detecting tumors earlier than conventional IR imaging. (b) Imaging of three RMA tumors injected close to each other. Due to the limit of sensitivity, conventional IR imaging is unable to resolve those three tumors, while they can be distinguished clearly with the help of TIS. 33

Figure 3.16. Imaging of cephalic veins on a human forearm without and with TIS. The IR image of the crossing point of veins is enhanced by over 10× in IR temperature contrast by the TIS coating. 34

Figure 4.1. Atmospheric window. The upper panel showed the intensity of the thermal radiation exchange between the earth and outer space, including the solar radiation (incoming) and thermal radiation of terrestrial objects (outgoing). The lower panel shows the absorptance of atmosphere. The low-absorptance wavelength ranges are called atmospheric window [89]. 36

Figure 4.2. Basic property of TARC in sky-window (8 to 13mm) emissivity modulation and schematics for temperature management when used as a household roof coating. The data points are the measured sky-window emissivitys of a TARC. The two-color bands represent the temperature-independent thermal emissivity of metals and radiative coolers. 37

Figure 4.3. (a) Schematics of the structure (i), materials composition and working mechanism (ii and iii) of the TARC. Subpanels (iv) and (v) show the simulated distribution of electric field intensity below and above the transition temperature, respectively, when electromagnetic waves

with a wavelength of 7.8mm were normally incident on the TARC structure. (b) Photograph (2 cm × 2 cm) and false color scanning electron microscope image of TARC showing high flexibility and structural consistency with the design. (c) Thermal infrared images of TARC compared with those of two conventional materials (references) with constantly low or high thermal emissivity showing the temperature-adaptive switching in thermal emissivity of TARC. (d) Solar spectral absorptance and part of the thermal spectral emissivity of TARC at a low temperature and a high temperature, measured by a UV-visible-NIR spectrometer with an integrating sphere and an FTIR spectrometer, respectively. Measurements (solid curves) show consistency with COMSOL simulations (dashed curves). The arrow at 7.8mm denotes the wavelength where the distribution of electric field intensity shown in subpanels (iv) and (v) of (a) are simulated..... 38

Figure 4.4. Schematics and pictures for the fabrication of TARC..... 40

Figure 4.5. Detailed infrared spectra of TARC by Fourier transform infrared (FTIR) spectroscopy over the metal-insulator transition of $W_xV_{1-x}O_2$ (x=1.5%). (a) Spectral emissivity of TARC at temperatures ranging from 15 °C to 30 °C (ramp-up branch). The dashed box bounds the sky window (8-13 μm). (b) Sky-window emissivity as a function of TARC surface temperature, including both the ramp-up and ramp-down branches. 41

Figure 4.6. Characterization of intrinsic radiative cooling power of TARC in a cryogenic vacuum chamber. (a) Schematics of the experimental setup showing a thin heater membrane covered by either a TARC or an Al foil and suspended in a cryogen-cooled vacuum chamber. The Al foil reference is used to cancel the effect of thermal loss through conduction. (b) Calibrated experimental cooling flux (power/area) of TARC as a function of temperature in vacuum (the black data line). Fitting of $P_{cool}''(T)$ at I and M states by the Stefan-Boltzmann radiation law gives ε_w values of 0.20 and 0.90, respectively. 42

Figure 4.7. Characterization of TARC in an outdoor environment. (a) Schematic showing structure, geometry, and materials of the experimental setup. Identical 4 cm × 4 cm copper plates covered with different coatings were suspended by thin cotton strings (< 1 mm in diameter) in a cardboard box. A white paper mask was placed on top of the strings to minimize undesirable thermal artifacts from solar heating. (b) Solar absorption and sky-window IR emissivity of the measured material surfaces. (c) A photo of the actual experiment setup. (d) Schematic showing the solar shield used to block the direct solar radiation on the samples after 14:00 LDT. (e) Surface temperature of a TARC, a commercial dark roof coating ($A = 0.70$, $\varepsilon w = 0.90$), and a commercial white roof coating ($A = 0.15$, $\varepsilon w = 0.90$) in an open-space outdoor environment recorded over a day-night cycle. The solid and dashed curves are experimental data and simulation results based on a local weather database, respectively. Measurements starting from 14:00 local daylight time (LDT) were performed with the direct solar radiation blocked. Temperature observed after sunset show a clear sign of the TARC shutting off thermal radiative cooling as its surface ambient temperature falls below T_{MIT}. (f) Measured ambient cooling power of TARC and white roof coating with direct solar radiation blocked in the outdoor environment. 44

Figure 4.8. Simulation of the surface temperature of a dark roof coating, TARC, and a white roof coating (the same three samples as those in Figure 4.7 in four seasons in Berkeley, California (37.91°N, 122.28°W). The ambient temperature data (green curves) are directly exported from the climate database used for the simulation (Details in subsection 4.6.1). The only condition where the white roof coating has an advantage over the TARC in energy saving is the daytime in summer (b), while for almost all other conditions (all night times, daytime in spring, winter, and most of autumn), the surface of temperature of TARC is closer to the ideal temperature zone between heating and cooling temperature setpoints (22 °C and 24 °C) than other roof coatings. Therefore, TARC saves more energy than the white roof coating from an all-season, day-and-night perspective. 45

Figure 4.9. Simulated minimum annual space conditioning source energy saving per unit roof area ($SCSES_{min}$) of TARC compared to other existing roof coating materials for different cities representing the 15 climate zones in the U.S. Red and blue circles indicate positive and negative $SCSES_{min}$ values, respectively. The values are scaled to the area of the circles. Representation of the triangle and circle icons is explained in the Method section (subsection 4.6.1). 46

Figure 4.10. Schematic of the adiabatic approximation for surface temperature calculation. For a surface with given solar absorptance (A) and sky-window thermal emissivity (ε_w), this model enables the calculation of the surface temperature T_s in any climate. 47

Figure 4.11. Calculated net radiative cooling power of TARC and a broad-band emitter with a constant emissivity equal to εw of TARC. The results include conditions with various surface temperatures and precipitable water (PW). The atmospheric spectral emissivity for different PW are obtained from [119]. 48

Figure 4.12. Example of surface temperature calculation based on the model for Baltimore, MD. (a) Air temperature from the TMY3 weather files included in the EnergyPlus climate database. (b)-(c) Projected surface temperature and sky-window emissivity of TARC. (d) Calculated energy saving advantage of TARC compared to conventional materials. All savings are normalized to roof area. The indexes in the SCSES map represent: i, white metal plate; ii, aluminum pigments; iii, daytime radiative coolers; iv, silicone; v, acrylic; vi, polyurethane; and vii, asphalt. 50

Figure 5.1. The working principle of STARC as a roof coating, where solar absorptance is temperature-independent but optimized to local climate, and thermal emissivity switches automatically with ambient temperature. 52

Figure 5.2. (a) Structure, composition and mechanism of STARC. (b) A 3D view shows the structure of STARC. (c) Absorptance/emissivity spectra calculated from FTIR spectroscopy result of STARC at low and high temperatures. (d) sky-window emissivity εw calculated from temperature-dependent FTIR measurements. The dashed lines are guides to the eye. 53

Figure 5.3. Absorptance/emissivity spectra calculated from FTIR spectroscopy result of STARC with PE thickness of 12um and 24um, respectively. The two curves in the plot are measured at the same temperature that is randomly selected. The thickness-insensitivity has been checked for multiple different temperatures across the phase transition of $W_xV_{1-x}O_2$..... 54

Figure 5.4. Schematic illustration of the production line for STARC. 55

Figure 5.5. Calculation of space-conditioning source energy consumption of TARC ($SCSES_{TARC}$) in different cities as a function of the TARC solar absorptance (A). The indexes (2A, 3C, etc.) represent the different U.S. climate zones. In each curve, $SCSES_{TARC}$ is vertically offset by its minimum value for better display of the data in the plot. 56

Figure 5.6. (a) Structure of the colored STARC. The chemicals next to the arrows are the pigments used to fabricate the colored STARCs in the corresponding photos on the right-hand side. (b) The spectral absorptance of STARCs in the solar wavelength range, calculated from the integrating sphere (diffuse + specular) measurements. 57

Figure 5.7. The outdoor experiment setup for household thermal regulation demonstration..... 58

Figure 5.8. The 24-hour record of the indoor temperature of model houses with different roof materials (STARC and two reference commercial paints). The left and right panels show magnified plots of temperature at night and noon, respectively. 59

List of Tables

Table 1.1. Emissivity of common materials. 3

Table 2.1. The phase profiles of $W_xV_{1-x}O_2$ layers at node temperatures used in the numerical simulation..... 10

Table 2.2. Composition and thickness profiles of the three graded doped $W_xV_{1-x}O_2$ samples obtained from fitting with numerical simulation. 11

Table 2.3. Comparison of various infrared camouflage systems..... 12

Table 2.4. The composition and thickness profile of each sample shown in Figure 2.7(a), to achieve different T_{IR}. The composition of each layer is represented by different color in the chart. 16

Table 3.1. Material properties used in the simulation..... 30

Table A.1. Calculated $SCSES_{min}$ as the first of merit for TARC in cities across the U.S. Units: MJ/(m^2·y), where m² refers to the roof area. 64

Table A.2. Regressed coefficients $\boldsymbol{\alpha_h}$ and $\boldsymbol{\alpha_c}$ for single-family homes of different vintages in cities across the U.S. Units: MJ/(m^2·y·K), where m² refers to the roof area. 65

Table A.3. Regressed coefficients $\boldsymbol{\alpha_h}$ and $\boldsymbol{\alpha_c}$ for apartment buildings of different vintages in cities across the U.S. Units: MJ/(m^2·y·K), where m² refers to the roof area. 66

Table A.4. Regressed coefficients $\boldsymbol{\beta_h}$ and $\boldsymbol{\beta_c}$ (dimensionless) for single-family homes of different vintages in cities across the U.S..... 67

Table A.5. Regressed coefficients $\boldsymbol{\beta_h}$ and $\boldsymbol{\beta_c}$ (dimensionless) for apartment buildings of different vintages in cities across the U.S..... 68

Acknowledgements

First of all, I would like to give my sincerest gratitude to my advisor, Prof. Junqiao Wu for his admirable guidance and support over my research and life journey in the past five years. He has enlightened me in conceiving the ideas with his solid knowledge and passion. His insightful guidance and continuous support also made me tackle all the challenges in my research. Moreover, I am very grateful to Prof. for offering me the opportunity to serve as a graduate student instructor in his course MSE 111, which is a fruitful teaching experience.

I would like to express my great appreciation to Prof. Jie Yao, Prof. Junqiao Wu, Prof. Van P. Carey for serving on my qualifying exam committee and dissertation committee. I am also grateful to Prof. Costas Grigoropoulos for serving on my qualifying exam committee. Their advice and suggestions haven been beneficial to my research works.

The research works presented in this dissertation would not be possible without the supports from the brilliant colleagues in Wu Group. I am specifically grateful to Dr. Kaichen Dong and Dr. Kechao Tang for working as a productive team and sharing their expertise in the thermal radiation research. I also would like to thank other group members in Wu Group, Dr. Penghong Ci, Dr. Hwan Sung Choe. Dr. Lei Jin, Anthony Salazer, Dr. Danqing Wang, Sorren Warkander, Yuhang Cai, Dr. Yang Gao, Dr. Huili Liu and Dr. Yabin Chen, for their inspiration and help.

I had the pleasure to work with Prof. Jie Yao and his group members, Tiancheng Zhang, Qingjun Wang, Dr. Rui Chen, Dr. Shuai Lou and Dr. Xi wang. I have been immensely benefited from their profound expertise in photonics experiments and simulations. I am also thankful to them for their contribution in the research projects in this dissertation.

I would like to acknowledge the collaboration and help from: Prof. Ali Javey, Prof. Costas Grigoropoulos, Prof. Chris Dames, Dr. Jeff Urban. Dr. Ronnen Levinson, Prof. Xiang Zhang, Prof. David H. Raulet, Dr. Madeleine Gordon, Dr. Hyungjin Kim, Dr. Yoonsoo Rho, Dr. Christopher J. Nicolai, Prof. Chengwei Qiu and Dr. Ying Li from NUS. Prof. Bo Sun from Tsinghua SIGS, Prof. Chang-yu Lin from CYCU.

I also would like to thank to the staffs of the Applied Science & Technology Graduate Group, Material Science Division at Lawrence Berkeley National Laboratory, Marvell Nanolab, and QB3.

Most importantly, I would like to thank my parents and my grandmother. Their unconditional support and encouragement have been crucial to my Ph.D. study and completion of this dissertation.

1. Introduction

1.1. Thermal Radiation: Physics and Applications

1.1.1. Physics of Thermal Radiation

Thermal Radiation is an intrinsic emission of electromagnetic waves from all matter that has a temperature greater than absolute zero. In 1900, Max Planck derived a formula for the hemispherical spectral radiance of a blackbody, which is an idealized object which absorbs and emits radiation with all wavelengths. The spectral radiance B(λ,T) describes the spectral emissive power per unit area, per unit solid angle, per unit frequency for particular radiation frequencies. This is also known as the Planck's Law:

$$B(\lambda, T) = \frac{2hc^2}{\lambda^5} \frac{1}{exp\left(\frac{hc}{\lambda k_B T}\right) - 1} \tag{1-1}$$

Here, c is the speed of light in the medium, λ is the wavelength of the radiation, T is the absolute temperature, h is the Planck constant, and k_B is the Boltzmann constant. Figure 1.1 is a plot of hemispherical spectral emissive power B(λ, T) as a function of wavelength λ at different temperatures.

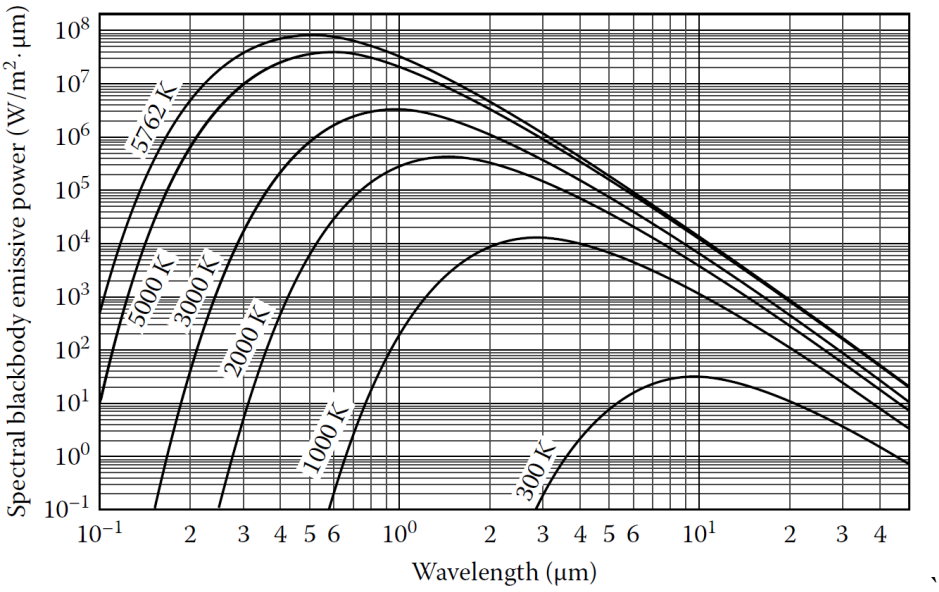


Figure 1.1. Hemispherical spectral emissive power B(λ, T) of a blackbody at different temperatures.

It's clear that the total power of thermal radiation, which is the spectral emissive power integrated over all wavelengths, increases with temperature. Also, the energy emitted at shorter wavelengths increases faster with temperature than the energy emitted at longer wavelengths. Thus, as

temperature increases, the distribution of thermal radiation and maximum spectral emissive power shifts toward smaller wavelengths. The relation between the wavelength with maximum emissive power λ_{max} and temperature is described by Wien's displacement law:

$$\lambda_{max} T = 2897.7721\ \mu m \cdot K \tag{1-2}$$

As an example, the temperature of the photosphere of the sun is approximately 5800K thus the $\lambda_{max,solar}$ is around 500nm, and the solar radiation power mainly lies in the visible and near-infrared (NIR) range.

The expression of the total energy radiated by a blackbody per unit surface area per unit time can also be derived from Planck's law by integrating the spectral thermal emissive power over all wavelengths and directions:

$$j = \int_0^\infty B(\lambda, T) d\lambda \int_0^{2\pi} d\varphi \int_0^{\pi/2} cos\,\theta\, sin\,\theta\, d\theta \tag{1-3}$$

With a substitution of $u = \frac{hc}{\lambda k_B T}$,

$$j = \frac{2\pi h}{c^2}\left(\frac{k_B T}{h}\right)^4 \int_0^\infty \frac{u^3}{e^u - 1} du \tag{1-4}$$

The value of integral on the right is $\pi^4/15$, which gives:

$$j = \sigma T^4, \sigma = \frac{2\pi^5 k_B^4}{15 c^2 h^3} \tag{1-5}$$

where σ is called the Stefan-Boltzmann constant and the relation is known as the Stefan-Boltzmann law. A body that does not absorb all incident radiation emits less energy than a blackbody, and can be characterized by an emissivity ε

$$j = \varepsilon \sigma T^4 \tag{1-6}$$

The emissivity ε ranges from 0 to 1. Table 1.1 shows the emissivity of common materials [1]. In general case, the emissivity depends on the wavelength. Also, according to Kirchhoff's law of thermal radiation, the spectral absorption $\alpha(\lambda, T)$is equal to the emissivity $\varepsilon(\lambda, T)$. The relation between integrated emissivity $\varepsilon_{int}(T)$ and spectral emissivity $\varepsilon(\lambda, T)$ can be expressed as:

$$\varepsilon_{int}(T) = \frac{\int \varepsilon(\lambda,T)\, B(\lambda,T)\, d\lambda}{\int B(\lambda,T)\, d\lambda} \tag{1-7}$$

Note that although $\varepsilon_{int}(T)$ and $\varepsilon(\lambda, T)$ depends on the temperature in the formula, $\varepsilon(\lambda, T)$ is normally insensitive to temperature for common materials. For most application cases, the temperature variation is not large enough to cause a substantial shift of $B(\lambda, T)$, hence the $\varepsilon_{int}(T)$ is also insensitive to temperature. For example, the temperature derivative of emissivity $(d\varepsilon_{int}(T)/dT)$ near room temperature is only $2\times10^{-5}\ ℃^{-1}$ for graphite [2], $-1\times10^{-4}\ ℃^{-1}$ for silicon [3], and $1\times10^{-4}\ ℃^{-1}$for typical metals [4]. However, for phase transition materials, $\varepsilon(\lambda, T)$ is possible to abruptly change across the phase transition. In this case, the $\varepsilon_{int}(T)$ can go through a significant change.

Material	Emissivity ε
Aluminum Sheet	0.09
Brass, Polished	0.03
Nickel, polished	0.07
Glass, smooth	0.92
PVC	0.91
Wood, Pine	0.95
Water	0.95
Concrete, rough	0.94

Table 1.1. Emissivity of common materials.

1.1.2. Applications Related to Thermal Radiation

Thermography is one of the most important applications based on thermal radiation. During the thermography process, a thermal camera receives the thermal radiation emitted from an object and creates an image of it. Since the total power of thermal radiation increase with temperature, thermography can be used to determine the surface temperature of objects. Moreover, thermal radiation is emitted by all objects with a temperature above absolute zero, therefore, thermography can be used to detect the temperature without visible illumination. Thermography has been widely used in many fields such as medical imaging, roof and wall inspections, quality control in electronics, and volcanology.

Another important application related to thermal radiation is thermal insulation. For application cases that involve vacuum or high temperature, thermal radiation is a dominant factor of thermal management. Since most metal materials have a very low emissivity/absorptance [1], the metal sheets can be used to create thermal insulation materials such as heat shield and multi-layer insulation (MLI). When used on spacecraft, the low emissivity material can reduce heat loss through thermal radiation, while protecting the spacecraft from being overheated by the sun. Thermal insulation can also find applications in automotive, aircraft, personal protection, etc.

Sub-ambient passive radiative cooling materials also have become trending for building applications in recent years. The radiative cooling materials feature maximized thermal emissivity and minimized solar absorption to cool the building and save energy from air conditioning. These radiative cooling materials are typically made from porous polymer [5], microparticle-polymer hybrid material [6], wood [7], etc. Experiments shows that these materials can cool the building to several ℃ below the ambient temperature. Therefore, it is expected that the energy consumption in air conditioning can be greatly reduced with these passive radiative cooling materials [8].

However, because of the fast development of material science and fabrication techniques, the latest materials are reaching the physics limit of static emissivity/absorptance ε (0 or 1). Thus, many thermal radiation applications are reaching the performance cap with the static-ε materials. Recently, research efforts on thermal radiation modulation materials have opened unprecedented routes toward thermal applications such as enhancing the sensitivity of thermography [9], thermal

radiation camouflage [10,11], temperature regulation for space objects [12], and temperature-adaptive radiative coating for energy saving in buildings [13,14]. Experiments and calculations have demonstrated that the thermal radiation modulation materials can outperform conventional materials with static- ε in many aspects.

1.2. Physical Properties of the Phase-Transition Material Vanadium Dioxide (VO_2)

VO_2 is a temperature-responsive phase change material that has a metal-insulator transition at 68℃. When the temperature is below the phase transition temperature (T_{MIT} = 68℃), VO_2 has a monoclinic structure and performs like a regular insulator. In contrast, when the temperature is above the T_{MIT}, VO_2 abruptly transfers into a rutile metal phase, Figure 1.2(a) shows the structure VO_2 in both insulating and metallic phases.

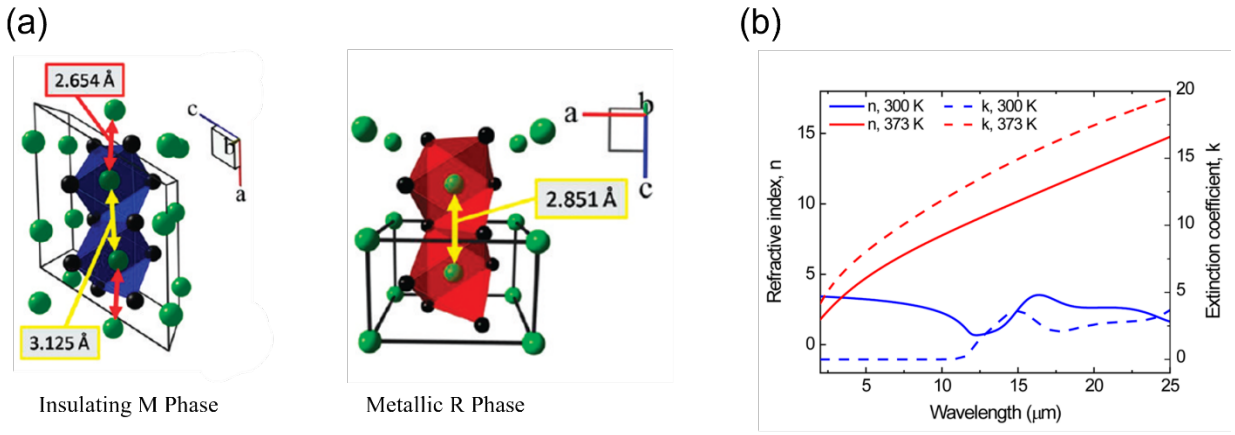


Figure 1.2. (a) Crystal structure of the low-temperature monoclinic insulating phase and high-temperature rutile metallic phase of VO_2 [15]. (b) Refractive index, n and extinction coefficient, k of a 40nm thick VO_2 film as a function of wavelength measured at 300K and 373K [16].

Although the underlying mechanism of the metal-insulator transition of VO_2 remains unknown, the infrared (IR) properties of VO_2 have been extensively studied. When the VO_2 switches from the insulating phase to the metallic phase, it can drastically transfer from transparent insulator to lossy metal in both near infrared and mid infrared range [16]. Due to this strong optical switch property, VO_2 can be utilized for both solar and thermal radiation modulation. Moreover, since the phase transition of VO_2 is driven by temperature change, it is naturally compatible with thermal applications such as temperature regulation, smart building, and thermography.

Another feature of VO_2 is that the phase transition temperature can be tuned for different applications by tungsten (W) doping [17]. The T_{MIT} of tungsten-doped vanadium dioxide ($W_xV_{1-x}O_2$) can be reduced by 25℃ per at% of tungsten. For instance, the $W_xV_{1-x}O_2$ with x=1.5% has a phase transition temperature of 22℃, so it can be used for manufacturing the smart roof for building temperature regulation. The tunable nature of T_{MIT} also grants us the ability to modulate the thermal emissivity of VO_2-based materials across a wide temperature range.

1.3. Outline of the Dissertation

The chapter 2 - 3 are focused on the thermal emissivity modulations in thermography applications.

In chapter 2, we realize a nearly T^{-4} dependence thermal emissivity by modulating the thermal emissivity of a graded W-doped VO_2 ($W_xV_{1-x}O_2$) structure. The T^{-4} dependence strongly deviates from the emissivity properties of conventional materials. An IR camouflage and an IR decoy system are also demonstrated based on the graded $W_xV_{1-x}O_2$ structure.

In chapter 3, we explore the improvement of the noise-equivalent differential temperature (NEDT) of IR cameras. A temperature imaging sensitizer (TIS) is achieved based on the phase transition of $W_xV_{1-x}O_2$ and a photonic resonance cavity structure. Unlike the traditional path of enhancing detection and conversion of infrared radiation power, the TIS increases the temperature-derivative of IR camera readout. Experiments verify that, sensing with TIS results in a reduction in the system's NEDT by 15 times down to ~3 mK.

In chapter 4-5 we investigate the passive radiative cool roof applications.

In chapter 4, we present a mechanically flexible, energy-free, and temperature-adaptive radiative coating (TARC) for intelligent regulation of household temperature. The TARC features a thermally driven metal-insulator transition in cooperation with photonic resonance and demonstrates the self-switching of the system from the radiative cooling mode at high temperatures to the solar-heating or keep-warm mode at low temperatures in an outdoor setting. Simulations indicate the TARC may outperform all conventional roof materials in terms of cutting energy consumption for households in most cities in the U.S.

In chapter 5, we report a scalable temperature adaptive radiative coating (STARC) which can be mass produced with a roll-to-roll system while preserving the same emissivity switching ability as the TARC in chapter 4. The STARC has a novel structure in which $W_xV_{1-x}O_2$ in encapsulated in a polyethylene matrix. The $W_xV_{1-x}O_2$ is protected from water and air as-fabricated so the lifetime as a roof material can be drastically improved. Moreover, the color (and solar absorption) of STARC can be adjusted in a wide range by incorporating IR transparent pigments. Thus, the aesthetic needs and energy saving optimization can be fulfilled. Field tests with a set of mock-up residential houses demonstrated the temperature regulation performance of STARC.

In the last chapter, I summarize my understanding of thermal radiation modulation structures based on vanadium dioxide. Future research directions are suggested for infrared applications and photonic studies.

2. Thermal Radiation Modulation of Graded Tungsten-Doped VO_2 Films

2.1. Introduction

According to the Stefan-Boltzmann law, thermal radiation flux from an object is proportional to the emissivity (ε) and the fourth power of surface absolute temperature (T^4). Most non-metals have a static high emissivity that is almost one, thus the surface temperature can be calculated by the thermal radiation power flux measured by an infrared camera. However, this method can only return a lower temperature readout for metal surfaces due to the lower emissivity.

Since VO_2 has a metal-insulator transition, the emissivity of a smooth VO_2 film can change from high to low as temperature increases across the T_{MIT}. In the temperature window of this phase transition, the decrease of emissivity and the increase of surface temperature of VO_2 film happens simultaneously, thus the thermal radiation flux will deviate from the typical T^4 relation, and the infrared camera will be deceived. However, this novel behavior is only limited within the phase transition range of VO_2, which is typically narrower than 20℃.

To overcome this limitation, we designed and deposited multilayer $W_xV_{1-x}O_2$ films with total thickness less than the infrared skin depth of metallic phase $W_xV_{1-x}O_2$, as schematically shown in the inset of Figure 2.1(b). During the film deposition and post annealing, diffusion of W took place inside the film. As a result, the multilayer structure becomes a graded W-doped VO_2 film, where the x = at% of W continuously varies along the normal direction. The graded doping widens the original temperature window to a broad temperature range, ranging from $T_{MIT}(x_{max})$ to $T_{MIT}(x_{min})$. Figure 2.1(b) shows the ε(λ,T) measured by the Fourier transform infrared (FTIR) spectroscopy.

With proper design of the x and thickness for each layer, it's possible to arbitrarily tune the monotonically decreasing emissivity and corresponding thermal radiation flux within this range. As shown in Figure 2.1(a), the film can be designed to have a greater slope of $\varepsilon_{int}(T)$, but at the cost of a narrower phase transition temperature range. Figure 2.1(c) also shows an example of designing the W-doping profile (dashed line, left-bottom axes) for the desired $\varepsilon_{int}(T)$ (solid curve, right-top axes). Therefore, this multilayer structure serves as a great platform for thermal radiation modulation. To exhibit the capability of this structure, we demonstrated a mechanically flexible and passive IR camouflage as well as a thermal IR decoy, both are immune to drastic temporal temperature fluctuations.

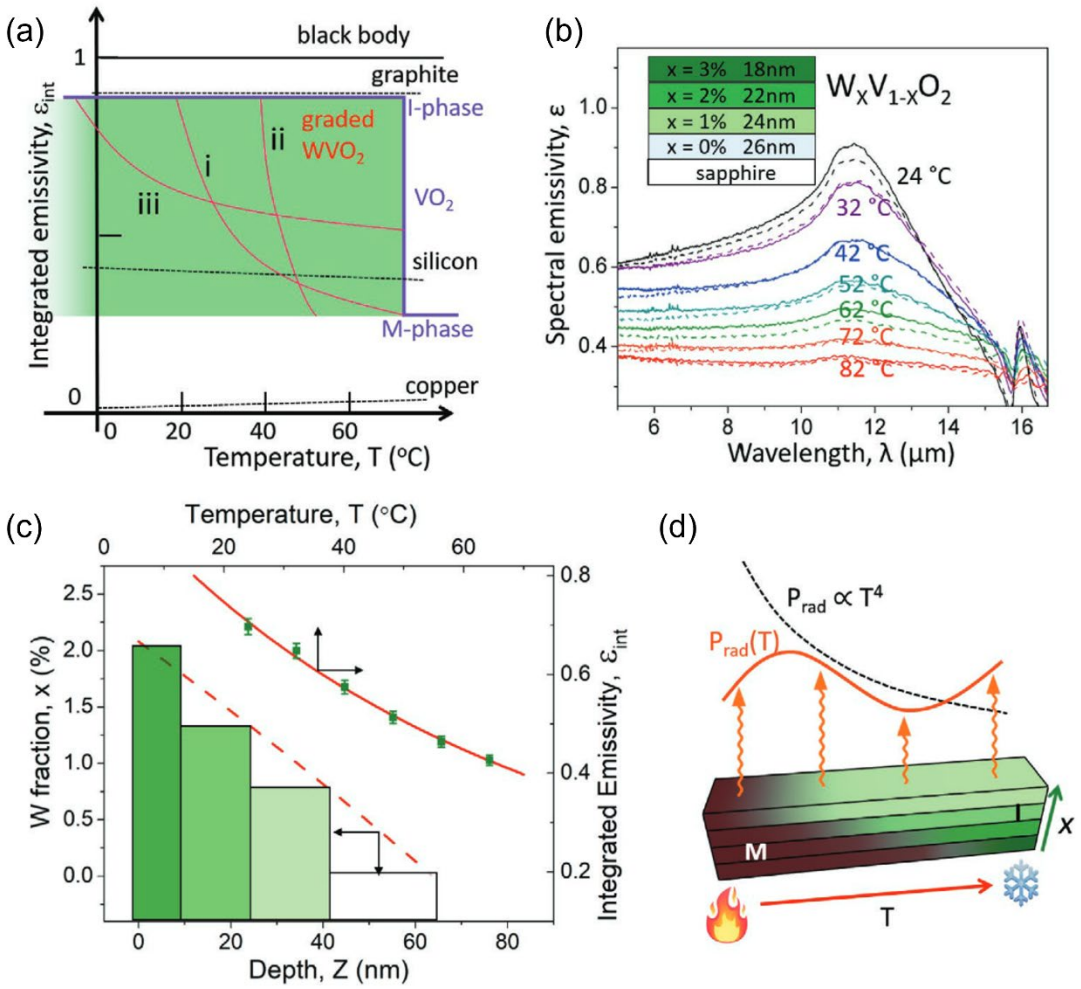


Figure 2.1. Engineering thermal IR emissivity by grading metal (M)–insulator (I) transition. (a) Schematic illustrating the temperature dependence of integrated emissivity (ε_{int}) within the shaded area using graded W-doped VO_2. Three arbitrarily designed emissivity curves are denoted by i, ii, and iii. The behavior of typical materials is also shown for comparison. (b) Spectral emissivity of a graded $W_xV_{1-x}O_2$ structure (schematic in inset) measured over a broad range of temperatures. The solid and dashed curves correspond to data collected during heating and cooling, respectively. (c) Design of W doping profile x(Z) (dashed line, left-bottom axes) to generate the desired $\varepsilon_{int}(T)$ relation (solid line, right-top axes). The boxes represent the actual nominal doping profile used in the $W_xV_{1-x}O_2$ film deposition, and the data points are the experimentally measured $\varepsilon_{int}(T)$ from this film. (d) Schematic showing that by rational design of the W doping profile (x along thickness direction) of $W_xV_{1-x}O_2$, emissivity can be programmed to regulate thermal radiation (P_{rad}) for distinctly different behavior from the T^4 law.

2.2. Design and Preparation of the Multilayer Structure

The multilayer structure consists of a graded $W_xV_{1-x}O_2$ film and an infrared absorptive substrate. When the temperature is between $T_{MIT}(x_{max})$ and $T_{MIT}(x_{min})$, the graded $W_xV_{1-x}O_2$ film is only partially metallic, and the metallic/insulating thickness ratio dynamically changes with temperature. The skin-depth of infrared in M-phase $W_xV_{1-x}O_2$ can be estimated as:

$$\delta = \sqrt{2\rho/\omega\mu_0} \approx 130nm \tag{2-1}$$

Here $\rho = 2 \times 10^{-6}\Omega$m is the resistivity of M-phase $W_xV_{1-x}O_2$, $\omega = 2\pi \cdot 30$THz is the angular frequency at IR wavelength ~ 10 μm, and μ_0 is the vacuum permeability. Since the total thickness is 100nm and smaller than the skin-depth, the absorption of the infrared radiation can be tuned by the temperature-induced thickness change of M-phase $W_xV_{1-x}O_2$. For example, we can adjust the thickness and x value of each layer to get a $\varepsilon_{int}(T)$ that follows $1/T^4$ and negate the increase of thermal radiation power that is caused by the temperature change (Figure 2.1(c)).

$W_xV_{1-x}O_2$ thin films were grown on c-cut sapphire and borosilicate glass substrates using pulsed laser deposition (PLD). The graded W doping was achieved by sequentially focusing the pulsed laser on a series of $W_xV_{1-x}O_2$ targets with different W doping ratios. The targets were prepared by mixing WO_3 and V_2O_5 powders with W/V the atomic ratio ranging from 0% to 3.0%, then made into 1 inch diameter round discs with a hydraulic press. All thin films were deposited in 5 mTorr O_2 environment at 475 °C substrate temperature. The PLD laser energy was set at 321 mJ with 5 Hz pulse frequency. A post-deposition annealing at 475 °C for 30 min in the same 5 mTorr O_2 environment was performed for all graded doped $W_xV_{1-x}O_2$ film. The thickness and deposition rate of the thin films were measured by atomic force microscopy (AFM) and scanning electron microscopy (SEM), and the W faction as well as depth profile was characterized by X-ray photoelectron spectroscopy (Figure 2.2).

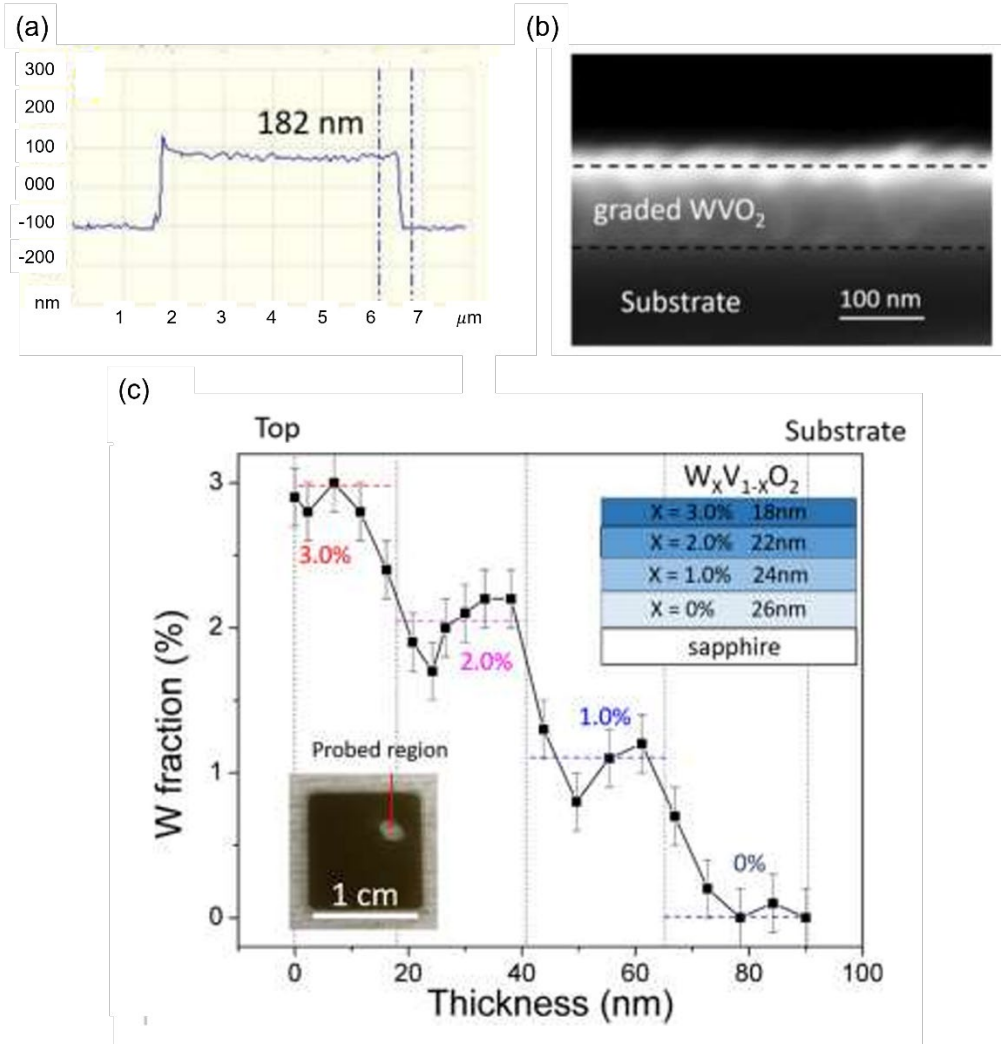


Figure 2.2. Thickness measurements and doping profile characterization of VO_2 films. The VO_2 film was deposited on a sapphire substrate by PLD, and then patterned by photolithography and selective dry etching. (a) The thickness of VO_2 extracted from the step heights in the surface line profiles of AFM. Given the deposition time of 90 mins, the result indicates a growth rate of ~ 2.0 nm/min. Similar deposition rate was obtained for $W_xV_{1-x}O_2$ films, with x ranging from 0 to 3.0%. (b) A cross section view of a graded $W_xV_{1-x}O_2$ film by SEM. (c) Depth profile of W fraction (x) across the thickness of a multilayer, obtained by XPS with controlled sputtering. The gradual change of W fraction across different layers supports the smoothly graded W-doped structure of $W_xV_{1-x}O_2$.

$W_xV_{1-x}O_2$ thin films grown on borosilicate glass substrates were transferred onto PE tapes by sticking the $W_xV_{1-x}O_2$ side to the adhesive side of the tape, and then etching off the 170 μm thick substrate by dipping into 49% hydrofluoric acid for 5 min. The samples with transferred $W_xV_{1-x}O_2$ were then rinsed in deionized water for 3 min and gently blown dry with a N_2 gun. The interfacial adhesion was strong and no delamination of $W_xV_{1-x}O_2$ was observed during the wet transfer process, in further contact with water, or with mechanical bending and twisting of the tape. The thickness of the PE tape (default) and the scotch tape was ≈0.20 and 0.08 mm, respectively. The visible color mainly depends on the thickness of the graded $W_xV_{1-x}O_2$ coating layer. Thicker film

will appear blue/purple, while thinner film tends to have brown/yellow color. When taking a photo, the lighting and the reflection will affect the visible appearance of the sample surface as well.

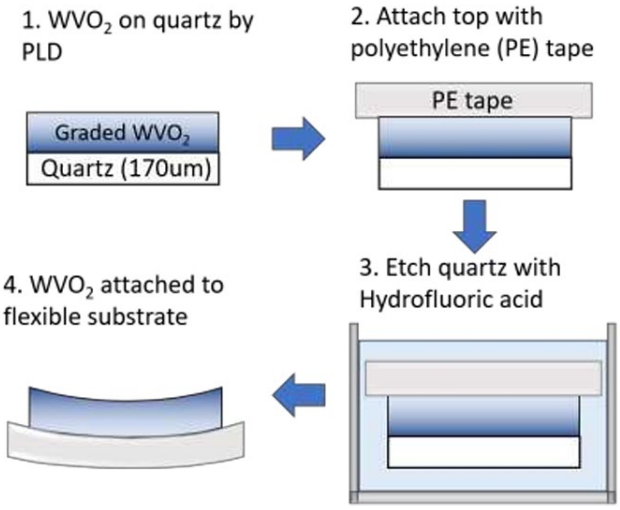


Figure 2.3. Schematics of the process to transfer $W_xV_{1-x}O_2$ onto a flexible PE tape. $W_xV_{1-x}O_2$ thin films grown on quartz substrates were transferred to PE tapes by sticking the $W_xV_{1-x}O_2$ side to the adhesive tape, and then etching off the 170 μm thick quartz substrate by dipping in 49% Hydrofluoric (HF) acid for 5 mins. The samples with transferred $W_xV_{1-x}O_2$ were then rinsed in deionized water for 3 mins and gently blown dry with a N2 gun.

2.3. Numerical Simulation of the Emissivity

Numerical simulation of the emissivity/absorptance was conducted using CST Microwave Studio where the perfect electrical conductor (PEC) and the perfect magnetic conductor (PMC) were used for the boundary condition in the in-plane directions. Based on the phase transition plots in Figure 2.4(a), the model employs a set of static node temperatures where all $W_xV_{1-x}O_2$ layers are in either purely insulating (I) phase or purely metallic (M) phase. The simulated curves were generated by connecting the calculated emissivity at each node temperature points. The node temperatures and the phase profile schematic are shown in Table 2.1.

Node temperature	x=3.0%	x=2.0%	x=1.3%	x=0.75%	x=0%
30°C	M	M	I	I	I
45°C	M	M	M	I	I
60°C	M	M	M	M	I
75°C	M	M	M	M	M

Table 2.1. The phase profiles of $W_xV_{1-x}O_2$ layers at node temperatures used in the numerical simulation

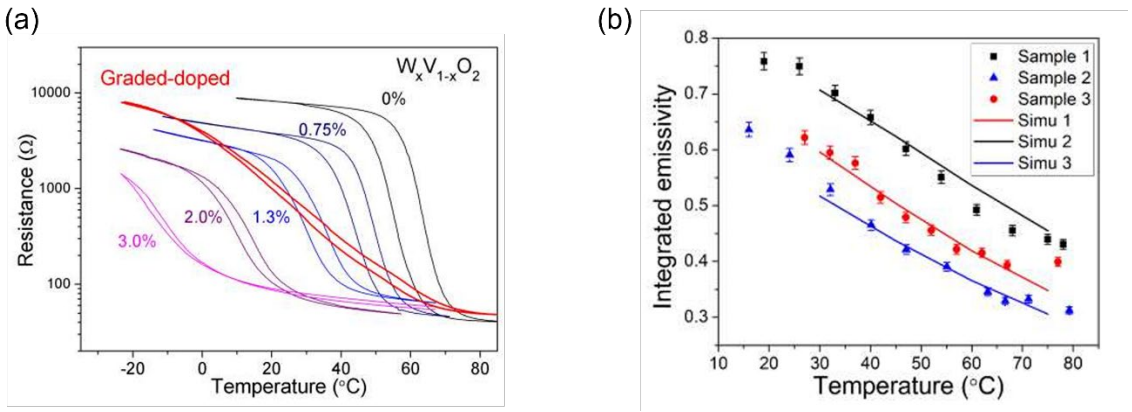


Figure 2.4. (a) Resistance-temperature data of uniformly doped $W_xV_{1-x}O_2$ thin films with different W fractions, measured by standard four-probe method. The abrupt drop in resistivity occurs at the T_{MIT} of each film. The resistance of a graded doped $W_xV_{1-x}O_2$ film (red curve) is also plotted for comparison, showing that its MIT is spread over a wide temperature range. The lack of kinks and abrupt changes in the electrical sheet resistance of the multilayer indicates that it becomes a smoothly graded W-doped structure. (b) Numerical simulation of three graded $W_xV_{1-x}O_2$ samples on PE tape. The symbols are experimental data, and the lines correspond to best-fit results.

The I phase of $W_xV_{1-x}O_2$ is taken as a lossless dielectric with real part of dielectric constant $\varepsilon_1 = 4.9$, and the M phase of $W_xV_{1-x}O_2$ follows the Drude model established in previous reports [72]. The substrate (high-emissivity PE tape) is approximated as a black body. For optimal fitting, we introduced a 1 nm-thick, high-loss layer at the top of all samples. This thin high-loss layer could be caused by damage from the 49% HF etching during the wet-transfer process. The experimental integrated emissivity of three samples as a function of temperature were fitted with the numerical simulation, and a good agreement was achieved as shown in Figure 2.4(b). The W doping profiles obtained from the best fits are shown in Table 2.2, and are compared to the intended profiles from the film deposition.

Sample index		Layer thickness (nm)				
		x=3.0%	x=2.0%	x=1.3%	x=0.75%	x=0%
1	Best fit	-	7	11	14	18
	Intended	-	6	9	12	15
2	Best fit	-	12	17	21	26
	Intended	-	10	14	18	22
3	Best fit	12	14	19	24	29
	Intended	8	12	16	20	24

Table 2.2. Composition and thickness profiles of the three graded doped $W_xV_{1-x}O_2$ samples obtained from fitting with numerical simulation.

2.4. Modulation of Thermal Radiation Power: Two Unique Functions

2.4.1. IR camouflage

As the first example, we demonstrate a thermal IR camouflage using the graded $W_xV_{1-x}O_2$ platform, of which the working principle is shown in Figure 2.5(a). When x and thickness of each layer were judiciously selected (Figure 2.5(c)), the graded doped $W_xV_{1-x}O_2$ exhibits an ε_{int} that depends on temperature approximately following $1/T^4$. The FTIR-measured $\varepsilon_{int}(T)$ of a sample prepared following this design method is shown in Figure 2.5(b). The $1/T^4$ dependence of $\varepsilon_{int}(T)$ is multiplied with the Stefan–Boltzmann T^4 relation of a black body, to give the T-independent thermal radiance P_{rad}, as shown in Figure 2.5(b). The constant P_{rad} over a temperature range over 50 °C near room temperature invalidates the assumption of T-dependent P_{rad}, the principle behind IR imaging [19,20]. As such, the structure would appear to have a constant IR temperature (T_{IR}) when imaged by an IR camera, despite the reality that its actual temperature may vary widely. Unlike low-emissivity camouflage coatings that rely on reflection signals from a confinement and thus limited to indoor scenarios, the IR camouflage based on graded $W_xV_{1-x}O_2$ fools the camera by manipulating thermal radiation from the target itself, making it ideal for outdoor applications.

Existing IR camouflage techniques use a coating whose emissivity can be modulated by effects of thermochromism [21-23], electrochromism [24-27], photo carrier doping [28], or mechanical actuation[29]. These active camouflage techniques generally require energy input to operate and are based on rigid and complicated heterostructures. They are also typically limited to only camouflage objects with uniform and slow-varying temperature profiles. In contrast, our graded $W_xV_{1-x}O_2$ film offers an IR camouflage that is power-free, monolithic, and mechanically flexible (Table 2.3). As the total thickness of the $W_xV_{1-x}O_2$ film is less than 100 nm, the $W_xV_{1-x}O_2$/tape structure can be bent to curvatures exceeding 10 cm^{-1} (Figure 2.5(c)) without degrading its camouflage performance. The mechanical flexibility allows the camouflage to be easily applied as a tape onto non-flat surfaces, with minimal or no impact to the performance. No noticeable degradation in camouflage property or change in surface morphology was detected after up to 100 heating/cooling cycles through the working temperature range (15–65 °C), demonstrating good reliability of the film. In Figure 2.6, a T_{IR} difference of ≈3 °C is observed between the heating and cooling branches, caused by the hysteresis effect of the $W_xV_{1-x}O_2$ phase transition. This degree of impact should not affect the general applicability of the technique, and could be reduced by future work to optimize the hysteresis, including process by crystal dehydration [30] or Ti doping method.[31]

Material	Working mechanism	Working temperature	Power consumption	Mechanical property	Adaptability to non-uniform temperature	Resoponse time
VO_2/Graphene/CNT	Thermochromism	>54°C	4200 W/m^2	Flexible	Not reported	40ms
VO_2 nanopowder	Thermochromism	>75°C	Not reported	Rigid	Not reported	Not reported
Graphese/PE/Ionic liquid	Electrochromism	Room temperature	Not reported	Flexible	Yes/ multiplexing	330ms
N-doped ZnO with Au resonators	Photo carrier doping	80°C	Not reported	Rigid	Yes/ multiplexing	100s
Cephalopods inspiration	Mechanical actuation	4-30°C	>8J/ m^2 per cycle	Flexible	Yes/ multiplexing	720ms
Graded $W_xV_{1-x}O_2$	Self-adaptive thermochromism	20-70°C	0	Flexible	Yes/ monolithic	<50ms

Table 2.3. Comparison of various infrared camouflage systems

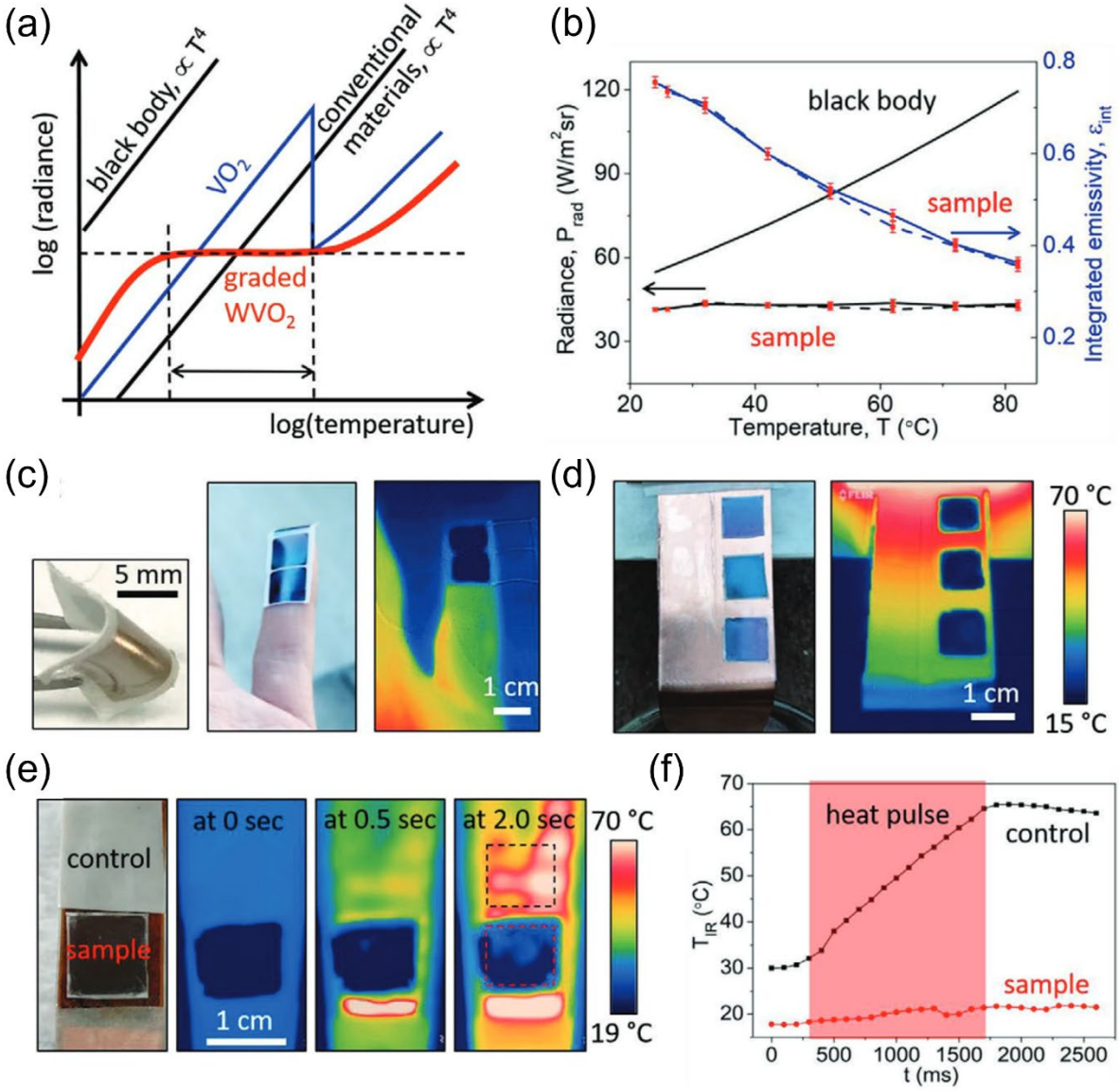


Figure 2.5. Mechanically flexible, power-free, and ∇T- and dT/dt-immune camouflage based on the graded $W_xV_{1-x}O_2$. (a) Schematic illustrating constant thermal radiance over a wide range of temperature from the camouflage, in stark contrast to the Stefan–Boltzmann T^4 law from conventional materials. (b) Thermal radiance and integrated emissivity of the film as a function of temperature, showing that the negative temperature coefficient of emissivity counteracts the T^4 law to yield a temperature-independent thermal radiation power. The solid and dashed curves are for measurements during heating and cooling, respectively. (c) Optical image of a graded $W_xV_{1-x}O_2$ film transferred onto a PE tape showing high mechanical flexibility. The visible color of the sample is related to the $W_xV_{1-x}O_2$ thickness and lighting on surface. The fingertip is hidden from the IR camera when covered with the camouflage. (d) Camouflaging an object with large spatial temperature variation from ≈25 to 65 °C, showing immunity to ∇T. (e) Camouflaging an object with drastic temperature surge, showing immunity to dT/dt. As shown in (f), the actual temperature of the camouflage (represented by the IR temperature of the control that is a high-emissivity tape placed near the sample) rises rapidly by the heating pulse, while the IR temperature of the camouflage stays nearly flat. The IR temperature was measured by averaging the camera reading in the center 1 × 1 cm^2 region of each film (dashed boxes), and the error bars are comparable to the symbols in size.

During the experiments, the IR images and videos were captured by a FLIR ONE infrared camera. To avoid reflection signals from the camera and the surrounding, the default viewing angle was set as 15° instead of normal incident direction, and the experiments were performed in an open-area outdoor environment under clear sky (little cloud). The temperature was controlled by the same thermal stage used in the FTIR measurements. When taking an IR image, the camera measures the incident thermal radiation P_{rad}, and gives the temperature reading (T_{IR}) assuming a constant emissivity for the target (ε_0= 0.90). The relationship can be described by the equation: $\varepsilon_0\sigma T_{IR}^4=P_{rad}$. The T_{IR} was then plotted as a function of actual temperature to demonstrate the camouflage performance. Figure 2.5(c) shows optical image and IR snapshot of a finger where the tip is covered by the camouflage. Distinct from the exposed skin, the part covered by the camouflage displays a T_{IR} similar to the environment, concealing the fingertip from IR detection. Apart from such conventional application as a living body camouflage, our structure has the inherent, unique advantage to cover up objects with large spatial variation (∇T) or abrupt temporal fluctuation (dT/dt) of temperature. In Figure 2.5(d), a copper plate coated with high-emissivity tape is thermally biased with T varying from 25 to 65 °C. Three identical $W_xV_{1-x}O_2$ camouflages were placed at different positions of the plate that have distinct local temperatures. The regions underneath the camouflages are simultaneously masked from IR detection regardless of the different local temperatures and high thermal gradient. Compared to using multiplexing to address the spatial temperature variation in conventional camouflages [25,28], the graded $W_xV_{1-x}O_2$ design offers a much simpler, monolithic, power-free, and titheless approach.

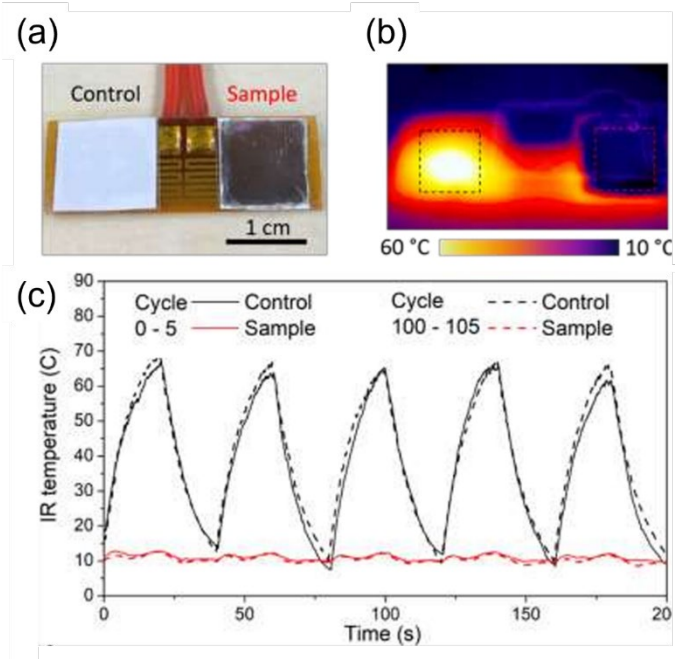


Figure 2.6. Reliability test for graded $W_xV_{1-x}O_2$ camouflage. (a). A high emissivity coating (control) and our graded $W_xV_{1-x}O_2$ camouflage attached to each side of a wing-shape heater, which ramps the temperature between ~15 °C and ~65°C with cycles of 40s. (b). An IR image during the temperature ramping. The black box and red box denote the region where IR temperature measurements are averaged for the control and sample, respectively. c. Measured IR temperature for control and sample over cycles 0-5 compared to cycles 100-105. The IR camouflage performance shows no degradation after over 100 heating/cooling cycles through the working temperature range.

The camouflage is also inherently immune against abrupt temperature fluctuation. In Figure 2.5(e), a heater membrane is partly covered by our graded $W_xV_{1-x}O_2$ film transferred onto a high-emissivity PE tape (sample), and the rest is covered by the high-emissivity PE tape alone (control). The temperature of the plate shoots up rapidly when a current pulse passes through the heater. The IR camera catches clearly a temperature spiking up to 65 °C within less than 2 s from the control surface, while the camouflaged surface stays at nearly constant T_{IR} of 20 °C irrespective of the heat pulse. The detected T_{IR} is plotted as a function of time in Figure 2.5(f), which shows a nearly total immunity to the temperature surge. This immunity is a substantial advantage over the strategy of adjusting the emissivity using a feedback loop in conventional camouflages, as the latter typically has a response time over seconds [25,26,29] and would have the object exposed to detection during the response lagging time.

2.4.2. IR decoy

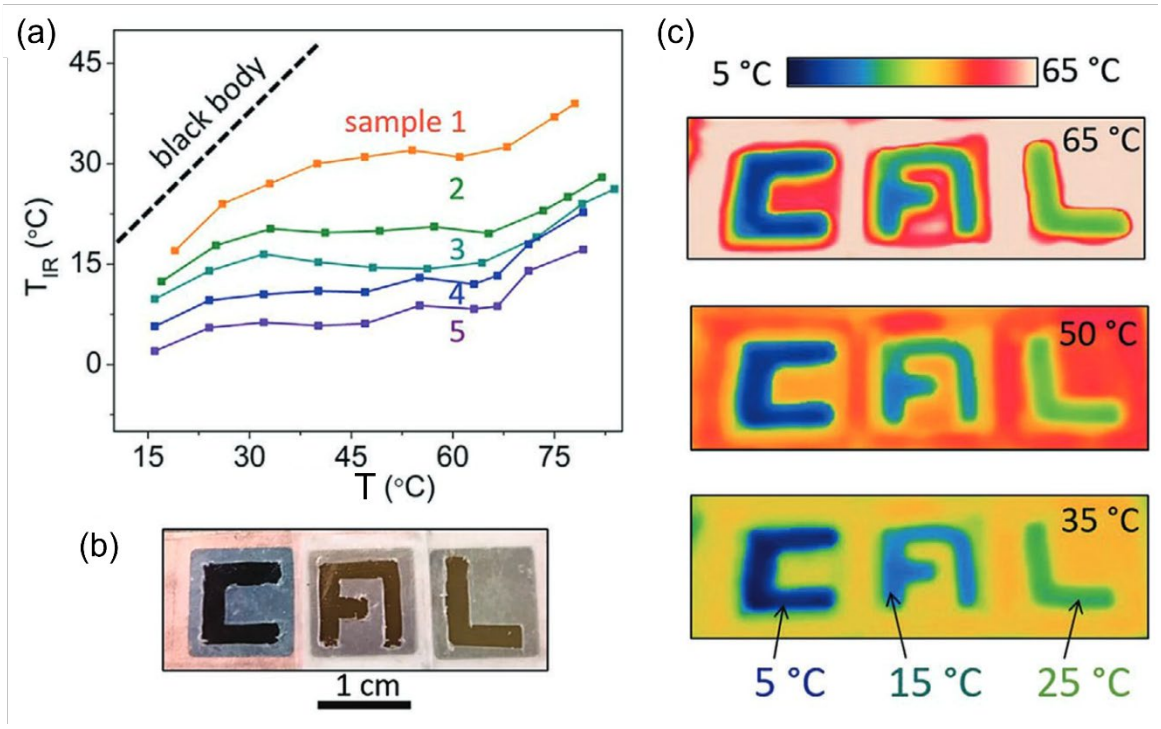


Figure 2.7. Demonstration of temperature-independent thermal IR decoy. (a) IR temperature (T_{IR}) versus actual temperature (T) of five flexible structures, where the graded $W_xV_{1-x}O_2$ configuration is designed to yield T-independent, but different values of desired T_{IR} within the working range of T. Details of these samples are shown in Table 2.4.The error bars are comparable to the symbols in size. (b) Optical and (c) IR images, using the samples 1, 3, and 5, respectively. A pattern of "CAL" is made to show "C" at constant $T_{IR}\approx$ 5 °C, "A" at $T_{IR}\approx$ 15 °C, and "L" at $T_{IR}\approx$ 25 °C, regardless of T varying to 65, 50, or 35 °C. The three samples are all 1 × 1 cm^2 in size.

We also demonstrated another unique function, a thermal IR "decoy," using the structure. A decoy is different from the camouflage in the way that the decoy would not only passively conceal the real thermal activity of the object from an IR camera, but also intentionally fool the camera with a counterfeited T_{IR} that is independent of T distribution and fluctuation. That is, to create a robust thermal radiative pattern $T_{IR}(X,Y,Z)$ on a surface that has arbitrary actual temperature distribution

T (X,Y,Z,t), where X, Y, and Z are the coordinates of the surface and t is time. Because the overall emissivity of the graded $W_xV_{1-x}O_2$/tape system is the combined effect of both the $W_xV_{1-x}O_2$ film and the tape, by using different doping profiles for the graded $W_xV_{1-x}O_2$ film and transferring onto different tapes, T_{IR} of the camouflage can be designed to take distinct values to meet different requirements. A series of flexible $W_xV_{1-x}O_2$/tape samples were prepared (details in Table 2.4). As shown in Figure 2.7(a), despite T varying widely from room temperature to ≈70 °C, these samples all exhibit a nearly constant T_{IR} within the T range, whereas T_{IR} is designed to be equal to any desired value in the range of 5–30 °C. As a proof of concept, Figure 2.7(b)-(c) demonstrates a working decoy where the image of "CAL" shows a stable IR temperature reading, regardless of the change in T. Such decoying information can be also encoded during the film deposition by laterally patterning the composition and thickness of the graded $W_xV_{1-x}O_2$ film, allowing fabrication of a monolithic and lithographically manufacturable decoy (Figure 2.8).

	Sample 1	Sample 2	Sample 3	Sample 4	Sample 5
Substrate	PE tape	PE tape	PE tape	PE tape	Scotch tape
x=3.0%	15 nm	20 nm	22 nm	22 nm	22 nm
x=2.0%	12 nm	16 nm	18 nm	18 nm	18 nm
x=1.3%	9 nm	12 nm	14 nm	14 nm	14 nm
x=0.75%	6 nm	8 nm	10 nm	10 nm	10 nm
x=0%				6 nm	6 nm

Table 2.4. The composition and thickness profile of each sample shown in Figure 2.7(a), to achieve different T_{IR}. The composition of each layer is represented by different color in the chart.

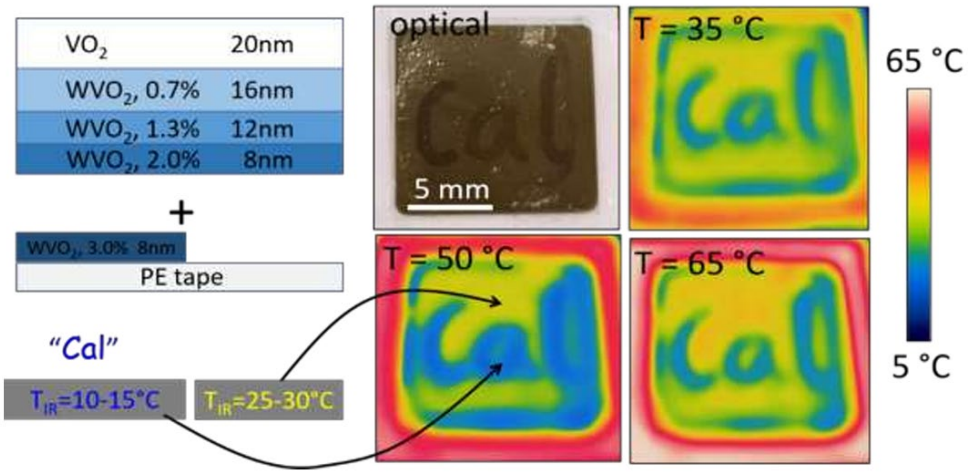


Figure 2.8. A monolithic decoy prepared by encoding the decoy pattern during the film deposition, by adding an extra layer of $W_{0.03}V_{0.97}O_2$ in areas that need colder IR temperature (T_{IR} = 10 - 15°C), while the rest is designed to be at higher T_{IR} = 25 - 30°C. The performance shows the T-independent T_{IR} images consistent with the design.

While these features greatly expand the application of radiative camouflage to inhomogeneous and dynamic environments as well as IR decoying, they also inspire novel device concepts based on reflection or transmission of IR signals. As expected, over the broad spectral range from near-IR (down to the plasma wavelength ≈1.2 μm) to the far-IR, the reflectivity of the graded $W_xV_{1-x}O_2$

would exhibit a temperature dependence that is much stronger than that of conventional materials (Figure 2.9, shows part of the spectrum). This feature enables potential ways for high-sensitivity remote temperature sensing using thermo-reflectance imaging, or active reflectance modulation of IR signals. Therefore, the graded $W_xV_{1-x}O_2$ structure offers a general platform for unprecedented manipulation and processing of IR signals for novel radiative and reflective systems.

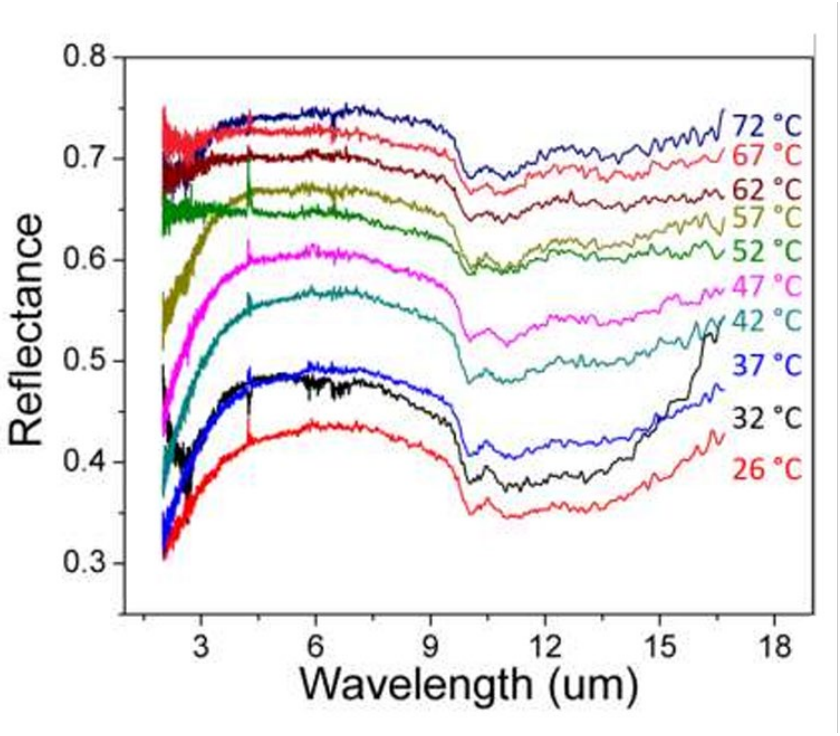


Figure 2.9. Normal-incidence spectral reflectance from 2 μm to 16 μm measured by FTIR of a graded doped $W_xV_{1-x}O_2$ film transferred onto the PE tape. The sample is the sample 3 in Table 2.4.

2.5. Summary

We achieved a power-free, monolithic, and mechanically flexible IR camouflage based on the graded W-doped VO_2 structure. This IR camouflage is not limited to indoor scenarios since it directly modulates the thermal radiation from the target. With pre-designed W-doping profile, different T_{IR} in the working temperature range can be achieved. Thus, it's possible to build an IR decoy system with the graded W-doped VO_2 structures. Moreover, this material provides a platform where emissivity can be engineered to exhibit nearly arbitrary, strong temperature dependence (decreasing with temperature) beyond that of conventional materials.

3. Thermal Imaging Sensitizer (TIS) Driven by the Metal-Insulator Transition of VO_2

3.1. Introduction

In chapter 2, we demonstrated a graded W-doped VO_2 film that can deceive the IR camera by modulating an emissivity that decreases with temperature. With proper design, it can achieve an almost invariant thermal radiation power in the working temperature range. In this chapter, we would like to present our research effort along an opposite direction, which is enhancing the temperature sensitivity of IR camera.

The IR thermography at ambient finds diverse applications in fields ranging from night vision [32], security surveillance [33], and electronics inspection [34] to medical diagnostics [35], structural defect screening [36], and academic research [37]. The noise-equivalent differential temperature (NEDT) is one key figure of merit for these cameras. It is a signal-to-noise figure which represents the temperature difference which would produce a signal equal to the camera's temporal noise.

$$NEDT = V_{noise} \cdot \frac{dT_{iR}}{dV} \cdot \frac{dT}{dT_{IR}} \tag{3-1}$$

The NEDT of IR camera has been improved via better designs to enhance detection and conversion of P_{rad} [38-40] (i.e. enhancing $\frac{dT_{iR}}{dV}$ in Equation (3-1)) while assuming the T dependence of P_{rad} to be strictly bounded by the T^4 law. Consequently, the roadmap of NEDT currently saturates at 20 to 40 mK for uncooled bolometers, with little advance in the past decades (Figure 3.1).

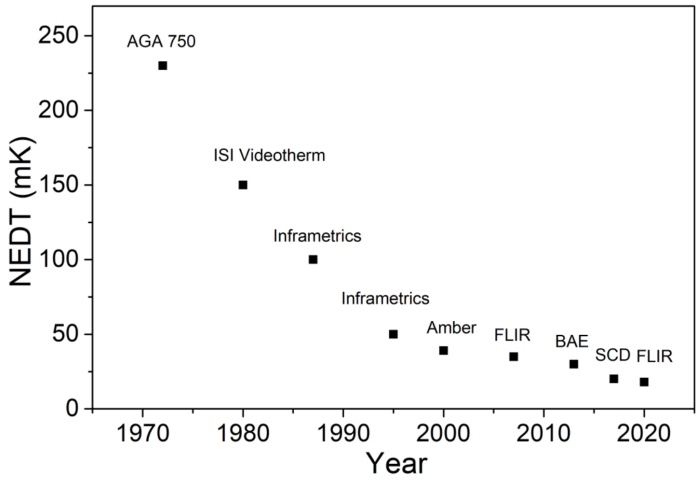


Figure 3.1. Roadmap of NEDT for state-of-the-art commercial uncooled bolometers [41-44]. Little advance was made in the past two decades, with the value currently saturated at 20 -40 mK. The working bandwidth is 20 –60 Hz.

The IR camera generates the temperature reading (T_{IR}) by assuming a constant wavelength-integrated emissivity (ε_0) for the object. In the case when the actual emissivity (ε) is different from

ε_0, T_{IR} deviates from the actual temperature T via $P_{rad} = \varepsilon_0\sigma T_{IR}^4 = \varepsilon\sigma T^4$, where σ is the Stefan-Boltzmann constant. The differentiation of T_{IR} over T is

$$\frac{dT_{IR}}{dT} = \left(\frac{\varepsilon}{\varepsilon_0}\right)^{\frac{1}{4}}\left(1 + \frac{1}{4}\frac{d\ ln\ \varepsilon}{d\ ln\ T}\right) \tag{3-2}$$

and is assumed to be equal to $(\varepsilon/\varepsilon 0)^{1/4}$ as ε of conventional materials is nearly T-independent. However, dT_{IR}/dT would be much higher if ε becomes strongly dependent on T, drastically amplifying small variations in T.

In this work, the strong, positive T dependence of ε is realized by integrating the metal-insulator transition (MIT) of tungsten-doped vanadium dioxide ($W_xV_{1-x}O_2$) with a photonic cavity structure (Figure 3.2(a)). ε switches to a much higher value when T rises above the transition temperature, boosting dT_{IR}/dT and refining NEDT by a factor over 15 (Figure 3.2(b)). The device, coined as a thermal imaging sensitizer (TIS), is fabricated on a thin flexible substrate, and can be conveniently and repeatedly applied to and peeled off from the object surface, as shown in Figure 3.2(a).

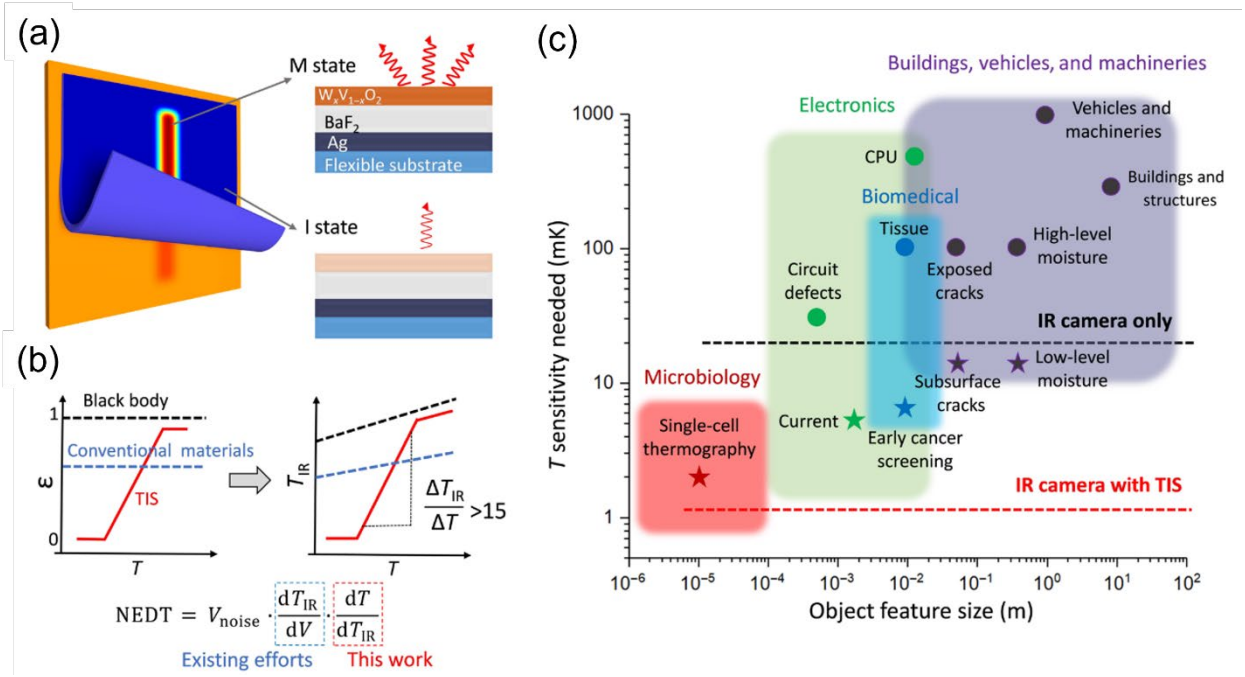


Figure 3.2. Thermal imaging sensitized by MIT. (a) Schematic illustration of boosted temperature resolution of thermography by the thermal imaging sensitizer (TIS) and its working mechanism. As the object (covered with TIS) is heated up across the MIT, the TIS switches from a reflector (hence, low absorbance and low emissivity) in the insulating (I) phase to a resonator (hence, high absorbance and high emissivity) in the metallic (M) phase for mid-IR waves. (b) In contrast to conventional materials or black body, the sharp increase in thermal emissivity (ε) at the MIT of $W_xV_{1-x}O_2$ introduces a high amplification (>15) of ΔT to ΔT_{IR} and thus reduction in NEDT. (c) Representative temperature resolution required for ambient thermography in various applications with paradigmatic feature sizes. TIS pushes boundaries of these applications and generates new markets.

3.2. Structural Design and Characterization of TIS

3.2.1. Working Principle of the ε Switching

The function of TIS builds on the metal-insulator transition of the strongly correlated electron material $W_xV_{1-x}O_2$ at the temperature $T_{MIT} \approx 67°C - 25°C \cdot x \cdot 100$, which can be conveniently tuned from 67° to −100°C by varying the composition x [17]. In the insulating (I) state, the material is basically transparent to IR in the 8 to 14 μm wavelength range, and incoming IR radiation will penetrate through the top two layers with negligible absorption and reflected by the Ag mirror, as shown in Figure 3.2(a). In contrast, when the $W_xV_{1-x}O_2$ switches to the metallic (M) state, it becomes highly absorptive to IR radiation, and the absorption is further enhanced by the photonic resonance around wavelength of 9.8 μm in the designed 1/4-wavelength cavity. Consequently, the system will go through an abrupt increase in absorbance and hence emissivity, according to the Kirchhoff's law of radiation.

3.2.2. Fabrication

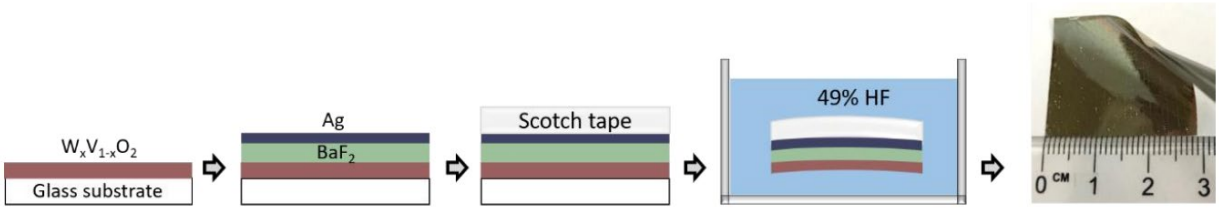


Figure 3.3. Schematics and picture for the fabrication of the TIS.

$W_xV_{1-x}O_2$ thin films were grown on 170-μm-thick borosilicate glass substrates using pulse laser deposition (PLD). The PLD targets were prepared by mixing WO_3 and V_2O_5 powders with W:V atomic ratio ranging from 1.1 to 1.5%, and then made into 1-inch-diameter round discs with a hydraulic press. All thin films were deposited in 5 mtorr O_2 environment at 570°C substrate temperature, and the PLD laser energy was set at 321 mJ with 5-Hz pulse frequency. 30nm of $W_xV_{1-x}O_2$ was grown at a rate of 3 nm/min, followed by a postdeposition anneal at 570°C for 30 min in the same 5 mtorr O_2 environment. On top of the $W_xV_{1-x}O_2$ films, 1.5-μm-thick BaF_2 and 100-nm-thick Ag layers were grown sequentially via thermal evaporation. The growth rates of BaF_2 and Ag were controlled at 20 and 2 Å/s, respectively. The thicknesses of the $W_xV_{1-x}O_2$, BaF_2, and Ag layers were optimized for best optical performance with finite-element method simulation using COMSOL Multiphysics and characterized by cross-sectional scanning electron microscopy (SEM) imaging (Figure 3.5(b)). In the transfer process, a piece of 0.06-mm-thick single-sided sticky scotch packaging tape was first carefully applied to fully cover the $W_xV_{1-x}O_2/BaF_2/Ag$ structure, where the Ag layer was stuck to the adhesive side without any residual air bubbles. The initial borosilicate glass substrate for thin-film growth was then etched off by 49% hydrofluoric acid in 5 min. After the release process, the scotch tape with transferred $W_xV_{1-x}O_2/BaF_2/Ag$

structure was rinsed in deionized water and dried with a N_2 gun. Detailed schematics and pictures of the process can be found in the Figure 3.3.

3.2.3. Setup of IR Camera Measurements

The sensitizing function of TIS is first characterized by imaging from an IR camera. The IR images were captured by a FLIR ONE IR camera working at a wavelength range of 8 to 14 μm, with a frame rate of 8.7 Hz. When taking IR images, the camera measures the incident thermal radiation P_{rad}, and then gives the temperature reading (T_{IR}) assuming a constant emissivity for the target (ε_0 = 0.90, default setting of the camera, which applies to all images in this work). Equations in Figure 3.4 demonstrate that the environmental radiation, which is denoted as S_{env}, has a negative effect on enhancing the dT_{IR}/dT. The differentiation of radiation power (P_{rad}) with T has an additional negative term contributed by S_{env}, suggesting that S_{env} needs to be reduced to optimize the sensitizing effect. To minimize the reflection signals from the camera and the surroundings, the default viewing angle was set as 15° instead of normal incident direction, and the experiments were performed either in an open-area, outdoor environment under clear sky (cloud free), or using a cold-plate setup. When doing experiments in outdoor environment, we avoid exposing the TIS and target surfaces to direct solar radiation, by setting up the system in the shadow of a building or blocking the sunlight with a solar shield. Moreover, the cold-plate setup shows a similar effect comparable to experimenting in the outdoor environment.

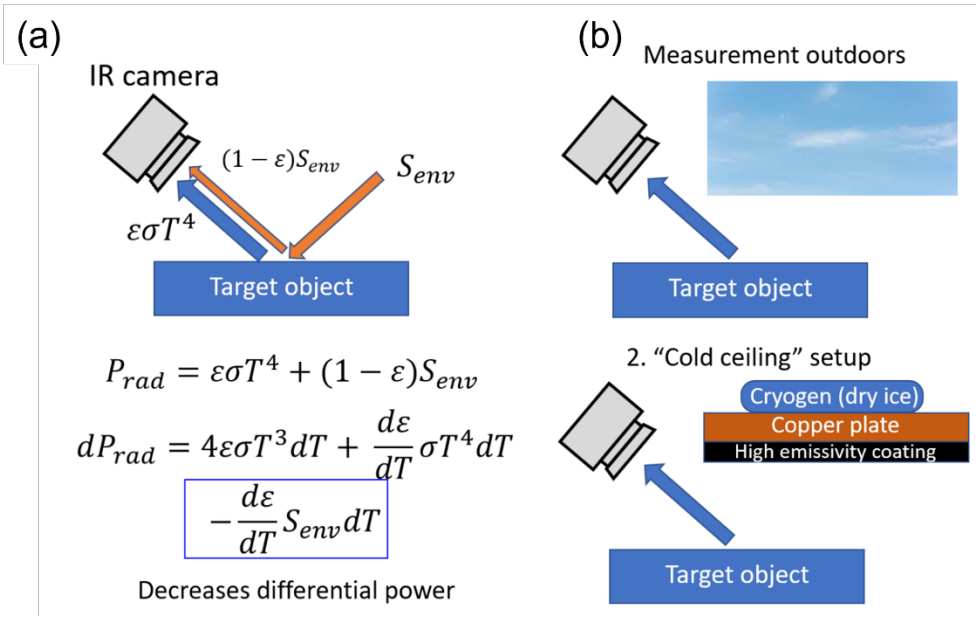


Figure 3.4. Schematics for the setups to minimize impact of IR signals from surrounding environment to optimize sensitizing effects. (a) Schematic and equations to demonstrate the impact of environmental radiation, which is denoted as S_{env}. (b) Setups to minimize the impact from S_{env}, either by doing the experiment in an outdoor environment with a clear sky or using a "cold ceiling" setup. The "cold ceiling" is made by a ~1 mm thick copper plate with high-emissivity coating facing the target object and cooled by cryogen such as dry ice. These two setups were applied throughout the IR camera measurement in this work and were comparable in the effect of optimizing sensitizing performance.

3.2.4. IR camera Characterization

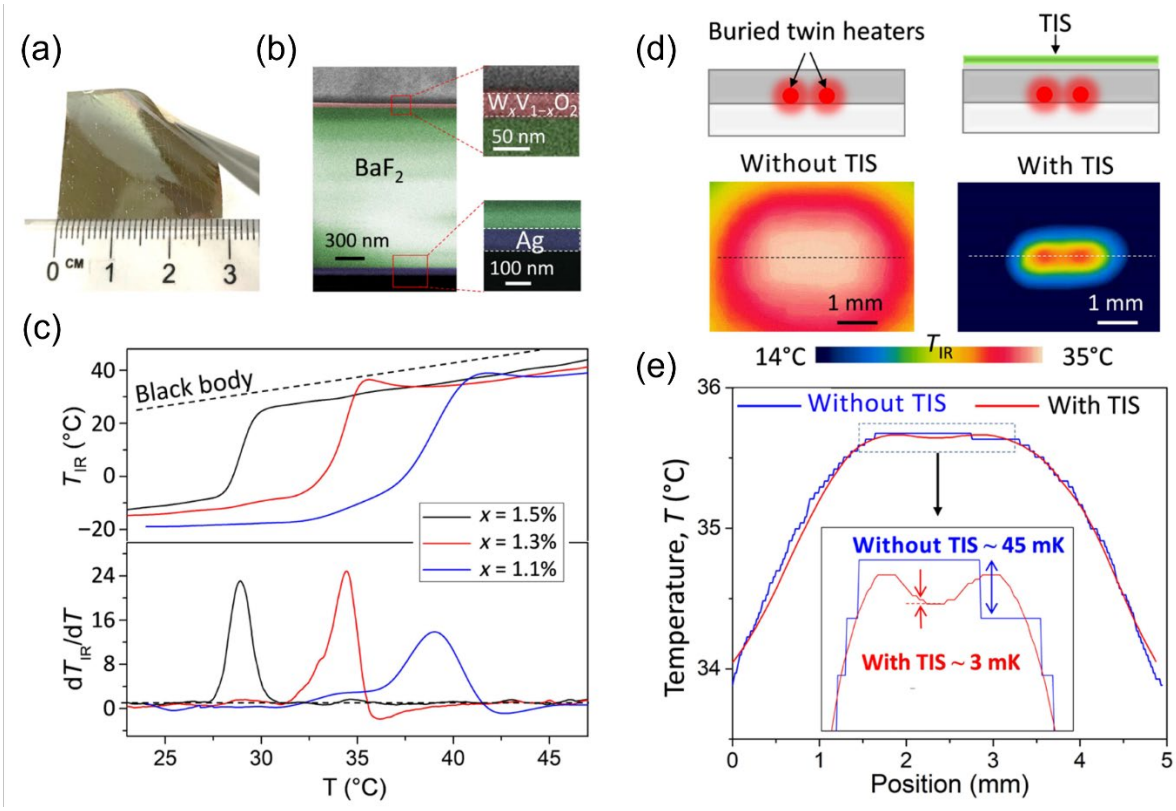


Figure 3.5. (a) Optical image of a fabricated TIS, showing high flexibility. (b) False-colored cross section of the TIS film imaged by scanning electron microscopy (SEM) before transfer. (c) IR temperature and temperature amplification as a function of actual temperature for TIS with three selected compositions (fractions of W in the $W_xV_{1-x}O_2$ layer). (d) Schematics and directly captured IR images of two closely placed (1-mm gap) small heaters imaged without and with TIS. (e) Calibrated temperature profiles along the dashed lines in (d). The twin-heater feature is distinctly resolved in the TIS-assisted imaging because of the ~15 times improvement of the experimental thermal sensitivity.

Figure 3.5(c) plots T_{IR} as a function of T in the upper panel, called the sensitizing property curve (SPC), for three selected TIS's with W fractions of 1.5, 1.3, and 1.1%. These samples exhibit sharp increase in T_{IR} at T ~ 28°, 34°, and 39°C, respectively, corresponding to the designed T_{MIT} of the $W_xV_{1-x}O_2$ layer. The sharp increase in T_{IR} at MIT is consistent with emissivity measurement by Fourier transform IR spectroscopy (Figure 3.6). Because T_{MIT} can be pre-set by the W fraction x, and the T_{MIT} of TIS, along with its working temperature range, can be precisely designed to fit various applications.

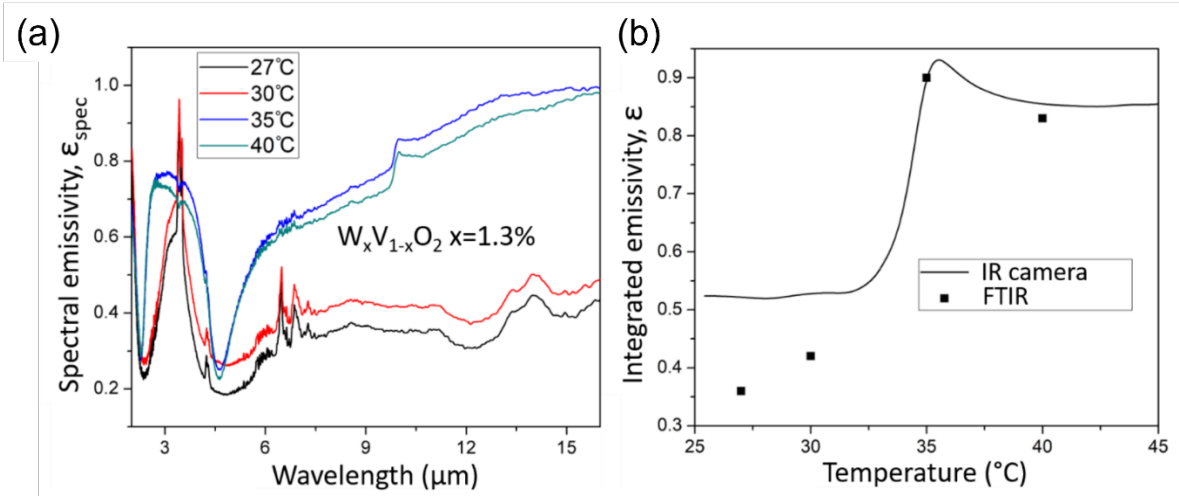


Figure 3.6. Emissivity of TIS measured by Fourier-transform infrared spectroscopy (FTIR) and the IR camera. (a) Spectral emissivity of a TIS measured by FTIR at different temperatures. An abrupt increase of emissivity is observed when the temperature increases above 35 °C, which is the metal-insulator transition (MIT) temperature of the $W_xV_{1-x}O_2$ (x = 1.3%) in this TIS. (b) The integrated emissivity over the 8-14 μm wavelengths (air transparency window) from the FTIR results, together with the results directly obtained by the IR camera. The higher emissivity extracted from the IR camera measurement is probably caused by signals contributed from environmental radiation, which is minimized but cannot be completely eliminated in the experiments (similar minimization effect between the outdoor and the cold ceiling setup).

The high dT_{IR}/dT enables drastic improvement of NEDT when taking IR images of objects coated with TIS, removing the artificial step features on the temperature profile while preserving good fidelity (Figure 3.7). The power of TIS is further demonstrated by the "Rayleigh criterion"–like experiment in Figure 3.5(d). Here, two small heaters made from tungsten wires were separated by 1 mm. The heaters are attached on a 2-mm-thick and 2 cm by 2 cm large paper board substrate (white block in the figure). A few layers of 0.5 cm by 1 cm large black carbon tapes are then stacked on the top of the heaters, with a total thickness of ~1 mm (gray block in the figure). The emissivity of the top layer is 0.90 to 0.95. Then the improvement of experimental sensitivity can be experimentally extracted from the converted T map by analyzing the size of artificial step features. For example, in the line profile crossing the centers of the two heaters in Figure 3.5(e), the two lobes of the heaters are indistinguishable, because the difference between the temperatures at the two peak points and the center dip is smaller than the experimental NEDT of the camera (~45 mK). In contrast, sensitizing with TIS results in a reduction in the system's NEDT by 15 times down to ~3 mK, thus making it possible to resolve the twin heaters. Note that for TIS-assisted IR imaging, T_{IR} recorded is not the actual temperature (T), but it could be readily calibrated back to T (Figure 3.5(e)) using the SPC in Figure 3.5(c).

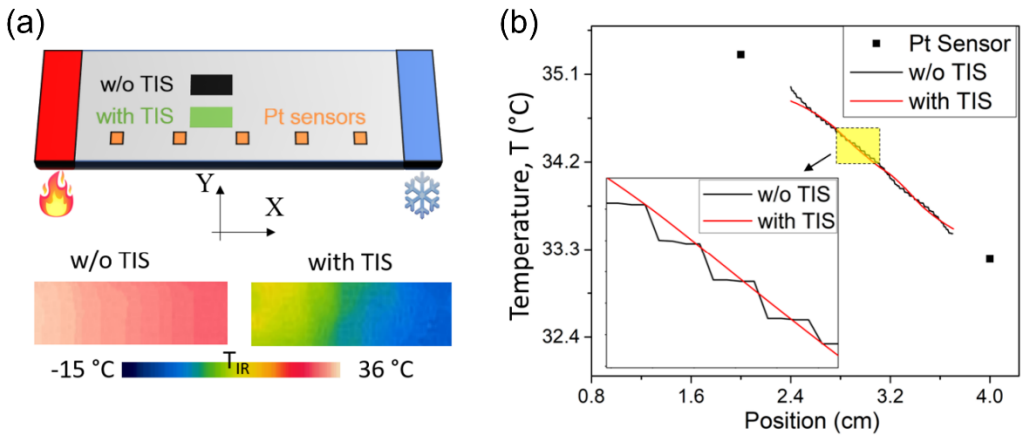


Figure 3.7. Improvement of IR imaging on a general thermal gradient by TIS. (a) Schematic and IR image of a high-emissivity coating (w/o TIS) placed next to a TIS film (with TIS) on a surface with known temperature gradient. Note that the "w/o TIS" and "with TIS" areas have the same real temperature gradient. (b) Temperature profile on the surface by IR imaging without TIS, with TIS, and locally read by platinum resistance temperature detectors (Heraeus Sensor Technology). The Pt thermocouples readouts served as verification of the temperature gradient in IR images. TIS enables much finer measurement of the temperature distribution, eliminating the artificial step feature caused by the experimental IR camera sensitivity limit (~ 45 mK).

Therefore, the application of TIS, which much reduces the NEDT, also contributes to the improvement of spatial resolution (D_r), especially in cases where the temperature gradient on the surface of object (∇T) is small, following a simplified equation as below

$$D_r = D_{r,c} + \mathrm{NEDT} \,/\, |\nabla T| \tag{3-3}$$

In which $D_{r,c}$ is the instrumentally limited spatial resolution of the camera.

3.2.5. Robustness Against Viewing Direction and Nonuniformity

Furthermore, the TIS can be applied to most near-ambient applications over the desired window of temperatures near T_{MIT}. Because T_{MIT} can be pre-set by the W fraction x, the T_{MIT} of TIS, along with its working temperature range, can be precisely designed to fit various applications. In addition, the angular independence of the SPC (Figure 3.8) and the mechanical flexibility allow TIS to be applied to non-flat, arbitrary surfaces with little impact to the performance.

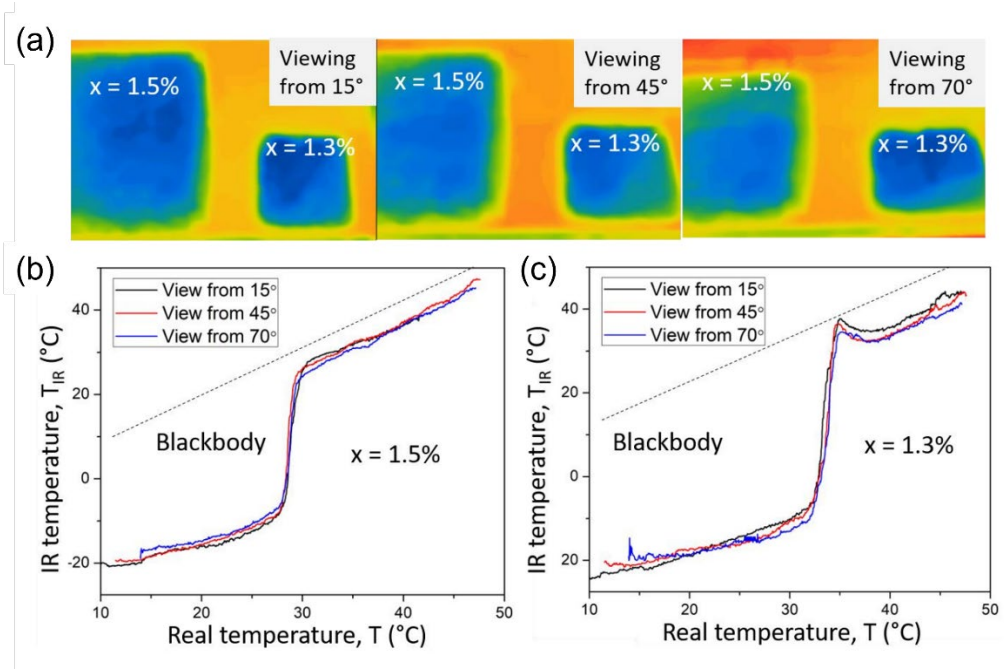


Figure 3.8. IR temperature (T_{IR}) as a function of real temperature (T) for two TIS samples imaged from different angles. (a) IR images of the two TIS samples with x = 1.5% and x = 1.3% in the $W_xV_{1-x}O_2$ layer, taken from different viewing angles. (b)-(c) T_{IR} (viewed from different angles) plotted as a function of T for the TIS with x = 1.5% and x = 1.3%, showing angular independence of the T_{IR}(T) curves.

All the IR images in the figures show the map of T_{IR}, which represent thermal features of the object but is numerically different from a map of T in the case of imaging with TIS. A map of T can be readily converted from the above T_{IR} image using the SPC data: At each pixel of the image, by matching the T_{IR} with SPC in Figure 3.5(c), the actual temperature T can be obtained. Note that this approach also works in the case when the TIS sensitization is spatially inhomogeneous, as long as the SPC of each pixel is measured and applied in the conversion to the image of T. As shown in Figure 3.9(a), when we deliberately selected a TIS sample with many defects and significant performance nonuniformity, the initially generated an T_{IR} image is severely deviated from the actual thermal feature. To calibrate the TIS-assisted T_{IR} image, the TIS was attached to a thermal stage with spatially uniform temperature, and T_{IR} images were sampled at N different real temperatures (T) of the thermal stage (which cover all working temperatures of TIS). Therefore we get a 3D matrix T_{IR} S (X,Y,N) containing the necessary T_{IR}-T response information of the whole TIS. With interpolation based on T_{IR} S (X,Y,N), pixel-by-pixel calibration of the defective raw IR image in panel A is executed. This calibration algorithm significantly improves the raw IR

image and reproduces the actual rod-shape thermal pattern, without the loss of enhanced temperature resolution by TIS (Figure 3.9(c)). Future large-scale applications of TIS would also benefit from this calibration procedure to eliminate spatial inhomogeneities.

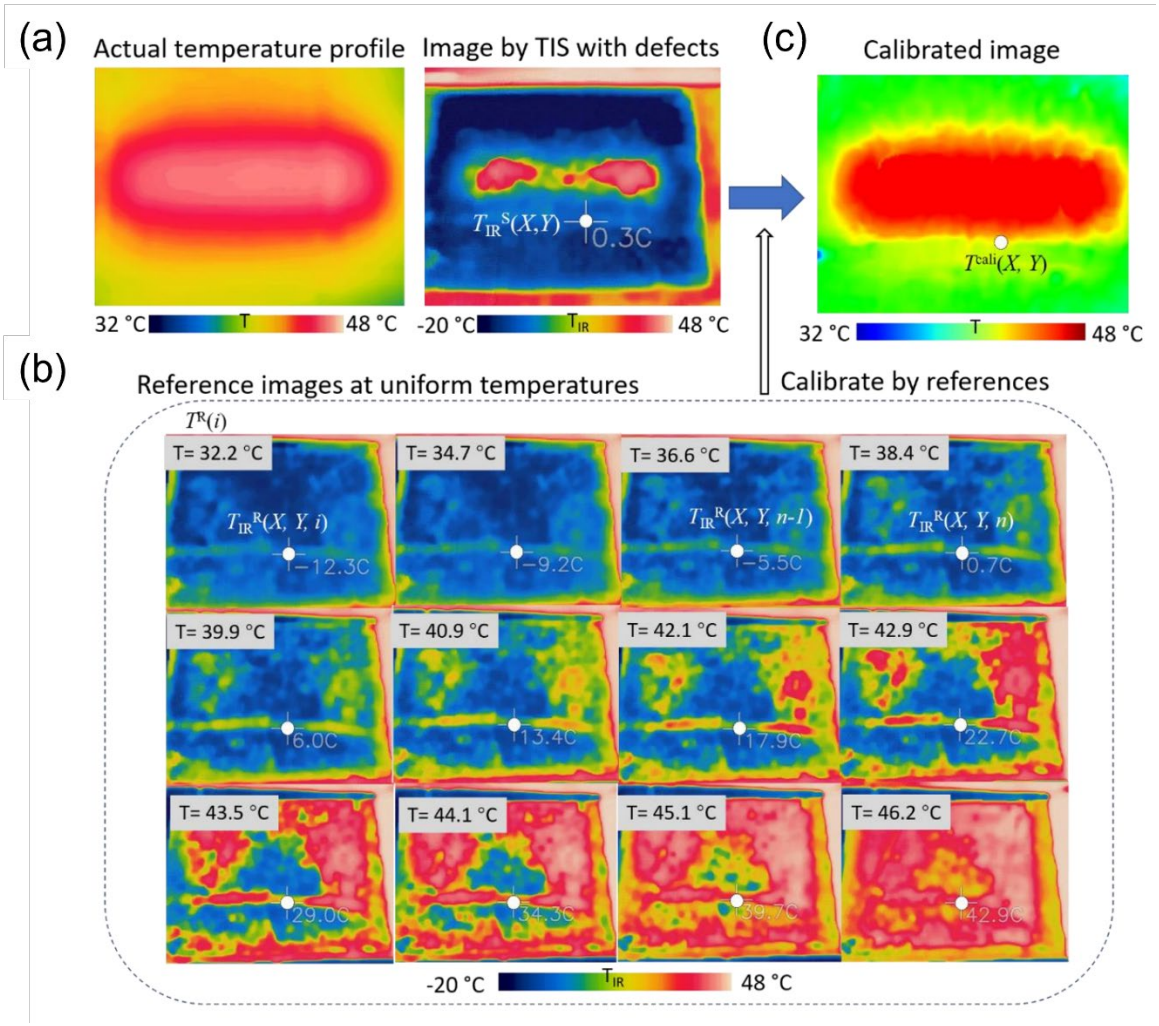


Figure 3.9. Temperature calibration for a TIS with significant defects and nonuniformity. (a) Actual temperature profile (obtained by conventional IR imaging) and an IR image assisted by a defective TIS of a surface with a rod-shaped thermal feature. (b) Collection of reference images for temperature calibration. Note that only a part of the sampled T_{IR} images was presented in this panel for simplicity. (c) Calibration result.

3.3. Operando Electronics Analysis (oEA) Applications

As a fast, convenient, and nondestructive detection method, thermography is widely used in imaging thermal profiles of electronics, including tests for thermal-via structures [45], screening of voids at thermal interfaces [46], failure analysis in electronics packaging [47], reliability estimation of PCBs [48], and investigation of lateral electronic inhomogeneities [49].

The substantial reduction in NEDT greatly benefits thermal imaging of electronics. Ultrasensitive passive thermal imaging can probe the operation status of electronic devices and is especially useful for scenarios where lock-in amplification is not available. The over 15 times sensitization enables accurate detection of very weak thermal features in electronic circuits. The TIS-assisted thermal imaging engenders a new technology that we call in operando electronics analysis (oEA). The oEA extends the application of thermography from inspecting defective devices to normal devices in operation. By analyzing extremely weak thermal features on the surface of the device, oEA noninvasively "spies" on and reveals the working mode of the device in real time.

3.3.1. Thermography for Integrated Circuit Packages

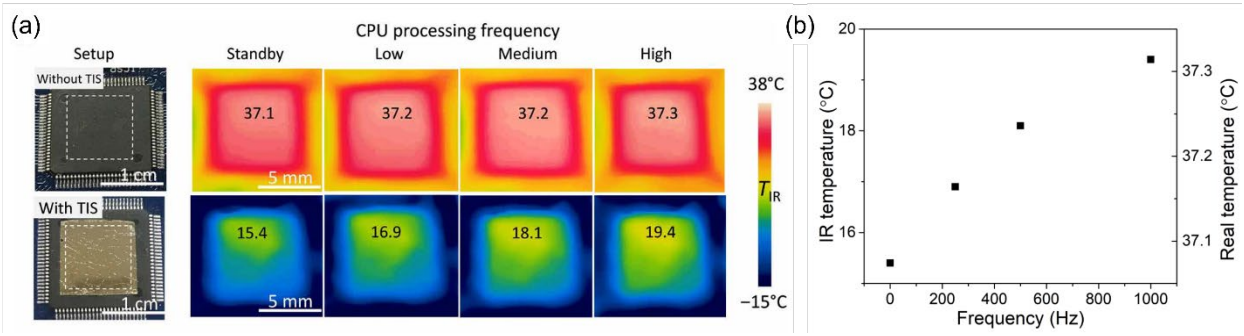


Figure 3.10. (a) Enhancement of thermographic contrast on a processor by TIS, allowing differentiation of various working modes. (b) Maximal surface temperature of the processor unit as a function of the working frequency measured in (a).

Figure 3.10 demonstrates thermographic differentiation of distinct workloads and operation modes of a processor. The oEA was performed on the processor chip (ATmega2560). In different modes characterized by IR imaging, the processor reads temperature data and exports terminal voltages at various frequency, which is 0 Hz for the standby mode, 250 Hz for the low-frequency mode, 500 Hz for the medium-frequency mode, and 1000 Hz for the high-frequency mode. For all conditions, there was a background thermal feature, probably arising from the background operation (including power supply, clocking, etc.) of the processor unit. A correlation of the peak IR temperature at the processor surface and the reading/exporting frequency is shown in Figure 3.10(b).

In the weak electrical heating demonstration (Figure 3.11), the chip was a TS3A44159 quad single-pole double-throw analog switch with two controls (Texas Instruments). The current was applied from the COM1 terminal to the NC1 terminal at on-state of this channel. For optimal demonstration, the background IR image without the applied current was subtracted from the one with current, which generates images of ΔT_{IR} caused by joule heating.

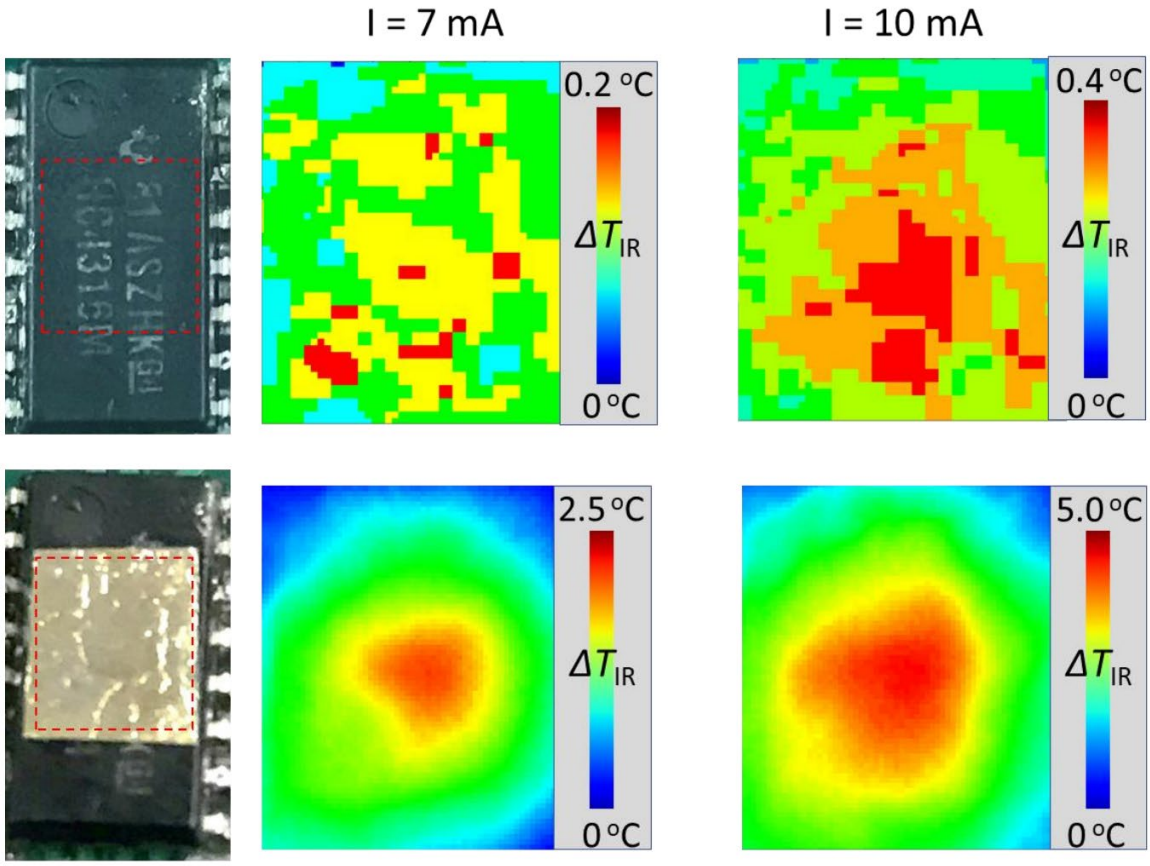


Figure 3.11. A SPDT switching chip with various input currents, imaged without and with TIS. Imaging with TIS coating enables accurate observation and detailed evaluation of vague thermal profile on the chip caused by weak Joule heating that are otherwise undetectable.

3.3.2. Electric Operation Parameters Probing

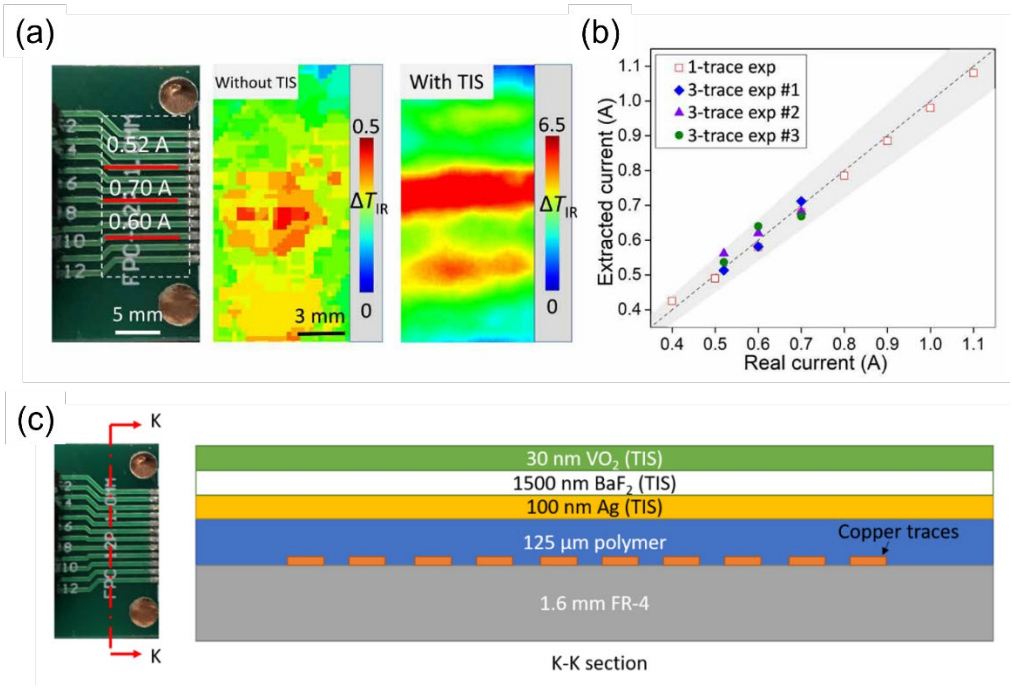


Figure 3.12. (a) Optical and IR mappings of temperature rise because of currents flowing in adjacent circuit traces on a printed circuit board (PCB), imaged without and with TIS. (b) Extracted current versus real current in the traces. The dashed line and the shadow correspond to the ideal current extraction and ±10% deviation, respectively. The experimental error bars for the data points are comparable to the size of the points. (c) Cross-sectional view of the model with partial geometric parameters used in the simulation. The total thickness of the polymer layer (representing scotch tape, glue, soldermask, etc.) is calculated based on the individual thickness of each material. The copper traces are 35 μm thick and 0.5 mm wide, with a 0.5 mm gap between adjacent traces.

The oEA can be further extended from qualitative probing to quantitative extraction of electronic operation parameters, such as electrical current flowing in wires and circuit traces. By calibrating local temperature rise from the joule heating, the current levels in the circuit traces can be evaluated thermographically at high accuracy without interrogation with current meters. The operation can be performed simultaneously for multiple, adjacent traces on a circuit board, allowing noninvasive and quantitative current mapping.

The quantitative oEA (Figure 3.12) was performed on a PCB with parallel circuit traces purchased from Uxcell. A finite-element analysis using the heat transfer module of COMSOL Multiphysics was developed to simulate the surface thermal profile at different current inputs. The surrounding air temperature (influenced by the cold plate) was calibrated based on the thermal profile of a single circuit trace with current from 0.4 to 1.1A. Most organic components (polypropylene, polyvinyl alcohol, epoxy, etc.) in the polymer layer have similar thermal properties [50-52]. Therefore, for simplicity, the polymer layer material is set to be polypropylene (the main component of the scotch tape used) [50]. Other material properties are from references [51-57]. The heating power in copper circuit traces is calculated using Joule–Lenz law with the copper conductivity of 6×107 S/m. The temperature of the thermal stage beneath the whole structure is

33.6 °C. To calculate the steady-state temperature profile of the TIS surface, the convective heat transfer coefficients of the air is set at 5 W/(m^2·K). Based on the thermal profile of the single-trace experiments (Figure 3.13(a)-(b)), the temperature of surrounding air is fitted to be 3.0 ºC. Note that the numerical thermal profiles in Figure 3.13 are evaluated at the very top surface of TIS in the model.

The model was then applied to map the currents in three traces with different experiment setups, which were then compared with the actual currents flowing in the circuit traces. Detailed information of the modeling can be found in Figure 3.13 and Table 3.1. As an additional benefit, the coverage of TIS can eliminate the effect of emissivity variation across the object surface in thermal imaging, which is typical for PCBs.

	Polypropylene	Ag	BaF2	VO2	Cu	FR-4
Thermal conductivity ($W*m^{-1}K^{-1}$)	0.24	275	11.72	4	400	0.343 (cross-plane) 1.059 (in-plane)
Specific heat ($J*kg^{-1}K^{-1}$)	1731	240	410	700	390	1369
Density ($g*cm^{-3}$)	0.91	10.49	4.89	4.67	8.9	1.9

Table 3.1. Material properties used in the simulation.

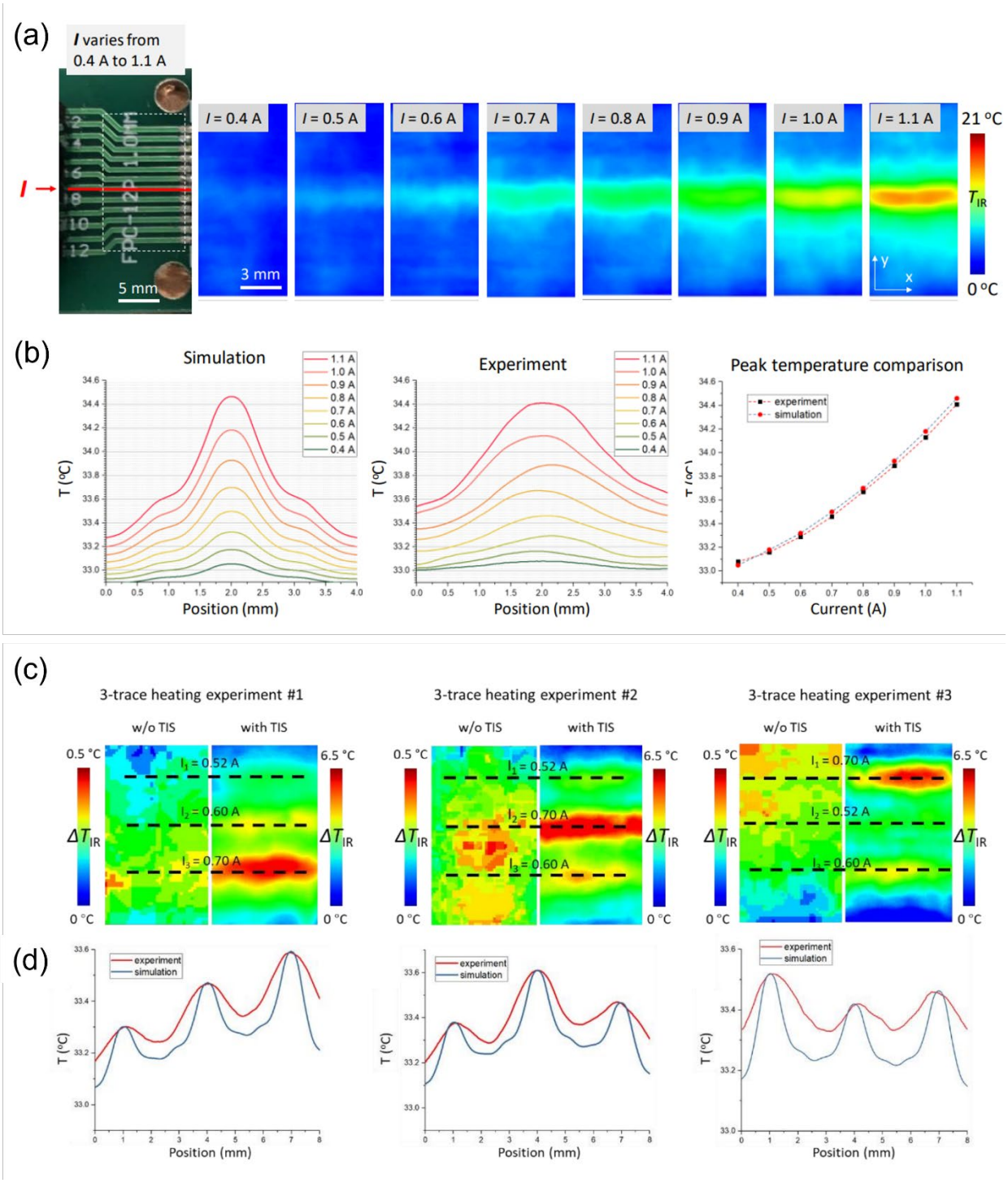


Figure 3.13. Calibration of the model based on thermal profiles of a single circuit trace, and extraction of the currents for 3-trace heating experiments. (a) Optical and IR images of current flowing through a single trace in PCB (IR images were taken with TIS coating). (b) Comparison between simulated and experimental thermal profiles in Y-direction. Note that the experimental thermal profiles were obtained by averaging over the X-direction through the IR images shown in (a). (c) IR images for three different experiments without and with TIS. (d). Representative current extraction in those three traces by fitting the simulated thermal profile to the experimental results.

3.4. Medical Thermography

The TIS also empowers groundbreaking advance in medical thermography [35]. Thermography is broadly applied in areas such as cancer detection [58], diagnosis of diabetic neuropathy and vascular disorder [59], fever screening [60], dental care [61], and surgery [62]. Breast cancer, for example, can be detected by IR cameras because hypervascularity in the tumors leads to slightly abnormal local temperature. With the advantages in cost, accessibility, and noninvasiveness, thermography is used to screen breast cancer before mammography testing [63]. However, current medical thermography suffers from the low diagnostic sensitivity and specificity [64], while TIS-assisted thermography would reduce noise, improve thermographic fidelity, and enable cancer screening at earlier stages, potentially improving the survival rate of patients [65].

All the following medical thermography experiments were performed at Department of Molecular & Cell Biology, UC Berkeley. IRB and/or IACUC guidelines were followed with human or animal subjects.

3.4.1. Cancer Screening

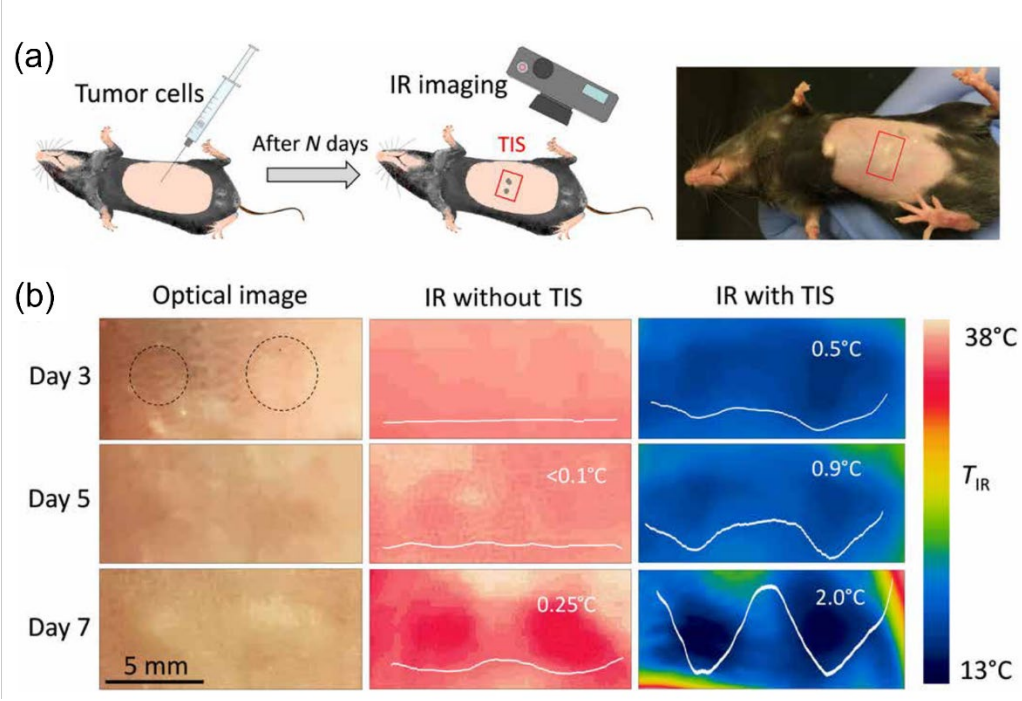


Figure 3.14. TIS applied to cancer screening. (a) RMA cells were injected at two adjacent spots to initiate the tumor growth in mice, which was then tracked by optical imaging, IR imaging without TIS, and with TIS. (b) TIS imaging reveals the two tumors in early stage after the injection when they are not yet detectable visibly or by conventional thermography. The white curves are temperature profiles across the center of the two tumors in each IR image, labeled with the amplitude of T_{IR} variation in each curve.

We demonstrate the benefit of TIS in subcutaneous cancer screening by tracking the growth of malignant tumors in mice. Figure 3.14(a) shows the schematic of the experiment and the picture of a laboratory mouse. RMA cells, belonging to the lymphoma cell line, were injected at two near

spots on the mouse belly to initiate the tumor growth. On different days after the injection, an optical image, an IR image without TIS, and an IR image with TIS were taken to characterize the tumor (Figure 3.14(b)). On day 3 after the cell injection, no features were detected in the optical or conventional IR imaging, while cold spots at the two tumors were clearly captured in the TIS-assisted IR imaging. As the tumors grow larger on day 5, they could be barely observed visibly and by conventional IR imaging, while the IR imaging of the cold spots becomes much clearer and more confirmative with the TIS. On day 7, the tumors are large enough to be detected in all imaging methods, and the consistency of these features validates the TIS-assisted imaging in the early stage of the tumor. As we show in Figure 3.15, the benefit of TIS can be also extended to detecting other types of tumor cells, imaging the shape and size of tumors, and resolving multiple tumors when they are closely situated, similar to the scenario in Figure 3.5(e).

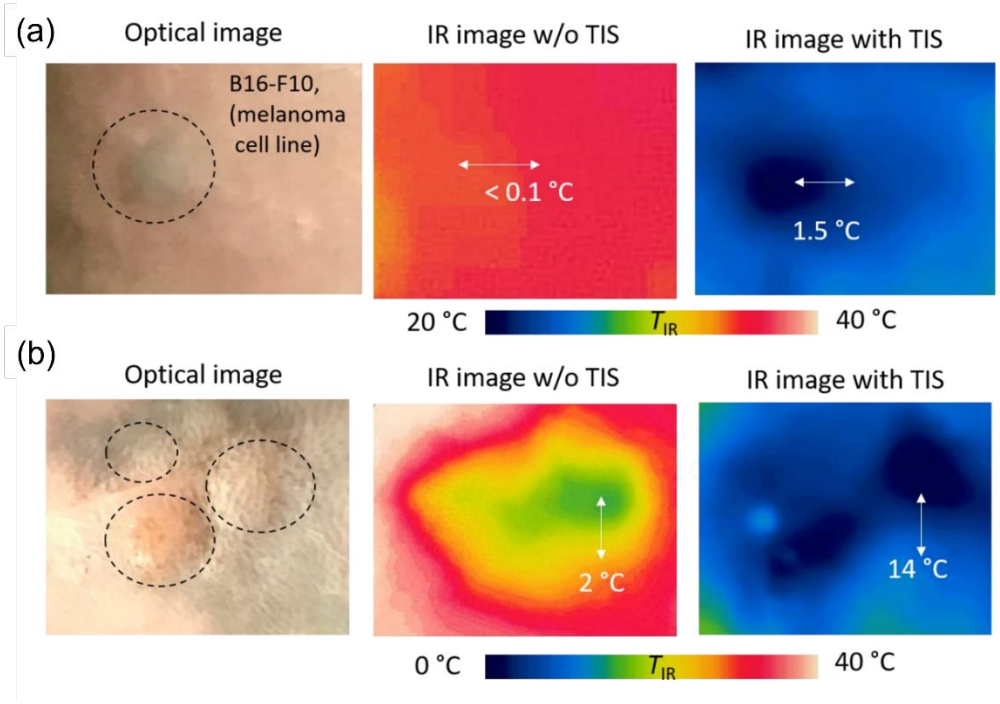


Figure 3.15. Supplementary results for the enhancement of IR imaging of tumors in mice. (a) Imaging of a tumor induced by injecting B16-F10 cells, which is a melanoma cell line distinct from the type applied in Figure 3.14. TIS demonstrates similar advantages in detecting tumors earlier than conventional IR imaging. (b) Imaging of three RMA tumors injected close to each other. Due to the limit of sensitivity, conventional IR imaging is unable to resolve those three tumors, while they can be distinguished clearly with the help of TIS.

3.4.2. Experimental Details for in Vivo Tumor Growth

RMA cells were cultured in RPMI 1640 (Thermo Fisher Scientific) and B16-F10 cells (obtained from University of California, Berkeley, Cell Culture Facility) were cultured in Dulbecco's modified Eagle's medium (Thermo Fisher Scientific). In all cases, media contained 5% fetal bovine serum (Omega Scientific), glutamine (0.2 mg/ml; Sigma Aldrich), penicillin (100 U/ml; Thermo Fisher Scientific), streptomycin (100 µg/ml; Thermo Fisher Scientific), gentamycin

sulfate (10 µg/ml; Lonza), 50 µM β-mercaptoethanol (EMD Biosciences), and 20 mM Hepes (Thermo Fisher Scientific), and the cells were cultured in 5% CO_2.For tumor growth experiments, RMA or B16-F10 cells were washed and resuspended in phosphate-buffered saline (Thermo Fisher Scientific) and injected subcutaneously into the belly of C57BL/6J mice (originally obtained from the Jackson laboratory) at a dose of ~105 cells in a total volume of 50 µl per injection site. The tumor growth was monitored daily. Note that as opposed to the hypervascularity around the natural cancer cells for human, the artificially introduced tumors in mice typically have impaired blood supplies, mainly because of the much faster growth rate of these tumors and the immunodeficiency of laboratory mice, causing a slightly lower local temperature, instead of higher as in the case of human.

3.4.3. More on Medical Thermography

Besides cancer screening, IR imaging of blood vessels is also critical for intravascular sampling of venous blood, intravenous injections of drug solutions [66], monitor of health parameters such as blood pressure [67], and diagnostics of circulatory disorders [68]. This requirement can also be readily met with the millikelvin sensitivity enabled by TIS, which shows a clear improvement in the imaging of cephalic veins (Figure 3.16). We note that the scope of TIS application goes much beyond the limited cases demonstrated in this work and can be extended to most areas of medical thermography, including checking of musculoskeletal disorders [69], diagnosis of rheumatic diseases [70], dermatological applications [71], evaluation of trans-plantation [72], and imaging of brain activities [73].

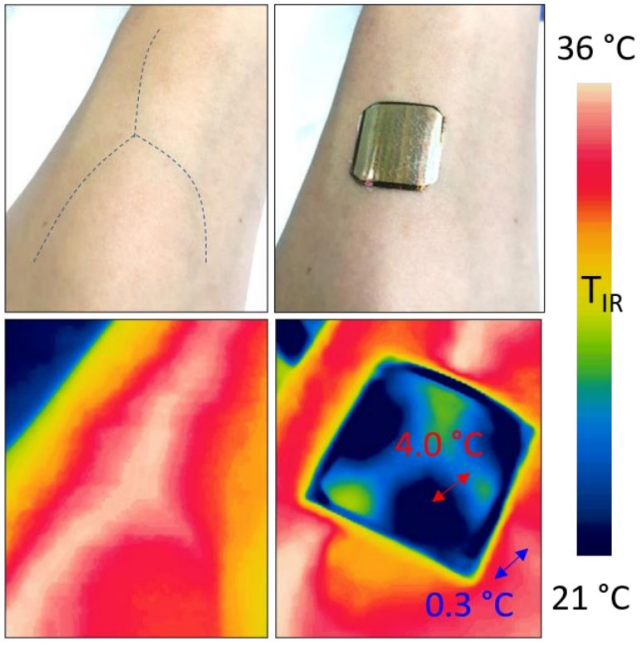


Figure 3.16. Imaging of cephalic veins on a human forearm without and with TIS. The IR image of the crossing point of veins is enhanced by over 10× in IR temperature contrast by the TIS coating.

3.5. Summary

Integrating the thermally driven metal-insulator phase transition with a resonant photonic structure, we innovate ambient thermography by drastically refining the temperature sensitivity to single digits of millikelvin. The TIS expands the applications of ambient thermography in electronics analysis and medical screening. As small temperature fluctuation exists over the surface of a wide range of objects and, in many cases, implicates unusual subsurface thermal activities, the TIS is envisioned to broadly affect many other fields (Figure 3.2(c)). For example, at larger scales, the TIS-assisted thermography may be used to inspect, image, and monitor subsurface cracks and stressed spots in buildings and bridges [74]; at smaller scales, with the aid of high-resolution IR microscopy, the TIS may act as functional templates on which biological activities of cells and microbes can be thermally imaged in real time.

For broader applications in practical scenarios, TIS is also open to improvements in multiple prospects by future endeavors. For example, more delicate control in the W doping of VO_2 will allow for finer tuning of the working temperature to optimize performance for various conditions. Doping with other elements like Ga or Al may shift the working temperature above that of pristine VO_2 (67°C) to enable applications at higher temperature. Future engineering efforts to improve the quality of $W_xV_{1-x}O_2$ can improve the sharpness of MIT and the reduction in NEDT, further boosting the performance in sensitivity and resolution. Last, the response time of the device could be shortened by reducing the thickness of the flexible substrate film and improving the thermal contact with the target surface.

4. Temperature-adaptive Radiative Coating (TARC) for Year-round Energy Saving

4.1. Introduction

4.1.1. Cool Roofs and Their Limitations

Apart from thermography, engineering the emissivity of materials also finds its applications in cool roofs. In countries such as the United States, ~39% of the total energy consumption is in buildings [75]. For the residential housing energy portion, ~51% is consumed for heating and cooling to maintain a desirable indoor temperature (~22°C) [76]. Thus, improving the energy efficiency of the heating, ventilation, and air conditioning (HVAC) systems with passive radiative cooling roof materials (cool roofs) has gained attention from researchers and government agencies.

In contrast to most temperature regulation systems, which require external power input, the cool roofs utilize the thermal radiation exchange between terrestrial surfaces and the 3 K outer space through the mid-infrared (IR) atmospheric transparency window ("sky-window", Figure 4.1). This method to cool an outdoor surface such as a roof has been extensively studied in the past [77–80]. It is now advanced by the development of daytime radiative cooling [81–87] using materials with low solar absorptance and high thermal emissivity in the form of thin films [82], organic paints (84,88), or structural materials [85].

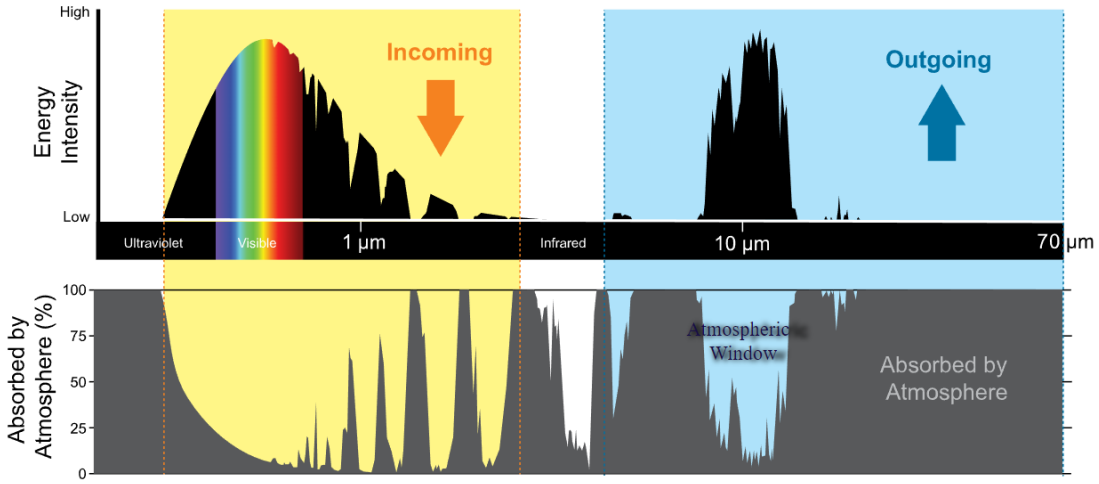


Figure 4.1. Atmospheric window. The upper panel showed the intensity of the thermal radiation exchange between the earth and outer space, including the solar radiation (incoming) and thermal radiation of terrestrial objects (outgoing). The lower panel shows the absorptance of atmosphere. The low-absorptance wavelength ranges are called atmospheric window [89].

Past research on daytime radiative cooling, while successful in reducing cooling energy consumption, typically used materials with fixed, cooling-optimized properties, which efficiently emit thermal radiation even when the temperature of the surface is lower than desired, such as during the night or in the winter. This unwanted thermal radiative cooling will increase the energy

consumption for heating and may offset the cooling energy saved in hot hours or seasons. This issue is well acknowledged by the research community, and mitigation of the overcooling has become a timely demand [90].

4.1.2. Solutions to the Overcooling

To cut the heating penalty from overcooling, a few techniques were recently attempted for switching off thermal radiative cooling at low temperatures (below 22°C). Although effective in switching, these techniques typically require either additional energy input [91,92] or external activation [93], and in some cases, switching is achieved by mechanical moving parts [94,95]. Developing dynamic structures that automatically cease radiative cooling at low temperatures is therefore highly desirable. Existing efforts in self-switching radiative cooling, however, are either purely theoretical [96–99] or limited to materials characterization with little relevance to practical household thermal regulation [16,100–102]. Very recently, a smart sub-ambient coating was developed [103], focusing on the reduction of solar absorption by fluorescence rather than modulation of thermal emissivity by temperature.

In this chapter, we took a different, holistic approach by designing and fabricating a mechanically flexible coating structure to minimize total energy consumption through the entire year. This temperature-adaptive radiative coating (TARC) automatically switches its sky-window emissivity to 0.90 from 0.20 when the surface temperature rises above ~22°C, a practical threshold not previously available. Our TARC delivers high radiative cooling power exclusively for the high-temperature condition (Figure 4.2). The solar absorptance at ~0.25 (solar reflectance = 0.75) is also optimal for all-season energy saving in major US cities. Our TARC demonstrates effective surface temperature modulation in an outdoor test environment. We performed extensive simulations based on the device properties and the climate database, which show advantages of TARC over existing roof coating materials in energy savings for most US cities indifferent climate zones (Details in Section 4.6). The energy savings by TARC not only bring economic benefits but also contribute to environmental preservation by reducing greenhouse gas emissions.

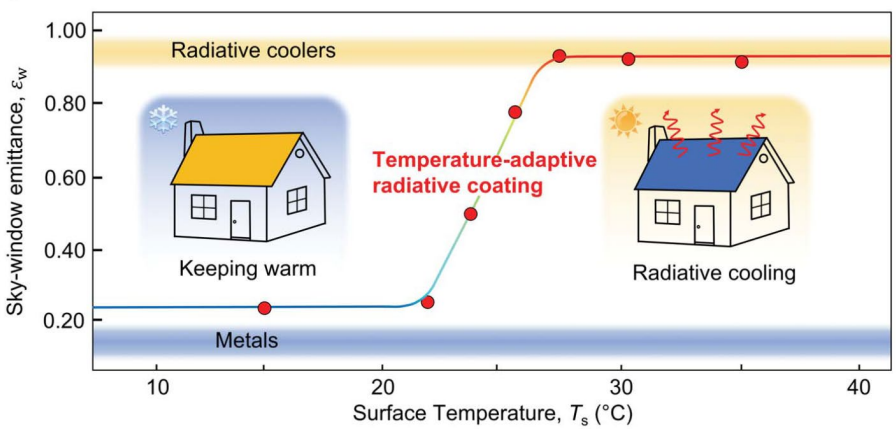


Figure 4.2. Basic property of TARC in sky-window (8 to 13mm) emissivity modulation and schematics for temperature management when used as a household roof coating. The data points are the measured sky-window emissivitys of a TARC. The two-color bands represent the temperature-independent thermal emissivity of metals and radiative coolers.

4.2. Working Principle of TARC

We developed the TARC based on the well-known metal-insulator transition (MIT) of the strongly correlated electron materials $W_xV_{1-x}O_2$ [104, 105], and the transition temperature (T_{MIT})is tailored to ~22°C by setting the composition at 1.5% [17]. We embedded a lithographically patterned two-dimensional array of thin $W_xV_{1-x}O_2$ blocks in a BaF_2 dielectric layer that sits on top of an Ag film (Figure 4.3(a)). In the insulating (I) state of $W_xV_{1-x}O_2$ at $T<T_{MIT}$, the material is largely transparent to the infrared (IR) radiation in the 8 to13 mm sky spectral window, so this sky-window IR radiation is reflected by the Ag mirror with little absorption [107]. By contrast, the $W_xV_{1-x}O_2$ becomes highly absorptive in the sky window when it switches to the metallic (M) state at $T>T_{MIT}$. The absorption is further amplified by the designed photonic resonance with adjacent $W_xV_{1-x}O_2$ blocks as well as with the bottom Ag layer through the ¼-wavelength cavity. The ¼-wavelength cavity structure induces Fabry-Perot resonance and was used in previous work to enhance thermal emission [96, 98]. According to Kirchhoff's law of radiation, the sky-window emissivity equals the sky-window absorptance and switches from low to high when the temperature exceeds T_{MIT}. Consequently, strong sky-window radiative cooling is turned on in operation exclusively at high temperatures, leaving the system in the solar-heating or keep-warm mode at low temperatures.

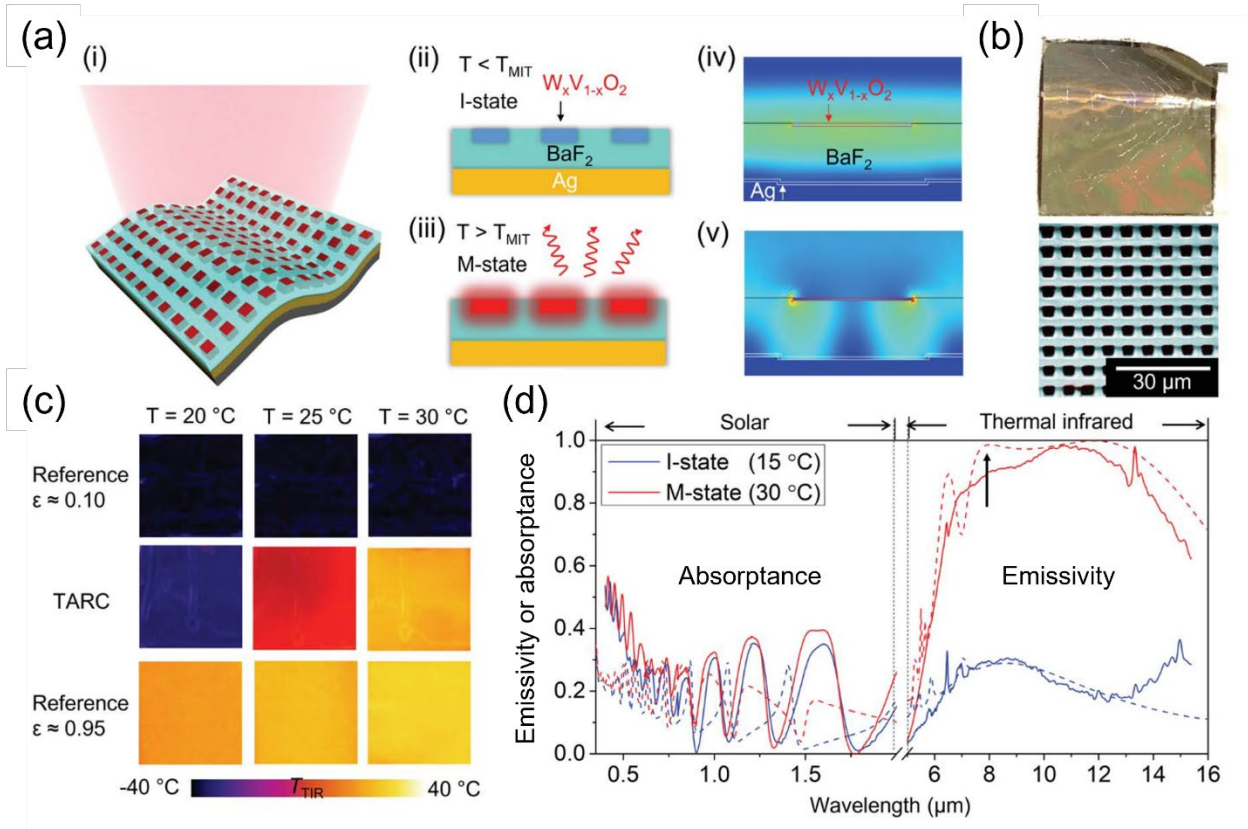


Figure 4.3. (a) Schematics of the structure (i), materials composition and working mechanism (ii and iii) of the TARC. Subpanels (iv) and (v) show the simulated distribution of electric field intensity below and above the transition temperature, respectively, when electromagnetic waves with a wavelength of 7.8mm were normally incident on the TARC structure. (b) Photograph (2 cm × 2 cm) and false color scanning electron microscope image of TARC showing high flexibility and structural consistency with the design. (c) Thermal infrared images of TARC compared with those

of two conventional materials (references) with constantly low or high thermal emissivity showing the temperature-adaptive switching in thermal emissivity of TARC. (d) Solar spectral absorptance and part of the thermal spectral emissivity of TARC at a low temperature and a high temperature, measured by a UV-visible-NIR spectrometer with an integrating sphere and an FTIR spectrometer, respectively. Measurements (solid curves) show consistency with COMSOL simulations (dashed curves). The arrow at 7.8mm denotes the wavelength where the distribution of electric field intensity shown in subpanels (iv) and (v) of (a) are simulated.

Our fabricated TARC has high flexibility for versatile surface adaption, as well as a micro-scale structure consistent with the design (Figure 4.3(b)). We examined the emissivity switching over the entire sample using a FLIR ONE infrared camera (Figure 4.3(c)). We imaged the TARC surface together with two reference samples having similar thicknesses but constant low thermal emissivity (0.10, copper plate) or constant high thermal emissivity (0.95, black tape), respectively. To minimize the reflection from the camera and the surroundings, the default viewing angle was set as 15° instead of normal incident direction, and the experiments were performed in an open-area, outdoor environment under a clear (cloud-free) sky. Although the thermal emission of the reference samples appeared to not be strongly temperature sensitive from 20 to 30°C, the TARC showed a marked change, corresponding to the switch in sky-window emissivity at the MIT around 22°C.

4.3. Fabrication Process

675 μm-thick Si wafers were first covered with an approximately 2 μm thick polyimide film (PI-2545, HD MicroSystems LLC) via spin coating, which was then cured in a N_2-filled oven at 425 °C for 60 minutes. The polyimide film acts as an etching protection layer for the final transfer process. $W_xV_{1-x}O_2$ thin films were grown on the polyimide layer using pulse laser deposition (PLD). The PLD target was prepared by mixing WO_3 and V_2O_5 powders with a W:V atomic ratio at 1.5%, then made into 2.5 cm diameter round discs with a hydraulic press. All $W_xV_{1-x}O_2$ thin films were deposited in a 5 mTorr O_2 environment at 500 °C substrate temperature, and the PLD laser energy was set at 321 mJ with 10 Hz pulse frequency. 70 nm of $W_xV_{1-x}O_2$ was grown at a rate of 6 nm/min, followed by a post-deposition anneal at 500 °C for 30 mins in the same 5 mTorr O_2 environment. The metamaterials patterns were made with standard photolithography, combined with etching of $W_xV_{1-x}O_2$ by SF_6+ O_2 in a plasma etching system. After removing the photoresist with acetone and O_2 plasma, 1.5 μm thick BaF_2 and 100 nm thick Ag layers were grown sequentially on top via thermal evaporation. The growth rates of BaF_2 and Ag were controlled at 20 Å/s and 2 Å/s, respectively.

In the transfer process, a piece of 0.06 mm thick single-sided sticky cellophane packaging tape was first carefully applied to fully cover the surface, where the Ag layer was stuck to the adhesive side without any residual air bubbles. An initial Si substrate removal process was performed in a HF + HNO_3 solution, mixed by aqueous HF (49% weight percentage) and HNO_3 solution (68% weight percentage) with a volume ratio of 10:1. The samples were taken out and rinsed with DI water to stop the initial etching when the etchant starts to touch down on the polyimide layer. A XeF_2 dry etching process was then carried out to clean off the residue Si. In the final step, the

polyimide protection layer was removed by O_2 plasma at 100 mTorr O_2 pressure and 200 W plasma power for about 11 mins.

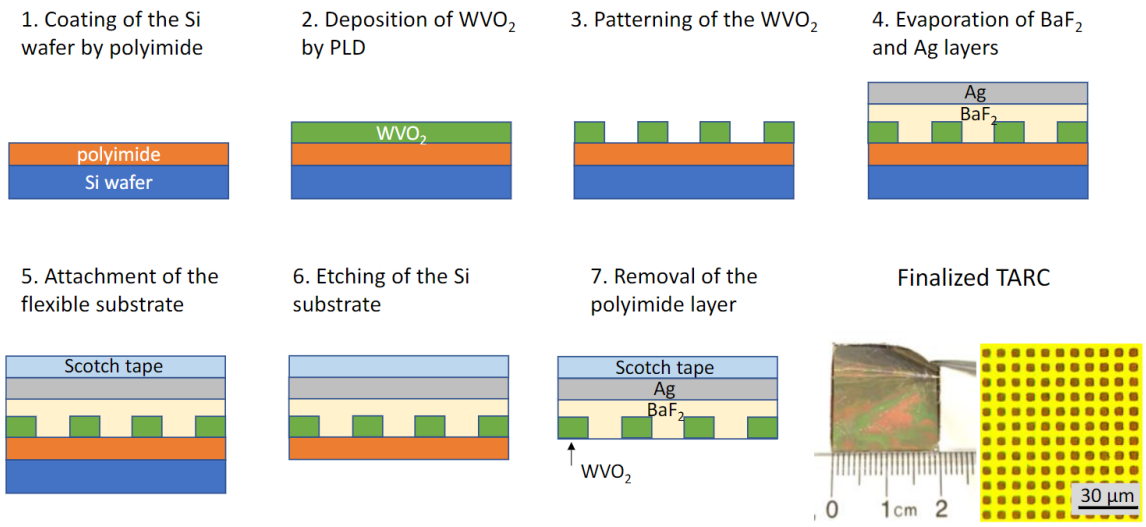


Figure 4.4. Schematics and pictures for the fabrication of TARC.

4.4. Experimental Characterizations

4.4.1. Spectrally Resolved Absorptance/Emissivity Measurements

We measured the spectral properties of the TARC by a UV-visible-NIR spectrometer and Fourier transform infrared spectroscopy (FTIR) for the solar and thermal infrared wavelength regimes, respectively (Figure 4.3(d)). The solar absorptance (A, 0.3 to 2.5mm) is ~0.25, and the sky-window emissivity (ε_w, 8 to 13mm) is ~0.20 in the I state and ~0.90 in the M state.

Near normal-hemispherical solar spectral reflectance, r(λ), was measured from 300 to 2,500 nm with an Agilent Cary 5000 UV-vis-NIR spectrometer equipped with an Internal Diffuse Reflectance Accessory (DRA-2500), which collects both specular and diffuse reflections. Solar spectral absorptance was computed as $a(\lambda)=1-r(\lambda)$ since the film was essentially opaque to sunlight. The solar absorptance A can be calculated from the corresponding spectral data by

$$A = \frac{\int_{0.3\mu m}^{2.5\mu m} I_s(\lambda)a(\lambda)d\lambda}{\int_{0.3\mu m}^{2.5\mu m} I_s(\lambda)d\lambda} \quad (4\text{-}1)$$

where Is(λ)is the solar spectral irradiance.

Thermal spectral reflectance at normal incidence, r(λ, T), was characterized by a Nicolet iS50 FTIR spectrometer and Nicolet Continuum microscope over the spectrum 5-15 μm. The objective lens was 32×with 0.65 numerical aperture. A blade aperture of 100 μm ×100 μm was used to select the area of interest. All reflection spectra were normalized to the reflection spectrum of a 300 nm thick gold film. The temperature of the samples (15-50 °C) was controlled by a customized closed-loop thermal stage, connected to a Lakeshore 321 temperature controller. Kirchhoff's law

of radiation states that in thermodynamic equilibrium, spectral emissivity ε(λ, T) equals spectral absorptance a(λ,T). Since the TARC was essentially opaque from 5 to 15 μm, its thermal spectral emissivity in this range was computed as ε(λ,T)=a(λ,T)=1−r(λ,T). and sky-window thermal emissivity ε_w can be calculated by

$$\varepsilon_w(T) = \frac{\int_{8\mu m}^{13\mu m} B(\lambda,T)\varepsilon(\lambda,T)d\lambda}{\int_{8\mu m}^{13\mu m} B(\lambda,T)d\lambda} \tag{4-2}$$

Here B(λ) is the spectral radiance of a black body emission. The temperature-dependent infrared spectra and sky-window thermal emissivity of TARC is shown in Figure 4.5(b)

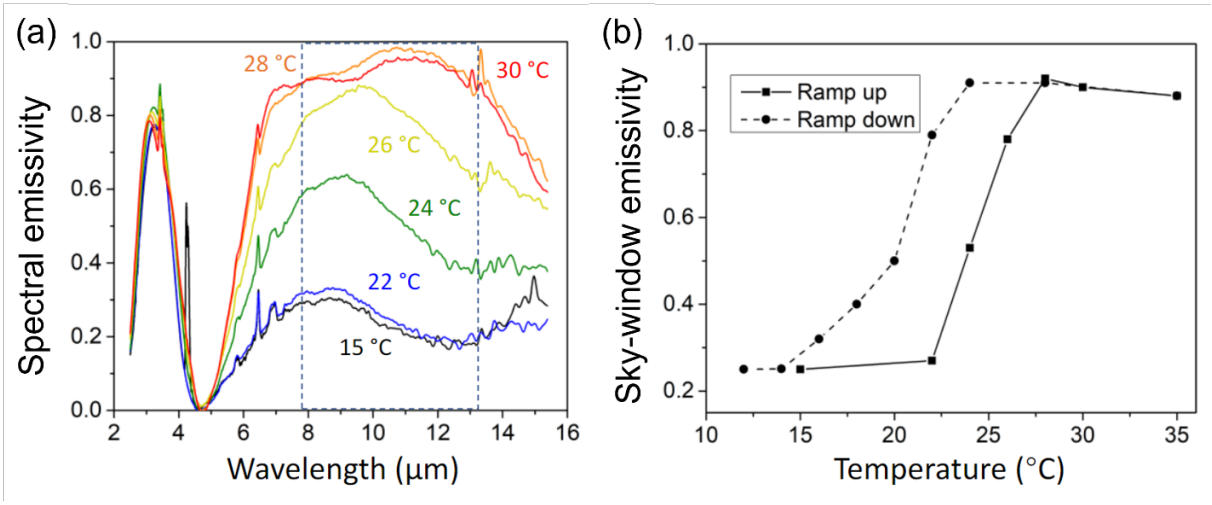


Figure 4.5. Detailed infrared spectra of TARC by Fourier transform infrared (FTIR) spectroscopy over the metal-insulator transition of $W_xV_{1-x}O_2$ (x=1.5%). (a) Spectral emissivity of TARC at temperatures ranging from 15 °C to 30 °C (ramp-up branch). The dashed box bounds the sky window (8-13 μm). (b) Sky-window emissivity as a function of TARC surface temperature, including both the ramp-up and ramp-down branches.

The spectral absorptance of TARC is also numerically calculated using COMSOL Multiphysics, with all the geometric parameters matching the original design. Material properties in IR and visible ranges are from Reference [108-111] and [112-114], respectively. Note that to better predict the actual TARC performance in the 5-15 μm range, the imaginary part of BaF_2 permittivity is slightly increased by $\Delta\varepsilon_i = 0.022\lambda - 0.049$ (unit of λ is μm) by fitting.

4.4.2. Cooling Power Measurement

The emissivity switching of the TARC enables deep modulation of radiative cooling power in response to ambient temperature, which we first measured in vacuum. The measurement setup is shown in Figure 4.6(a). We suspended a heater membrane by thin strings in a vacuum chamber, which was cooled with dry ice to ~ –78°C to minimize radiation from the chamber walls. We attached apiece of Al foil with $\varepsilon_{Al} \approx 0.03$ or a TARC of the same size to the top of the heater in two separate measurements. At each stabilized sample temperature T, the heating powers needed for the two coating scenarios are denoted as P_{Al} (T) and P_{TARC}(T), respectively. P_{Al}(T) and P_{TARC}(T) can be expressed from the thermal equilibrium equation:

$$P_{Al}(T) = \sigma \mathcal{A} \varepsilon_{Al}(T^4 - T_{env}^4) + C(T) \quad (4\text{-}3)$$

$$P_{TARC}(T) = \sigma \mathcal{A} \varepsilon_{TARC,v}(T^4 - T_{env}^4) + C(T) \quad (4\text{-}4)$$

Here σ is the Stefan-Boltzmann constant, $\mathcal{A}$ is the area of the sample surface, ε_{Al} and $\varepsilon_{TARC,v}$ are effective thermal emissivity of Al and TARC in vacuum conditions, T_{env} is the temperature of the environment (chamber wall), C(T) represents ancillary heat loss power from other radiative source and thermal conduction, and all temperatures are absolute. The ancillary loss is temperature dependent and unknown but is reasonably assumed to be the same for the surface conditions of the two materials. The inner walls of the vacuum chamber can be treated as a black body due to two reasons: (1) High-emissivity tape was used to cover the inner walls; (2) The sample area (16 cm^2) is much smaller than the total area of the inner walls (1,500 cm^2) [115]. Therefore, the cooling flux (power/area) contributed by the TARC, denoted as $P''_{cool}(T)$, can be calculated as:

$$P''_{cool}(T) = [P_{TARC}(T) - P_{Al}(T)]/\mathcal{A} = \sigma(\varepsilon_{TARC,v} - \varepsilon_{Al})(T^4 - T_{env}^4) \quad (4\text{-}5)$$

In this equation, σ is known, ε_{Al} is approximated as 0.03, and T_{env} is equal to the temperature of the cryogen (195 K, or -78 °C). Therefore, $\varepsilon_{TARC,v}$ at the I state and the M state can be obtained by fitting $P''_{cool}(T)$, with T at two branches before and after MIT.

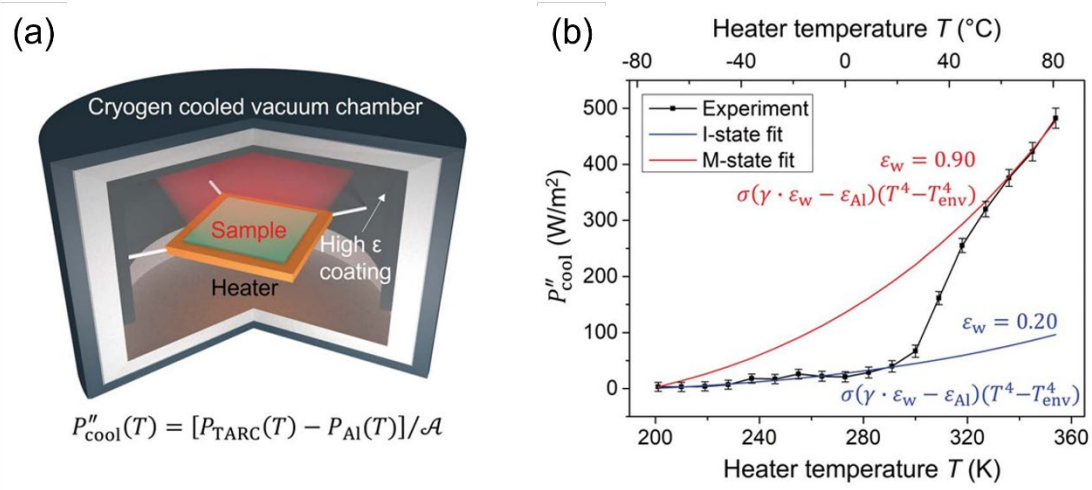


Figure 4.6. Characterization of intrinsic radiative cooling power of TARC in a cryogenic vacuum chamber. (a) Schematics of the experimental setup showing a thin heater membrane covered by either a TARC or an Al foil and suspended in a cryogen-cooled vacuum chamber. The Al foil reference is used to cancel the effect of thermal loss through conduction. (b) Calibrated experimental cooling flux (power/area) of TARC as a function of temperature in vacuum (the black data line). Fitting of $P''_{cool}(T)$ at I and M states by the Stefan-Boltzmann radiation law gives ε_w values of 0.20 and 0.90, respectively.

We plotted the calibrated cooling power (Figure 4.6(b)), which shows an abrupt increase in $P''_{cool}(T)$ when T rises above the MIT temperature. The error bars in Figure 4.6(b) come from the uncertainty of ε_{Al} (taken as 0.02) and a systematic error ϵ_s (taken as 8.0 W/m2) in the measurement of $P''_{cool}(T)$ arising from the limitation of the tool and the power instability. $P''_{cool}(T)$ measurements in the I-state and M state are well fitted by the Stefan-Boltzmann radiation law

$$P''_{cool}(T) = \sigma(\varepsilon_{TARC,v} - \varepsilon_{Al})(T^4 - T_{env}^4) \quad (4\text{-}6)$$

We have considered and corrected the effect of radiation from the chamber wall (~ –78°C) for the calibration. Furthermore, to account for the difference between the vacuum and ambient measurement conditions, we calculated the integral in Equation (4-2) in 8-13 μm and 2-30 μm for ε_w and $\varepsilon_{TARC,v}$, respectively. We found that the ratio between the two emissivity $\gamma = \frac{\varepsilon_{TARC,v}}{\varepsilon_w}$ is about 0.7 for both the I state and the M state. The values of ε_w were extracted to be ~0.20 and ~0.90, respectively, consistent with the spectrally characterized results (Figure 4.3(d)).

4.5. Outdoor Demonstration of Thermal Regulation Performance of TARC

We demonstrated the actual outdoor performance of the TARC (Figure 4.7). We recorded the surface temperatures (T_s) of the TARC, together with a dark roof coating product (BEHR #N520 Asphalt Gray) and a cool (white) roof coating product (GAF RoofShield White Acrylic), over 24 hours on a sunny summer day on an open-space rooftop in Berkeley, California, with temperature time series recorded by a customized automatic temperature reading system. The measurement system was carefully designed to minimize the effects of artifacts (Figure 4.7(a)).

From 00:00 to 09:00 local daylight time (LDT) when the ambient temperature was below T_{MIT}, the TARC was 2 °C warmer than the two reference roof coatings, arising from the low sky-window emissivity (ε_w = 0.20) of the TARC in the I-state and thus a lower radiative cooling power than the references (ε_w = 0.90). The 2 °C temperature elevation is consistent with adiabatic simulation results based on these nominal emissivity values and the local weather database (Details in subsection 4.6.1). From 09:00 to 13:00 LDT when the samples were in direct sunlight, T_s was dominated by the solar absorption in balance with radiative cooling and air convection, and the differences between the samples agree with the simulated results assuming the solar absorptance A to be 0.15, 0.25, and 0.70 for the white roof coating, TARC, and the dark roof coating, respectively. After 13:00 LDT, we erected a shield to intentionally block direct solar radiation to the surface of the samples (Figure 4.7(d)). This imitates the scenario of a cloud blocking the sun but with the rest of the sky mostly clear. We quickly observed a convergence of the T_s curves for all three samples, an indication that the thermal emissivity of the TARC in the M state is close to that of the two references (0.90). This condition persists for a few hours until T_s started to drop below T_{MIT} = 22 °C. After this point, TARC grew warmer than the two references, with a final temperature difference of about 2 °C similar to the 00:00 to 09:00 LDT period. This indicates that the TARC switched to the low-emissivity I state. The 24-hour outdoor experiments demonstrate the emissivity switching and resultant temperature regulation by TARC. Although the white roof coating shows an advantage over TARC in thermal management in summer daytime and under solar radiation (Figure 4.7(e)), for almost all the rest of the conditions, including daytime in other seasons and all the nighttime, the TARC regulates the roof temperature closer to the heating and cooling setpoints (22 and 24 °C) than the white roof coating (Figure 4.8). From an all-year-round perspective, the TARC demonstrates superiority compared to regular roof coatings in terms of source energy saving.

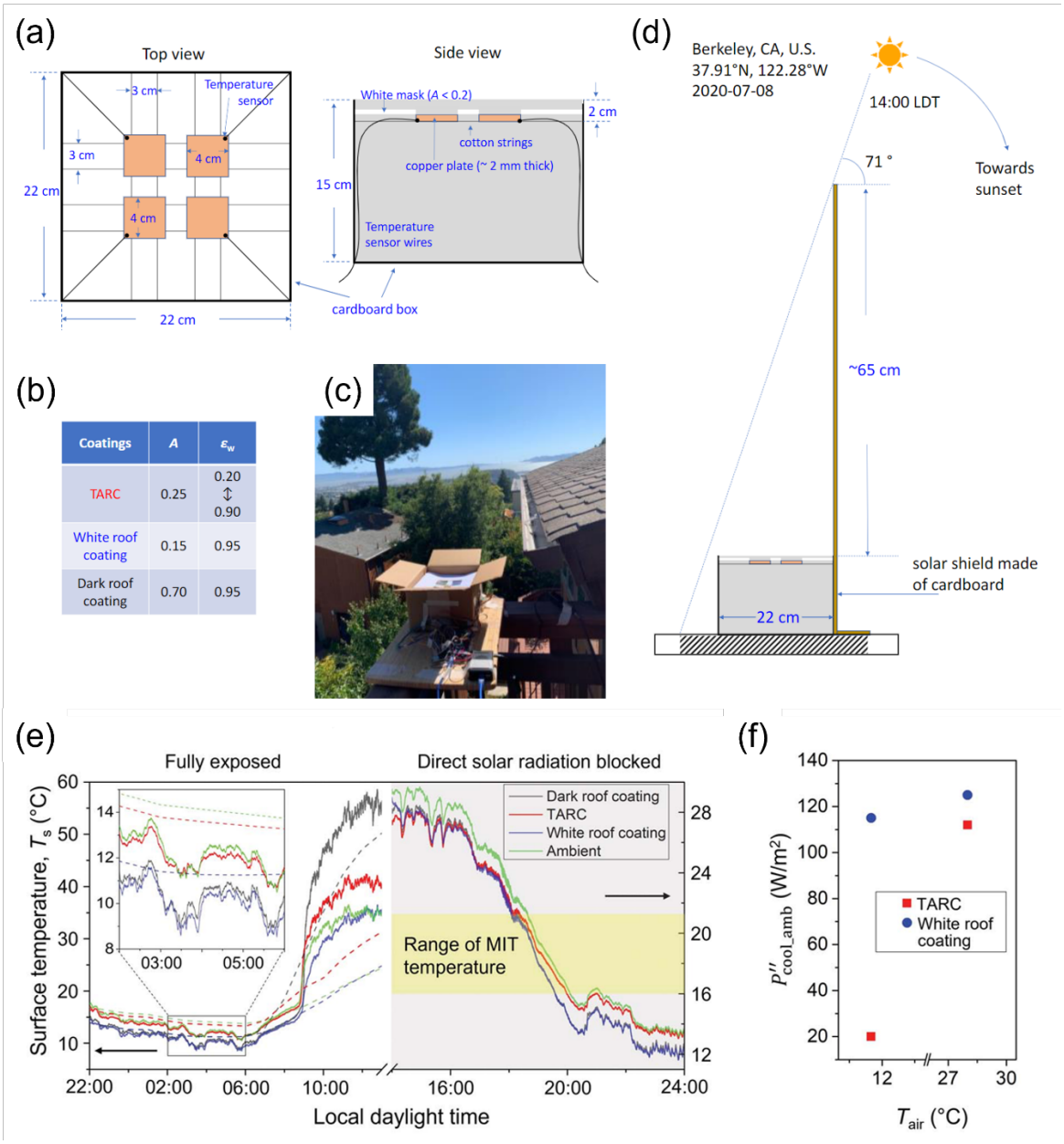


Figure 4.7. Characterization of TARC in an outdoor environment. (a) Schematic showing structure, geometry, and materials of the experimental setup. Identical 4 cm × 4 cm copper plates covered with different coatings were suspended by thin cotton strings (< 1 mm in diameter) in a cardboard box. A white paper mask was placed on top of the strings to minimize undesirable thermal artifacts from solar heating. (b) Solar absorption and sky-window IR emissivity of the measured material surfaces. (c) A photo of the actual experiment setup. (d) Schematic showing the solar shield used to block the direct solar radiation on the samples after 14:00 LDT. (e) Surface temperature of a TARC, a commercial dark roof coating (A = 0.70, ε_w = 0.90), and a commercial white roof coating (A = 0.15, ε_w = 0.90) in an open-space outdoor environment recorded over a day-night cycle. The solid and dashed curves are experimental data and simulation results based on a local weather database, respectively. Measurements starting from 14:00 local daylight time (LDT) were performed with the direct solar radiation blocked. Temperature observed after sunset show a clear sign of the TARC shutting off thermal radiative cooling as its surface ambient temperature falls below T_{MIT}. (f) Measured ambient cooling power of TARC and white roof coating with direct solar radiation blocked in the outdoor environment.

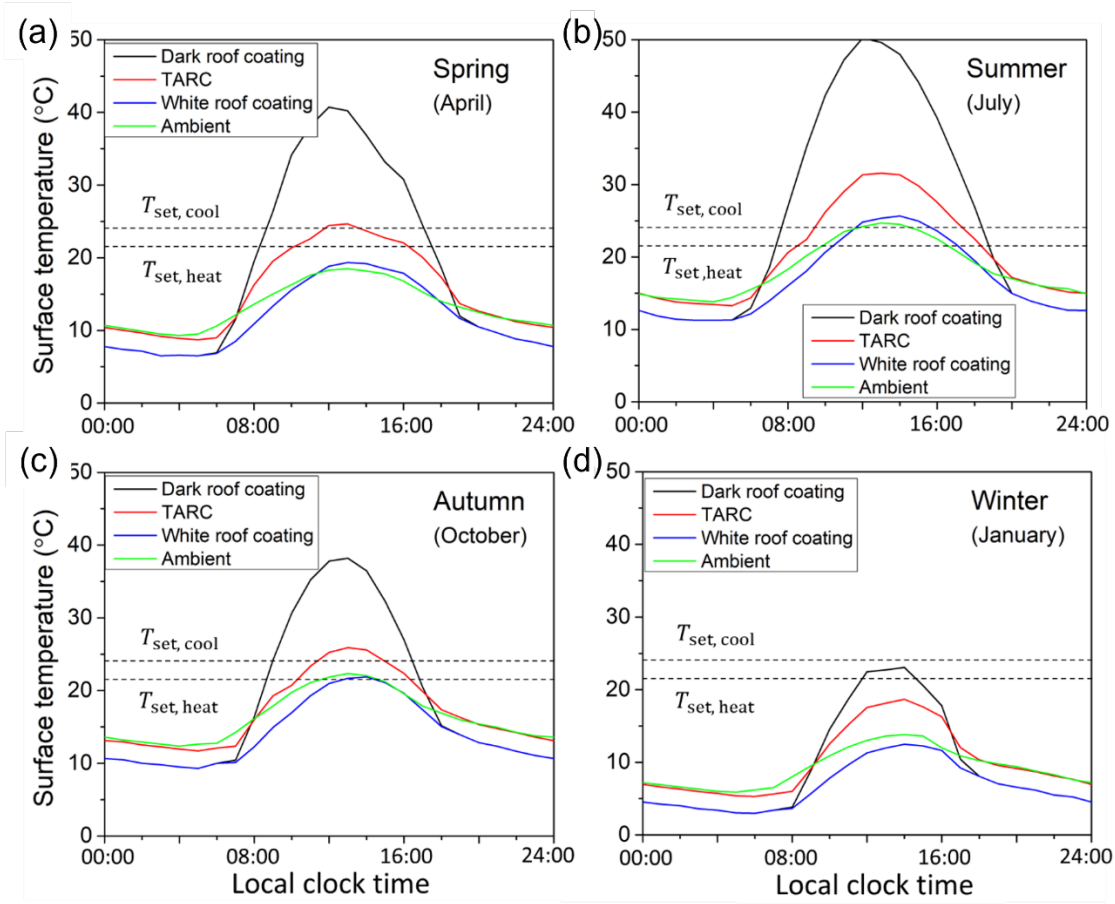


Figure 4.8. Simulation of the surface temperature of a dark roof coating, TARC, and a white roof coating (the same three samples as those in Figure 4.7 in four seasons in Berkeley, California (37.91°N, 122.28°W). The ambient temperature data (green curves) are directly exported from the climate database used for the simulation (Details in subsection 4.6.1). The only condition where the white roof coating has an advantage over the TARC in energy saving is the daytime in summer (b), while for almost all other conditions (all night times, daytime in spring, winter, and most of autumn), the surface of temperature of TARC is closer to the ideal temperature zone between heating and cooling temperature setpoints (22 °C and 24 °C) than other roof coatings. Therefore, TARC saves more energy than the white roof coating from an all-season, day-and-night perspective.

To directly compare their ambient condition cooling fluxes (P''_{cool_amb}), we heated the TARC and the white roof coating to the air temperature with the direct solar radiation blocked. P''_{cool_amb} refers to the net cooling flux from the surface, namely, the thermal radiative heat loss flux minus the absorbed diffuse solar irradiance. We plotted the P''_{cool_amb} values we obtained at a low and a high air temperature (Figure 4.7(f)). The TARC exhibits a clear switching of P''_{cool_amb} by a factor over five across the MIT. This behavior is in stark contrast to the nearly constant P''_{cool_amb} around 120 W/m^2 for the shaded white roof coating, which is consistent with values (90 - 130 W/m^2) reported in literature for roofs surfaced with daytime radiative cooling materials [79,83,84].

4.6. Energy Saving Potential of TARC by EnergyPlus simulation

We performed extensive numerical simulations to analyze the performance of TARC in household energy saving for the U.S. cities from an all-season perspective. We first calculated an hour-month map of T_s using a local weather file [116], laying the basis for estimation of energy saving. Then we assumed heating and cooling setpoints $T_{set,heat}$ = 22 °C and $T_{set,cool}$ = 24 °C [117], and approximated that the building will need heating when $T_s < T_{set,heat}$ and require cooling when $T_s > T_{set,cool}$. We used past simulations of cool-roof energy savings to predict potential space-conditioning source energy savings (SCSES) per unit roof area attainable by using TARC in place of roofing materials that have static values of solar absorptance and thermal emissivity. The figure of merit of TARC is represented by $SCSES_{min}$, the minimum value of SCSES found over all existing conventional roofing materials, which have constant values of A_{ref} and ε_{ref}.

We mapped $SCSES_{min}$ for cities representing the 15 U.S. climate zones. This figure-of-merit map shows that TARC provides clear, positive annual space-conditioning source energy savings relative to existing roof coating materials in most major cities, except for climates that are constantly cold (such as Fairbanks) or hot (such as Miami) throughout the year. It highlights the advantage of TARC, especially in climate zones with wide temperature variations, day to night or summer to winter.

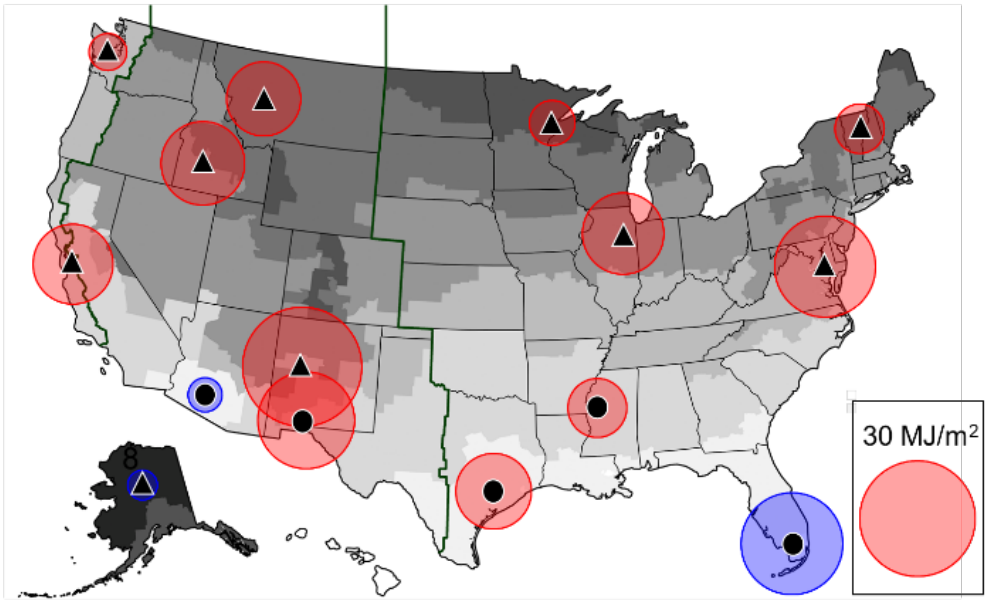


Figure 4.9. Simulated minimum annual space conditioning source energy saving per unit roof area ($SCSES_{min}$) of TARC compared to other existing roof coating materials for different cities representing the 15 climate zones in the U.S. Red and blue circles indicate positive and negative $SCSES_{min}$ values, respectively. The values are scaled to the area of the circles. Representation of the triangle and circle icons is explained in the Method section (subsection 4.6.1).

4.6.1. Surface Temperature Simulation

The stabilized surface temperature of TARC and any materials with given solar absorptance (A) and sky-window thermal emissivity (ε_w) can be calculated based on the adiabatic approximation [118], assuming negligible heat exchange with the underlying structure.

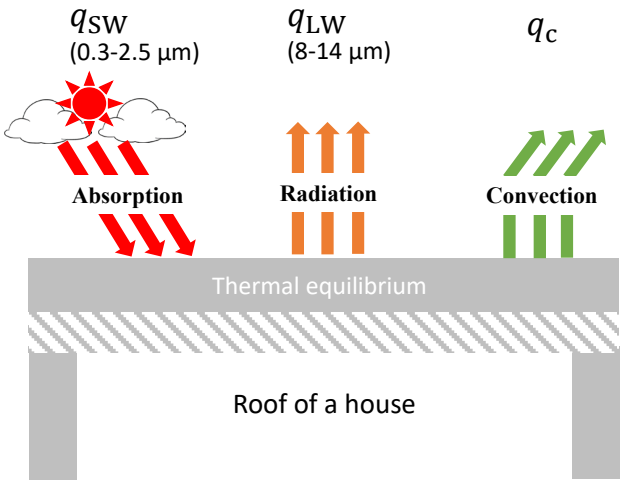


Figure 4.10. Schematic of the adiabatic approximation for surface temperature calculation. For a surface with given solar absorptance (A) and sky-window thermal emissivity (ε_w), this model enables the calculation of the surface temperature T_s in any climate.

The thermal equilibrium is balanced by the three heat exchange components on the surface, which are net long-wave thermal radiative loss (q_{LW}), short-wave solar absorption (q_{SW}), and convective heat loss (q_c), respectively. The equation for thermal equilibrium is denoted as

$$q_{SW} - q_{LW} - q_c = 0 \tag{4-7}$$

Each term can be expanded as

$$q_{SW} = A \cdot I \tag{4-8}$$

$$q_{LW} = \varepsilon_w(T_s) \cdot \sigma(T_s^4 - T_{atm}^4) \tag{4-9}$$

$$q_c = h_c(T_s - T_a) \tag{4-10}$$

In these equations, I is the solar irradiance, T_s is the absolute surface temperature, T_{sky} is the absolute sky temperature, h_c is the convective heat transfer coefficient, and T_a is the absolute air temperature. The model schematic is shown in Figure 4.10. We note that though Equation (4-9) is typically applied to broad-band IR emitters with uniform spectral emissivity from 2 μm to 30 μm, it can be safely extended to the case of TARC. To support this argument, we calculated the net radiative cooling power for TARC and that of a broad-band emitter with constant emissivity equal to ε_w of TARC. The general form of net radiative cooling power P_{net} is:

$$P_{net} = P_{rad} - P_{atm} \tag{4-11}$$

$$P_{rad} = \iint B(\lambda, T_s)\varepsilon_s(\lambda, \Omega, T_s)cos\theta d\Omega d\lambda \quad (4\text{-}12)$$

$$P_{atm} = \iint B(\lambda, T_a)\varepsilon_{atm}(\lambda, \Omega)\varepsilon_s(\lambda, \Omega, T_s)cos\theta d\Omega d\lambda \quad (4\text{-}13)$$

in which P_{rad} and P_{atm} are radiative power of the surface and absorbed radiation power from the atmosphere, respectively; B is the black body spectral radiance; ε_s is the surface's spectral emissivity; and ε_{atm} is the atmospheric spectral emissivity. For simplicity, we assume that TARC is in M state when $T_s \geq 27$ °C, and in I state when $T_s \leq 19$ °C. The ε_{atm} is retrieved from previous studies [119]. The spectral integration range is 2-30 μm. The results are presented in Figure 4.11, showing that the net radiative cooling power of TARC and the broad-band emitter are very similar for different scenarios, with deviation <10% even for extreme conditions ($T_s - T_a > 20$ °C). Therefore, the approximation of TARC as a broad-band emitter in the calculation of long-wave radiative power (q_{LW}) is valid.

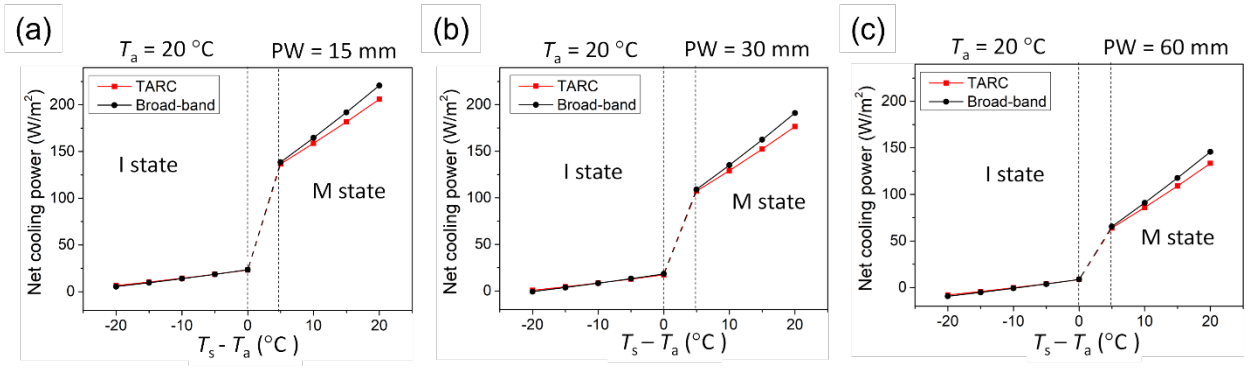


Figure 4.11. Calculated net radiative cooling power of TARC and a broad-band emitter with a constant emissivity equal to ε_w of TARC. The results include conditions with various surface temperatures and precipitable water (PW). The atmospheric spectral emissivity for different PW are obtained from [119].

The solar irradiance (I) and the air temperature (T_a) can be directly imported from the TMY3 weather files included in the EnergyPlus climate database [116]. For an infinitely large surface, the convective heat transfer coefficient (h_c, W/m^2·K) is related to the wind speed (v, m/s) by [120]

$$h_c = 5.6 + 5.1 \times \sqrt{v} \quad (4\text{-}14)$$

The sky temperature is approximated by

$$T_{sky}^4 = \varepsilon_{sky} \cdot T_a^4 \quad (4\text{-}15)$$

$$\varepsilon_{sky} = \varepsilon_{clear_sky} + 0.8(1 - \varepsilon_{clear_sky}) \cdot CF \quad (4\text{-}16)$$

$$\varepsilon_{clear_sky} = 0.754 + 0.0044T_d \quad (4\text{-}17)$$

following a clear-sky model [121] combined with cloud correction [122], and the sky emissivity is denoted as ε_{clear_sky} and ε_{sky} in each model, respectively. T_d is the dew point temperature (in °C) and CF is the cloud factor (ranging from 0 to 1; 0 for no clouds and 1 for full coverage), each of which is available in the climate database. The solar absorptance A and the thermal emissivity ε

are property parameters for the materials either pre-set (for reference materials) or obtained from experimental characterization (for TARC). Note that for TARC, $\varepsilon_w(T_s)$ is set to 0.20 for $T_s <$ 19 °C and to 0.90 for $T_s >$ 27 °C and approximated by a linear interpolation in the transition region (19 °C $\leq T_s \leq$ 27 °C). The only unknown parameter T_s can thus be calculated by solving the equations (4-7) to (4-10). Based on this setup, the all-year-around temperature map of TARC and of all conventional materials with an arbitrary combination of static A and ε were calculated and compared.

4.6.2. Energy Saving Comparison Between TARC and Conventional Materials

In hour-of-year i, we define heating degrees $D_{h,i} = \left(T_{set,heat} - T_{s,i}\right)_+$ and cooling degrees $D_{c,i} = \left(T_{s,i} - T_{set,cool}\right)_+$, where $x_+ = x$ if $x > 0$ or 0 otherwise. The annually averaged heating degrees and cooling degrees are denoted by D_h and D_c, respectively.

To evaluate the potential space-conditioning source energy savings (SCSES) per unit roof area obtained by using TARC instead of a reference roofing surface with static solar absorptance A_{ref} and static thermal emissivity ε_{ref}, we calculated, in each city, $\Delta D_{h,TARC}(A_{ref}, \varepsilon_{ref}) \equiv D_{h,TARC} - D_h(A_{ref}, \varepsilon_{ref})$ and $\Delta D_{c,TARC}(A_{ref}, \varepsilon_{ref}) \equiv D_{c,TARC} - D_c(A_{ref}, \varepsilon_{ref})$, varying A_{ref} and ε_{ref} from 0 to 1. We then computed space-conditioning source energy savings $\Delta S_{TARC}(A_{ref}, \varepsilon_{ref}) = \alpha_h \Delta D_{h,TARC}(A_{ref}, \varepsilon_{ref}) + \alpha_c \Delta D_{c,TARC}(A_{ref}, \varepsilon_{ref})$ for each building category and vintage of interest. Here the α_h and α_c are calculated by regressing our own calculations of the reductions in annual average heating degrees ΔD_h and cooling degrees ΔD_c against the U.S. cool-roof space heating energy savings ΔS_h and space cooling energy savings ΔS_c reported by Rosado & Levinson, respectively [117]. These linear fits of the form $\Delta S_h = \alpha_h \Delta D_h$ and $\Delta S_c = \alpha_c \Delta D_c$ yield. Specifically, energy simulations for four static roofing materials with ε_w = 0.90 and solar reflectance R = 0.10, 0.25, 0.40, or 0.60 ($A = 1 - R = 0.90, 0.75, 0.60,$ or 0.40) were selected for the extraction of the coefficients α_h and α_c using the material with A = 0.90 as the baseline. Note that ΔS_h and ΔS_c are not directly presented by Rosado & Levinson but can be estimated from the heating, cooling, and fan energy uses reported in that work, as described in Appendix A1.

The minimum $\Delta S_{TARC}(A_{ref}, \varepsilon_{ref})$ (namely, $SCSES_{min}$) for all possible existing roof coating properties is taken as the figure of merit for each combination of local climate, building category, and vintage group. In Figure 4.9, we used three different icons to represent three different types of competing materials where $SCSES_{min}$ occurs -- that is, the strongest rivals to TARC in energy saving. The triangle, circle, and square icons represent metallic, white, and dark roof coatings, with typical $(A_{ref}, \varepsilon_{ref})$ parameters around (0.35, 0.25), (0.05, 0.95), and (0.95, 0.95), respectively.

The results in Figure 4.9 are based on the dominant resident building prototype in the U.S. [123], which is a single-family home built prior to 1980. Minimum annual source energy savings per unit roof area for single-family homes and apartment buildings built before 1980, between 1980 and 1999, and recently are presented in Table A.1.

4.6.3. Example: Energy Saving Performance of TARC in Baltimore, MD

An example of SCSES mapped with A_{ref} and ε_{ref} (each ranging from 0 to 1) for Baltimore is plotted in Figure 4.12. The dashed boxes in the right panel of Figure 4.12 correspond to the parameters of

currently available roof coatings. The minimum point within the dashed box regions denotes the material that leads to the minimum space conditioning source energy saving ($SCSES_{min}$) compared to all other roof coatings. In other words, the most energy-saving material (with fixed A_{ref} and ε_{ref}) is first selected from all existing roof materials, and then compared with TARC. Thus, $SCSES_{min}$ is the additional source energy saving of TARC compared to that "existing best energy-saving material". $SCSES_{min}$ is taken as the figure of merit of TARC for the local climate and used to plot the mapping in Figure 4.9. In this example, the value for Baltimore is 22.4 MJ/(m^2·y), suggesting that would yield at least an annual source energy saving of 2.64 GJ over any other existing roof coating materials for a typical single-family building with a roof area of 118 m².

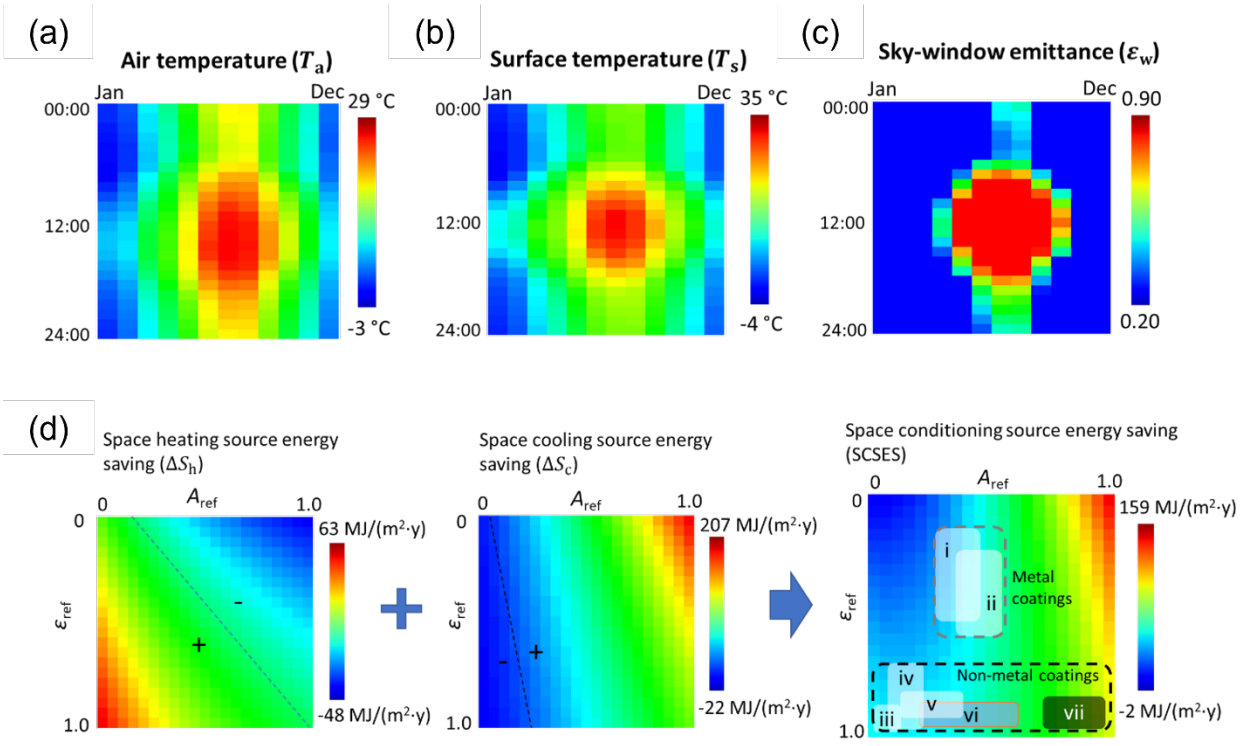


Figure 4.12. Example of surface temperature calculation based on the model for Baltimore, MD. (a) Air temperature from the TMY3 weather files included in the EnergyPlus climate database. (b)-(c) Projected surface temperature and sky-window emissivity of TARC. (d) Calculated energy saving advantage of TARC compared to conventional materials. All savings are normalized to roof area. The indexes in the SCSES map represent: i, white metal plate; ii, aluminum pigments; iii, daytime radiative coolers; iv, silicone; v, acrylic; vi, polyurethane; and vii, asphalt.

4.7. Conclusion and Remarks

We developed a mechanically flexible, energy-free, and temperature-adaptive radiative coating (TARC) for intelligent regulation of household temperature. Our system features a thermally driven metal-insulator transition in cooperation with photonic resonance, and demonstrates self-switching in sky-window thermal emissivity from 0.20 to 0.90 at a desired temperature of about 22 °C. These attractive properties enable switching of the system from the radiative cooling mode at high temperatures to the solar-heating or keep-warm mode at low temperatures in an outdoor

setting. For most cities in the U.S., our simulations indicate the TARC may outperform all conventional roof materials in terms of cutting energy consumption for households.

5. Scalable Temperature Adaptive Radiative Coating (STARC) with Optimized Solar Absorption

5.1. Challenges for the Applications of Thermal Radiation Modulation Materials

As introduced in chapter 4, using thermal radiation modulation material is an emerging solution to solve the overcooling problem of conventional cool roofs. According to simulation, a temperature-adaptive radiative coating that has a static solar absorptance (0.25) and a switchable thermal emissivity (0.2 to 0.9) with a switching temperature of ~22ºC has the potential to save 10% of electric consumption in an average U.S. house [13]. Although several thermal radiation modulation materials have been reported, their applications are severely limited in many aspects, such as extra energy input [91-94], requirements of user activation or mechanically moving parts [124] and size limitations due to non-scalable fabrication methods [13,14]. Moreover, these materials have a very high cost since expensive materials or nanofabrication techniques are used.

In this chapter, we report our solution to all these pressing problems, which is termed as scalable temperature-adaptive radiative coating (STARC) with optimized solar absorption. The STARC is a flexible film that can be mass produced with roll-to-roll system while maintaining the same emissivity switching ability as the TARC in chapter 4. The STARC has a novel structure in which $W_xV_{1-x}O_2$ in encapsulated in polyethylene matrix. Since $W_xV_{1-x}O_2$ is protected from water and air as-fabricated, the lifetime as a roof material can be drastically improved. Moreover, the color (and solar absorption) of STARC can be adjusted in a wide range by incorporating IR transparent pigments. Thus, the aesthetic needs and energy saving optimization can be fulfilled.

5.2. Design of STARC and Manufacturing Process

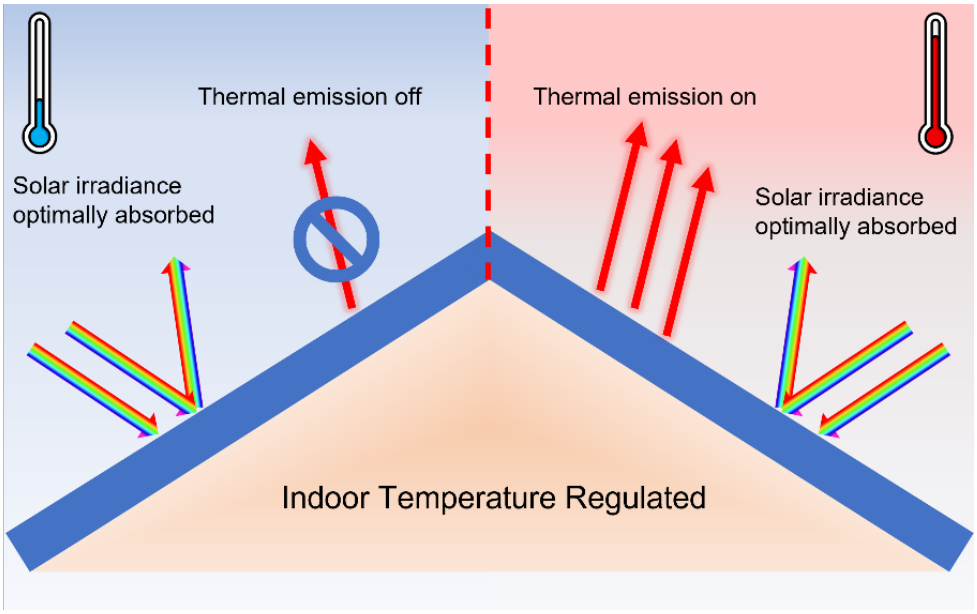


Figure 5.1. The working principle of STARC as a roof coating, where solar absorptance is temperature-independent but optimized to local climate, and thermal emissivity switches automatically with ambient temperature.

5.2.1. Structure Design of STARC

The working principle of STARC is similar to that of TARC in chapter 4 (Figure 5.1). And the thermal radiation modulation is also based on the metal-insulator transition of tungsten-doped vanadium dioxide ($W_xV_{1-x}O_2$). For general household applications, x can be set as 2% so the corresponding phase transition temperature (T_{MIT}) is around 22 °C. In the cases that roof temperature is low, such as during the night or winter, the sly-window emissivity ε_w of STARC is only ~0.25, so the heat loss from thermal radiation is strongly suppressed. In other cases, such as directly under sunlight, the roof temperature can be as high as 60~70 ℃, and STARC has a strong thermal emission with ε_w at 0.85 (Figure 5.2(d)). Since STARC has the emissivity modulation ability and magnitude similar to that of TARC, all the energy-saving simulation results in section 4.6 also applies to STARC.

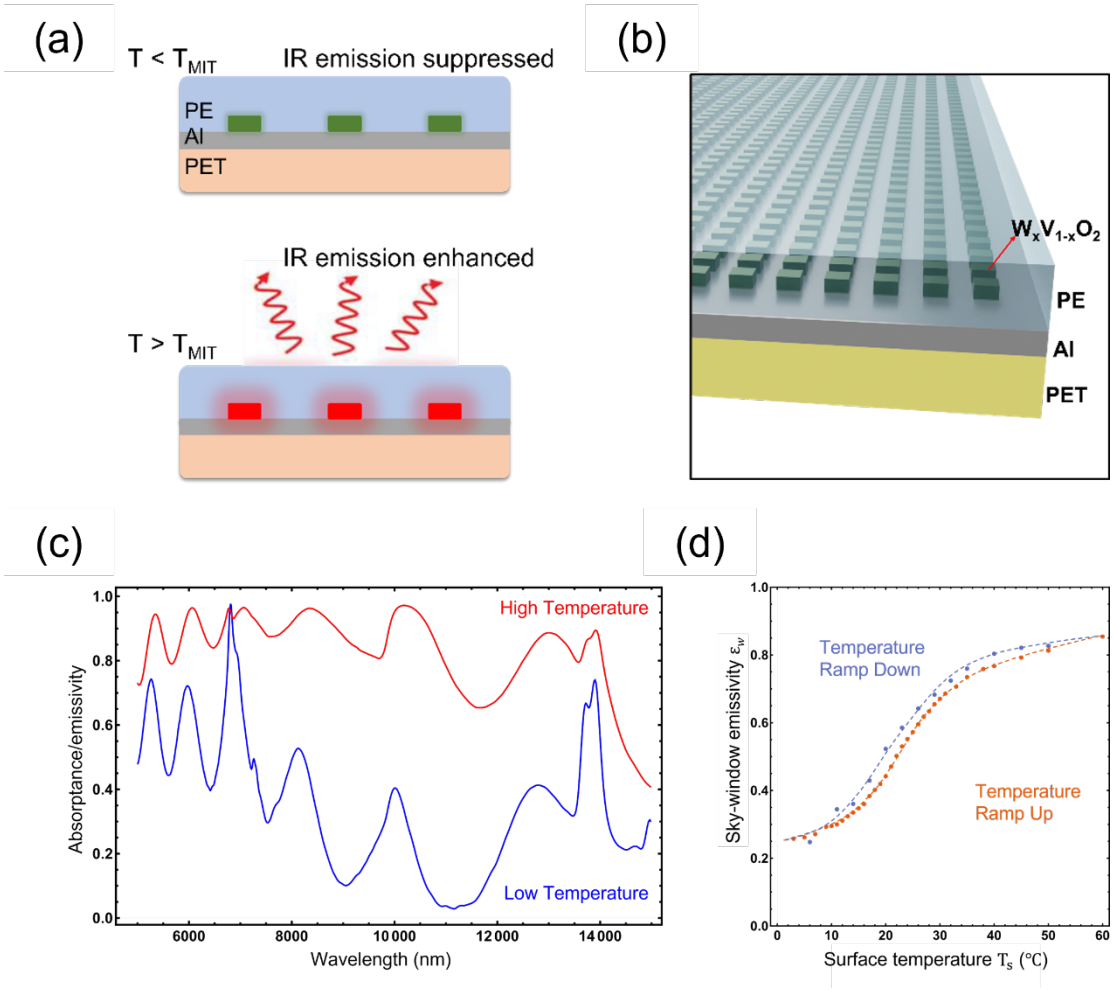


Figure 5.2. (a) Structure, composition and mechanism of STARC. (b) A 3D view shows the structure of STARC. (c) Absorptance/emissivity spectra calculated from FTIR spectroscopy result of STARC at low and high temperatures. (d) sky-window emissivity ε_w calculated from temperature-dependent FTIR measurements. The dashed lines are guides to the eye.

Compared to TARC, STARC has a slightly but critically different structure, which is aimed at mass production. The structure is shown in Figure 5.2(a)-(b). The STARC includes a substrate (PET), a metal layer deposited on the substrate (Al), an array of tungsten-doped vanadium dioxide ($W_xV_{1-x}O_2$) blocks, and a mid-infrared transparent dielectric layer (PE, food wrap in the experiments). The array of $W_xV_{1-x}O_2$ blocks is formed by clusters of VO_2 micro-particles, and directly touches the Al surface. Since the array of blocks is encapsulated by the PE matrix, it is free from the degradation caused by the oxidization of $W_xV_{1-x}O_2$. Note that since the substrate and the dielectric layer of STARC is polymer, it has better flexibility and is free of cracks when bent.

Another major advantage of the new STARC structure is that the emissivity is insensitive to the thickness of the dielectric layer. This insensitivity greatly improves the error tolerance in fabrication process.

In the case of TARC, the broad band absorption/emission in IR atmospheric window strongly relies on the complementary peaks from meta-structure and Fabry-Perot resonance, hence it is very sensitive to the thickness of the structure. Any minor change in the thickness would only cause the shift of the Fabry-Perot peak, leaving the meta-structure peaks unaffected. As a result, the absorption spectrum in M state will largely deviate from the ideal case in Figure 4.3(d).

However, changing the thickness of the dielectric layer cannot affect the average trend of the $\varepsilon(\lambda)$ for STARC. At a random temperature (35℃), emissivity spectra were measured for two STARCs with PE thickness of 12um and 24um, respectively. As shown in Figure 5.3, the two emissivity spectra have almost the same magnitude, thus the sky-window emissivity for these two STARCs should be close to each other. This insensitivity of dielectric layer thickness has been verified in a wide temperature range that covers the phase transition of $W_xV_{1-x}O_2$.

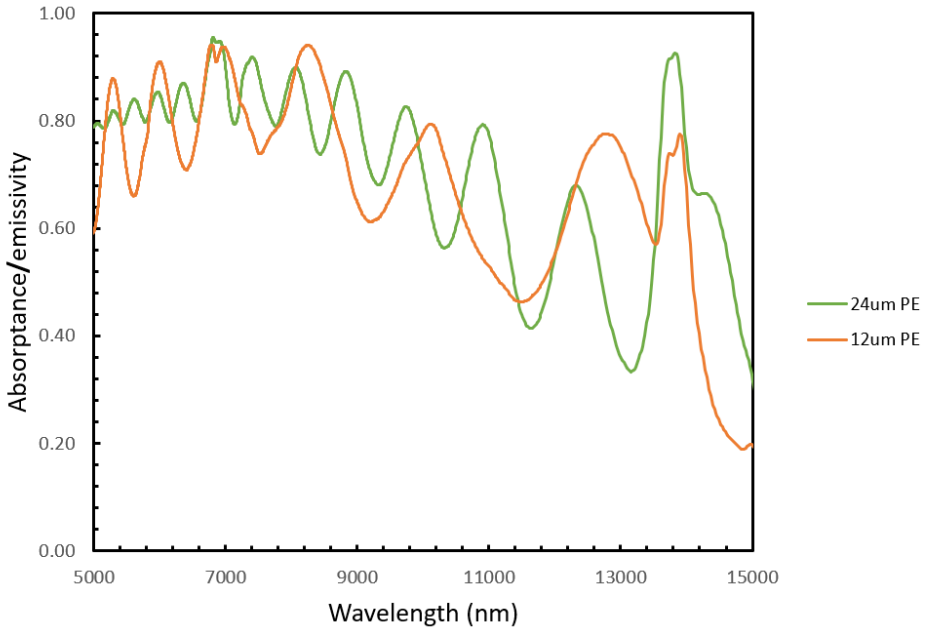


Figure 5.3. Absorptance/emissivity spectra calculated from FTIR spectroscopy result of STARC with PE thickness of 12um and 24um, respectively. The two curves in the plot are measured at the same temperature (35℃) that is

randomly selected. The thickness-insensitivity has been checked for multiple different temperatures across the phase transition of $W_xV_{1-x}O_2$.

5.2.2. Design of the Production Line for STARC

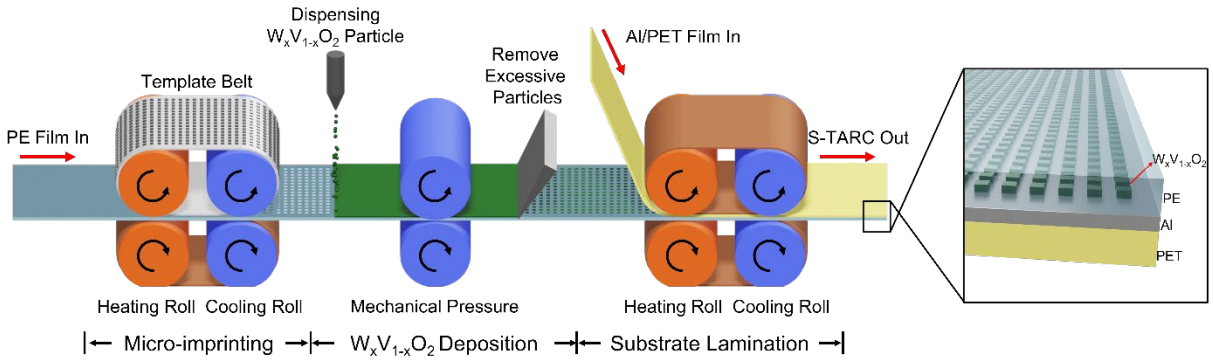


Figure 5.4. Schematic illustration of the production line for STARC.

To fabricate the STARC, a PE film is first thermal imprinted by a metal template through a heated roller system. The reusable metal template is a metal sheet with a periodic planar array of micron-sized pillars on the surface. An array of holes with the same dimension will be imprinted on the surface of PE film (Saran Premium Plastic Wrap). Then $W_xV_{1-x}O_2$ micro-particles (diameter <2μm) are spread onto the patterned PE film surface by spraying a $W_xV_{1-x}O_2$ particles/isopropyl alcohol suspension. Mechanical pressure can be applied to the $W_xV_{1-x}O_2$ particles to improve the filling of holes. After wiping off the excessive $W_xV_{1-x}O_2$ particles, a PE film embedded with a planar array of $W_xV_{1-x}O_2$ blocks is produced. The STARC is formed by laminating the patterned side of the PE film to a metallized polyester substrate (McMaster-Carr) by running through another heated roller system. The schematic of the process is shown in Figure 5.4. The flow chart of the fabrication process of STAC can be found in Appendix A.4.

5.2.3. Fabrication of the Reusable Imprinting Template

The process to produce the metal template for the micro-imprinting is as follows (Appendix A.5): A patterned Si substrate is fabricated by lithography (GCA8500 Wafer Stepper) and etching (Lam Research Poly-Si TCP Etcher). After a conductive layer is sputtered (Edwards Auto 306 Sputter Coater) on the patterned Si surface, a metal layer (Ni) with approximately 20 um thickness can be deposited by electroplating. Then the Si substrate is removed by KOH etching, and the remaining metal is the desired template for imprinting on PE films. An optional layer of polyimide can be attached to the Ni template to improve the mechanical strength without losing the flexibility.

Although the metal template is fabricated with multiple nanofabrication techniques, the STARC is still considered scalable since the template is reusable due to the excellent mechanical properties and chemical resistance of Ni. During the one-year period of experiments, no damage to the Ni templates is observed.

5.3. Colored Variations of STARC for Optimal Solar Absorption

The STARC also features an adjustable solar absorptance, which is an additional crucial factor affecting the annual energy saving by the temperature-adaptive radiative materials. For example, in cities with colder temperatures throughout the year, a higher solar absorption of the roof or wall can increase the energy intake from sunlight and save more energy from space heating. While in cities with tropical climates, low solar absorption is desired since the major energy consumption in buildings is for air conditioning.

We used the method in section 4.6 to calculate the energy saving of TARC and STARC ($SCSES_{TARC}$) as a function of the solar absorptance for major U.S. cities. The ε_w of TARC has been set to be 0.2 in I state and 0.9 in M state. Each $SCSES_{TARC}$ curve is U shaped, suggesting that a solar absorptance neither too low nor too high is desirable. The ideal solar absorptance varies depending on the cities and tends to shift to a higher value for those with colder climates, consistent with expectations.

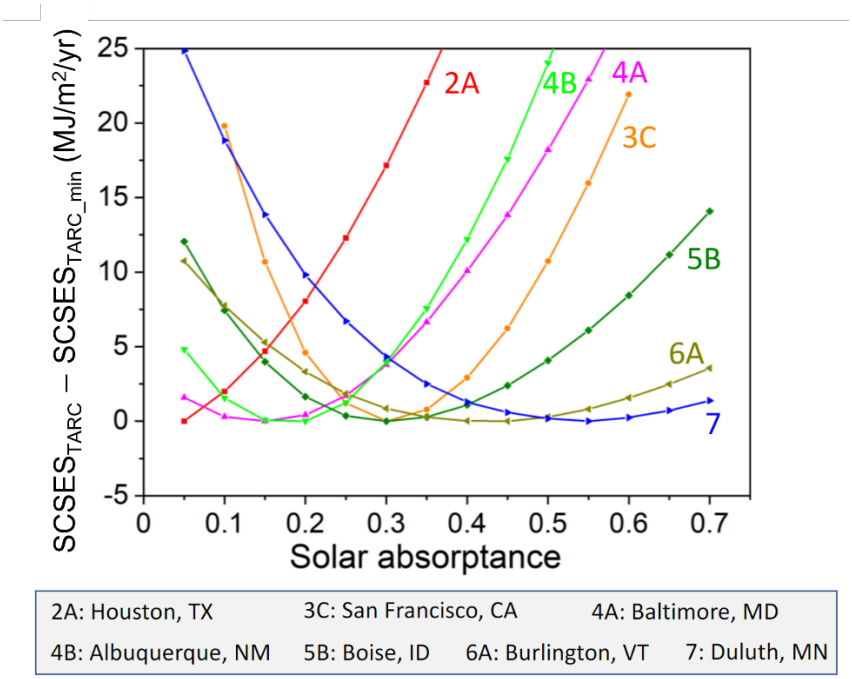


Figure 5.5. Calculation of space-conditioning source energy consumption of TARC ($SCSES_{TARC}$) in different cities as a function of the TARC solar absorptance (A). The indexes (2A, 3C, etc.) represent the different U.S. climate zones. In each curve, $SCSES_{TARC}$ is vertically offset by its minimum value for better display of the data in the plot.

In our STARC, we can customize the color of STARC and optimize its solar absorptance by adding an extra layer of infrared-transparent pigments sealed with a dielectric layer (Figure 5.6(a)). Additional steps are added to the fabrication process of STARC (Appendix A.4): pigments that are transparent in the sky window wavelength range are sprayed onto the STARC surface. Then the pigments are sealed by laminating a smooth PE film on the top. We have used Prussian Blue (Blue), BaF_2 (White), ZnSe (Yellow), and Fe_2O_3 (red) as the pigments.

Figure 5.6(b) shows the spectral solar absorption modulation ability of colored STARC. With a combination of different species and different coverage of pigments to use, we can achieve a wide modulation range of solar absorption to fit the different local climates.

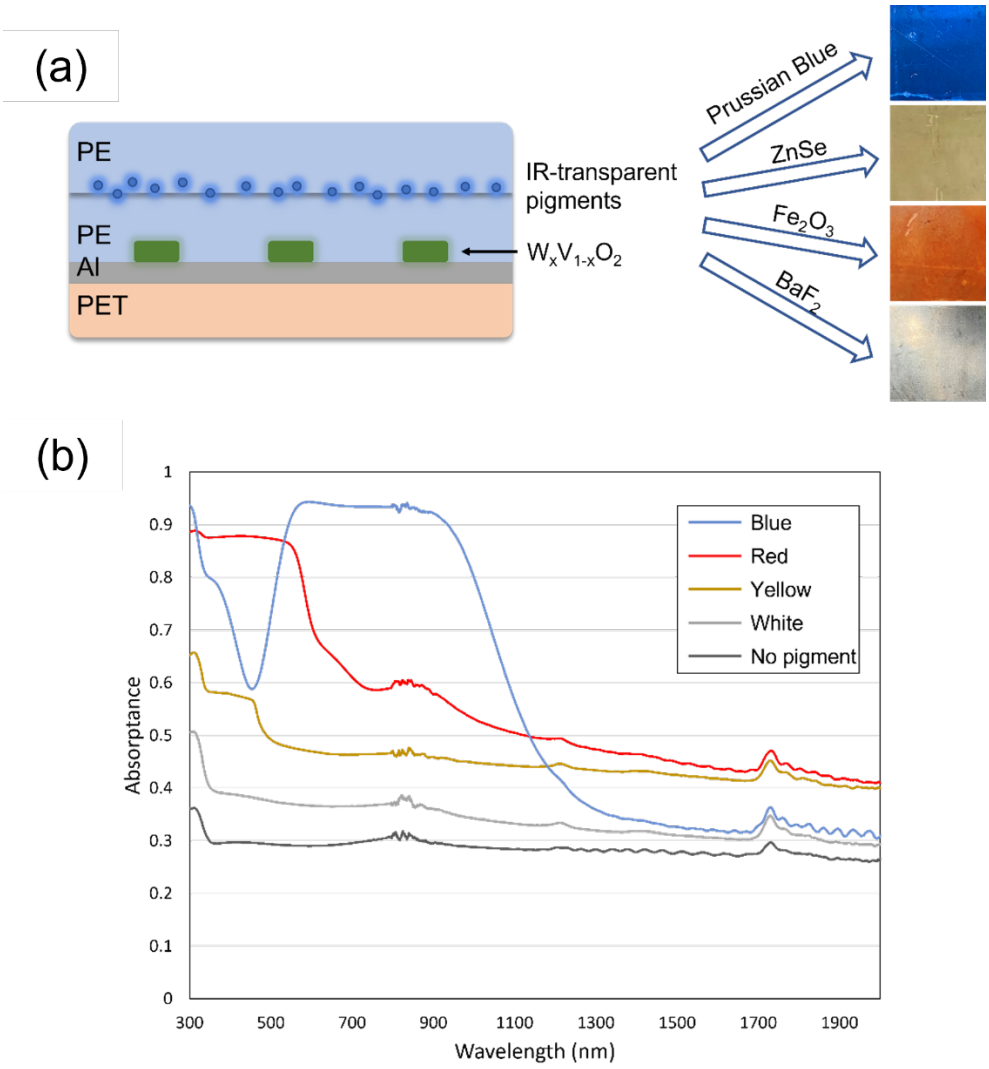


Figure 5.6. (a) Structure of the colored STARC. The chemicals next to the arrows are the pigments used to fabricate the colored STARCs in the corresponding photos on the right-hand side. (b) The spectral absorptance of STARCs in the solar wavelength range, calculated from the integrating sphere (diffuse + specular) measurements.

5.4. Field Test with a Mock-Up of Residential House

5.4.1. Experimental Setup

An outdoor temperature regulation experiment was conducted to demonstrate the performance of STARC as a smart roof coating. The STARC, a dark roof coating product (BEHR #N520 Asphalt Gray), and a cool roof coating product (Henry Enviro-White Extreme Elastomeric Roof Coating) were used as roofs on three model houses that serve as mock-ups of residential houses. The model houses were 3D-printed with ABS filament and were painted with white (walls) and dark

(windows and doors) commercial paints. To simulate the heat exchange of real houses, the thermal conductance per area of the model house was carefully tuned to be close to that of real houses by adjusting the wall and roof thickness of the model houses. During the measurement, the model houses are placed on a foam board to exclude the non-uniformity of the ground.

The indoor and roof temperatures of the model houses were measured by temperature sensors inside of each model house, and the temperature-time series were recorded by a Raspberry Pi. The experiment was performed on a cloudless summer day on a residential house roof in Berkeley, CA (Figure 5.7), and the weather data were retrieved from a weather station near the experiment site.



Figure 5.7. The outdoor experiment setup for household thermal regulation demonstration

5.4.2. Result of the Field Test

The middle panel of Figure 5.8 shows a 24-hour record of the indoor temperature of houses coated with STARC (without colored pigments), dark coating, and white cool roof coating, respectively. The left and right panels are magnified plots of temperature at night and noon, respectively. The temperature-time series show that during the night, STARC can keep the house ~2℃ high than the other two roof materials, which indicates that STARC switches to a low emissivity, heat-retaining state. While at noon with direct sunlight, STARC performs as a cool roof with a solar absorptance slightly higher (~2℃) than that of the commercial white coating.

Since the heating degree difference between STARC and the commercial white coating are similar, and space heaters are generally less efficient than air conditioners, the daytime energy saving advantage of the white coating can be compensated by the better night-time performance of STARC on a summer day. Considering that the STARC would perform better in other seasons, we can conclude that the STARC outperforms the cool roof coating in terms of year-round energy saving due to its non-stop, all-season thermal regulation.

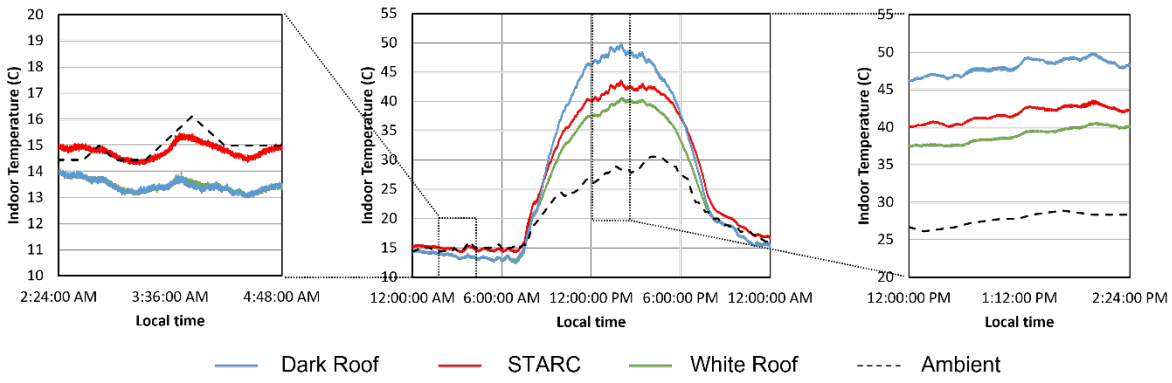


Figure 5.8. The 24-hour record of the indoor temperature of model houses with different roof materials (STARC and two reference commercial paints). The left and right panels show magnified plots of temperature at night and noon, respectively.

5.5. Conclusion and Remarks

We demonstrated a scalable temperature-adaptive radiative coating (STARC) to solve the most pressing problems with the existing smart cool roof materials. The STARC can be mass produced with roll-to-roll system while maintaining the same emissivity switching ability as the TARC in chapter 4. The cost of materials and electricity to fabricate the STRAC in the lab is estimated at $0.8/sqft, which is already comparable to some high-performance cool roofs on the market.

The STARC features a novel structure that is tolerant to the thickness change and has longer lifetime than TARC. The temperature regulation performance of STARC is also tested by the 24-hour indoor-temperature measurement with mock-up residential houses. Moreover, the solar absorption of STARC can be adjusted by incorporating IR-transparent pigments, making it an ideal system for maximizing the energy saving as a roof and fulfilling the aesthetic needs from house owners.

Additionally, STARC can also find temperature-regulation applications in other systems that have surfaces facing the sky, such as tents, vehicles, clothes, space objects and mobile electronics.

6. Summary and Outlook

In this dissertation, we exhibited the VO_2-based thermal radiation modulation structure for various applications and their advantages over conventional materials. In chapter 1, we reviewed the physics and applications of thermal radiation. Structural, optical and doping properties of VO_2 and W-doped VO_2 were revisited. In chapter 2, we showed a nearly T^{-4} dependence thermal emissivity by modulating the thermal emissivity of a graded W-doped VO_2 ($W_xV_{1-x}O_2$) structure. An IR camouflage and an IR decoy system were also demonstrated. In chapter 3, we focused on the improvement of the noise-equivalent differential temperature (NEDT) of IR cameras. A temperature imaging sensitizer (TIS) was achieved based on the phase transition of $W_xV_{1-x}O_2$ and a photonic resonance cavity structure. A 15 times enhancement in the sensitivity of IR camera was verified with thermography experiments. In chapter 4, we presented a mechanically flexible, energy-free temperature-adaptive radiative coating (TARC) for smart regulation of household temperature. The TARC features a thermally driven self-switching from the radiative cooling mode at high temperatures to the keep-warm mode at low temperatures in an outdoor setting. Simulations indicated the TARC may outperform all conventional roof materials in terms of cutting energy consumption for households in most cities in the U.S. In chapter 5, we reported a scalable temperature adaptive radiative coating (STARC) which works as a TARC in terms of household temperature regulation, but can be mass produced with a roll-to-roll system. The STARC has a novel structure in which $W_xV_{1-x}O_2$ is protected from water and air as-fabricated. The color and solar absorption of STARC can be adjusted in a wide range to fulfill the needs in aesthetic and energy saving optimization. The temperature regulation performance of STARC was demonstrated by a field test with mock-up residential houses. Currently, only highly reflective metal substrates are used for the TIS and TARC system to maximize the photonic amplification of the thermal emissivity. Moreover, the metal substrates can block the thermal radiation under them, making the thermal radiation behavior of TIS and TARC independent from the mechanical supporting layer and working surface. In the future, systems with transparent or absorptive substrates will be studied for wider applications and photonic research.

6.1. Future works

6.1.1. Improvement of current devices

Engineering on VO_2 and substrate materials will benefit all the devices presented in this dissertation. For example, using more delicate control in the W doping of VO_2 will allow for finer tuning of the working temperature in various conditions. Doping with other elements like Ga or Al may shift the working temperature above that of pristine VO_2 (67°C) to realize a wider working temperature range. The response time can be improved by using thinner substrates.

For TIS, an important future direction is improving the spatial resolution. The spatial resolution can be intuitively improved by using a thinner substrate. Moreover, since the IR reflection layer of TIS is Ag, which has very high thermal conductivity, the spatial detail on the target surface will be smeared out by the strong lateral heat transfer. By changing the IR reflection layer to the Indium

Tin Oxide (ITO), the lateral heat transfer will be reduced due to the lower thermal conductivity of ITO. The ITO is transparent in visible range so the corresponding TIS will also be transparent, enabling the visible light photography during the enhanced thermography.

The smart radiative cooling application will be further developed with upgrades with STARC. The STARC inherited the emissivity ability from TARC, with scalability, durability, and lower fabrication difficulty. Tuning of the in-plane metamaterial structure can further improve the emissivity switch ability of STARC and increase the energy saving potential. Thanks to the great upgradability of the polymer-based structure, more functional layers can be integrated into STARC. For example, the energy saving ability of STARC can be further augmented with synergetic solar and thermal modulation active by an additional solar modulation layer.

6.1.2. Broader applications and research directions

The STARC can be readily applied to other systems that have surfaces facing the sky, such as tents, vehicles, clothes, space objects and mobile electronics. By changing the Al layer to ITO, transparent STARC can be fabricated for thermal regulation for greenhouses. Furthermore, temperature-adaptive radiative paints and fabrics will be developed based on the mechanism of TARC and STARC, enabling the thermal radiation modulation in broader applications.

The polymer meta-structure of STARC is a great platform for fundamental photonic research, such as metamaterials, photonic crystals, and Moiré photonics. For instance, it's easy to fabricate a Moiré photonic crystal by laminating two VO_2/PE layers with a twist angle. The possible novel phenomena observed in this photonic system may help understand the physics in photonic crystals and find wide applications in infrared sensing.

Appendix

A.1. Estimation of space-heating source energy saving (ΔS_h) and space cooling source energy saving (ΔS_c)

Rosado & Levinson [117] report for residential and commercial buildings across California and the United States gas heating (H), air conditioning (C), and fan (F) annual source energy uses in the heating, ventilation, and air conditioning (HVAC) system. Some of the fan energy is used to deliver heated air, and some is used to deliver cooled air. To calculate space heating source energy use S_h and space cooling source energy use S_c, we split annual fan source energy use into annual heating fan source energy use F_h and annual cooling source fan energy use F_c:

$$F = F_h + F_c \tag{A-1}$$

The simplest scheme is to assume that F_h is proportional to H and that F_c is proportional to C:

$$F_h = \beta_h H \tag{A-2}$$

$$F_c = \beta_c C \tag{A-3}$$

We use subscript 1 to refer to the baseline condition, such that:

$$F_{h,1} = \beta_h H_1 \tag{A-4}$$

$$F_{c,1} = \beta_c C_1 \tag{A-5}$$

$$F_1 = F_{h,1} + F_{c,1} \tag{A-6}$$

Since β_h and β_c are assumed to be constant for each building prototype (combination of building category, vintage, and location), we have similar expressions for gas heating source energy savings ΔH, air conditioning source energy savings ΔC, and fan source energy savings ΔF relative to the baseline:

$$\Delta F_h = \beta_h \Delta H \tag{A-7}$$

$$\Delta F_c = \beta_c \Delta C \tag{A-8}$$

$$\Delta F = \Delta F_h + \Delta F_c \tag{A-9}$$

Combining Equation (A-4) to (A-9) yields:

$$\beta_h = \frac{F_1 \Delta C - C_1 \Delta F}{H_1 \Delta C - C_1 \Delta H} \tag{A-10}$$

$$\beta_c = \frac{H_1 \Delta F - F_1 \Delta H}{H_1 \Delta C - C_1 \Delta H} \tag{A-11}$$

The baseline refers to the condition where ε_w=0.90 and A = 0.90, and the source energy uses are H_1, C_1, and F_1. The source energy savings ΔH, ΔC, and ΔF for conditions with other A values (0.75, 0.60, 0.40) are available in the savings database described in the Section 2.8 of Rosado & Levinson [117].

Finally, the space heating energy saving ΔS_h and space cooling energy saving ΔS_c can be calculated as:

$$\Delta S_h = \Delta H + \Delta F_h = (1 + \beta_h)\, \Delta H \tag{A-12}$$

$$\Delta S_c = \Delta C + \Delta F_c = (1 + \beta_c)\, \Delta C \tag{A-13}$$

A.2. Space-conditioning source energy savings of TARC across the U.S.

Climate zone	Location	Single-family home			Apartment building		
		Oldest (pre-1980)	Older (1980-1999)	New	Oldest (pre-1980)	Older (1980-1999)	New
1A	Miami, FL	-22.5	-6.6	-4.7	-17.5	-3.3	-2.4
2A	Houston, TX	12.4	9.5	8.6	25.1	11.9	7.18
2B	Phoenix, AZ	-2.1	9.7	8.4	24.1	22.3	22.4
3A	Memphis, TN	7.5	8.4	8.4	14.4	11.6	10.4
3B	El Paso, TX	20.2	16.4	11.3	32.7	15.0	9.0
3C	San Francisco, CA	14	4.2	2.8	10.6	2.03	1.8
4A	Baltimore, MD	22.4	8.5	4.9	21.1	8.1	3.7
4B	Albuquerque, NM	31.3	11.4	8.2	28	10.5	6.3
4C	Seattle, WA	3.1	0.83	-0.83	0.33	-2.1	-0.29
5A	Peoria, IL	14.5	5.7	4.6	13.9	5.9	3.45
5B	Boise, ID	15.1	5.6	3.9	13.7	5.0	2.14
6A	Burlington, VT	5.2	2.7	2.6	3.9	2.5	0.54
6B	Helena, MT	11.8	4.0	-0.039	10.0	1.6	-0.81
7	Duluth, MN	4.5	1.4	0.12	3.9	-0.031	-0.99
8	Fairbanks, AK	-1.0	-0.72	-2.7	-3.7	-3.4	-3.0

Table A.1. Calculated $SCSES_{min}$ as the first of merit for TARC in cities across the U.S. Units: $MJ/(m^2 \cdot y)$, where m^2 refers to the roof area.

A.3. Coefficients Used in EnergyPlus Calculation

Climate zone	Location	Oldest (pre-1980)		Older (1980-1999)		New	
		α_h	α_c	α_h	α_c	α_h	α_c
1A	Miami, FL	31.48	24.52	21.24	10.55	18.87	8.53
2A	Houston, TX	33.00	22.61	23.30	11.28	19.93	7.67
2B	Phoenix, AZ	22.55	25.56	16.48	10.64	16.23	11.34
3A	Memphis, TN	17.97	23.29	11.77	11.37	11.71	11.25
3B	El Paso, TX	20.94	22.43	17.69	10.57	13.54	7.34
3C	San Francisco, CA	28.75	26.94	21.18	9.87	13.56	6.57
4A	Baltimore, MD	26.36	30.81	13.50	12.21	9.46	7.10
4B	Albuquerque, NM	20.90	27.17	14.64	10.45	13.26	7.72
4C	Seattle, WA	17.85	11.84	11.75	4.98	8.69	3.66
5A	Peoria, IL	18.19	22.76	11.13	10.44	8.85	7.47
5B	Boise, ID	21.86	16.86	12.56	6.55	11.85	4.81
6A	Burlington, VT	13.69	14.50	11.52	8.67	8.97	7.01
6B	Helena, MT	22.47	24.02	11.97	8.98	10.19	5.53
7	Duluth, MN	17.68	19.07	10.91	7.91	8.97	7.18
8	Fairbanks, AK	14.19	15.91	8.67	6.87	8.05	5.67

Table A.2. Regressed coefficients $\boldsymbol{\alpha_h}$ and $\boldsymbol{\alpha_c}$ for single-family homes of different vintages in cities across the U.S. Units: MJ/(m^2·y·K), where m^2 refers to the roof area.

Climate zone	Location	Oldest (pre-1980)		Older (1980-1999)		New	
		α_h	α_c	α_h	α_h	α_c	α_h
1A	Miami, FL	43.99	24.37	28.93	10.34	22.30	7.93
2A	Houston, TX	44.84	21.93	27.89	10.69	22.30	6.67
2B	Phoenix, AZ	39.24	24.59	24.22	9.96	24.26	9.90
3A	Memphis, TN	21.97	22.52	13.55	10.96	12.39	9.79
3B	El Paso, TX	34.66	21.03	23.23	9.95	17.57	6.12
3C	San Francisco, CA	40.35	23.43	24.37	8.45	14.29	5.09
4A	Baltimore, MD	29.82	29.51	14.40	11.72	9.21	5.60
4B	Albuquerque, NM	30.39	25.10	16.81	9.82	14.48	6.25
4C	Seattle, WA	21.17	10.77	12.22	4.48	7.86	3.65
5A	Peoria, IL	20.75	21.85	11.31	9.60	8.29	5.87
5B	Boise, ID	26.55	15.79	13.57	6.11	11.40	3.89
6A	Burlington, VT	14.48	12.37	12.68	9.76	7.87	5.05
6B	Helena, MT	25.71	22.05	12.37	7.67	8.97	3.86
7	Duluth, MN	21.36	20.78	11.44	8.83	8.20	5.61
8	Fairbanks, AK	17.45	15.28	9.55	6.43	7.42	4.53

Table A.3. Regressed coefficients $\boldsymbol{\alpha_h}$ and $\boldsymbol{\alpha_c}$ for apartment buildings of different vintages in cities across the U.S. Units: MJ/(m^2·y·K), where m^2 refers to the roof area.

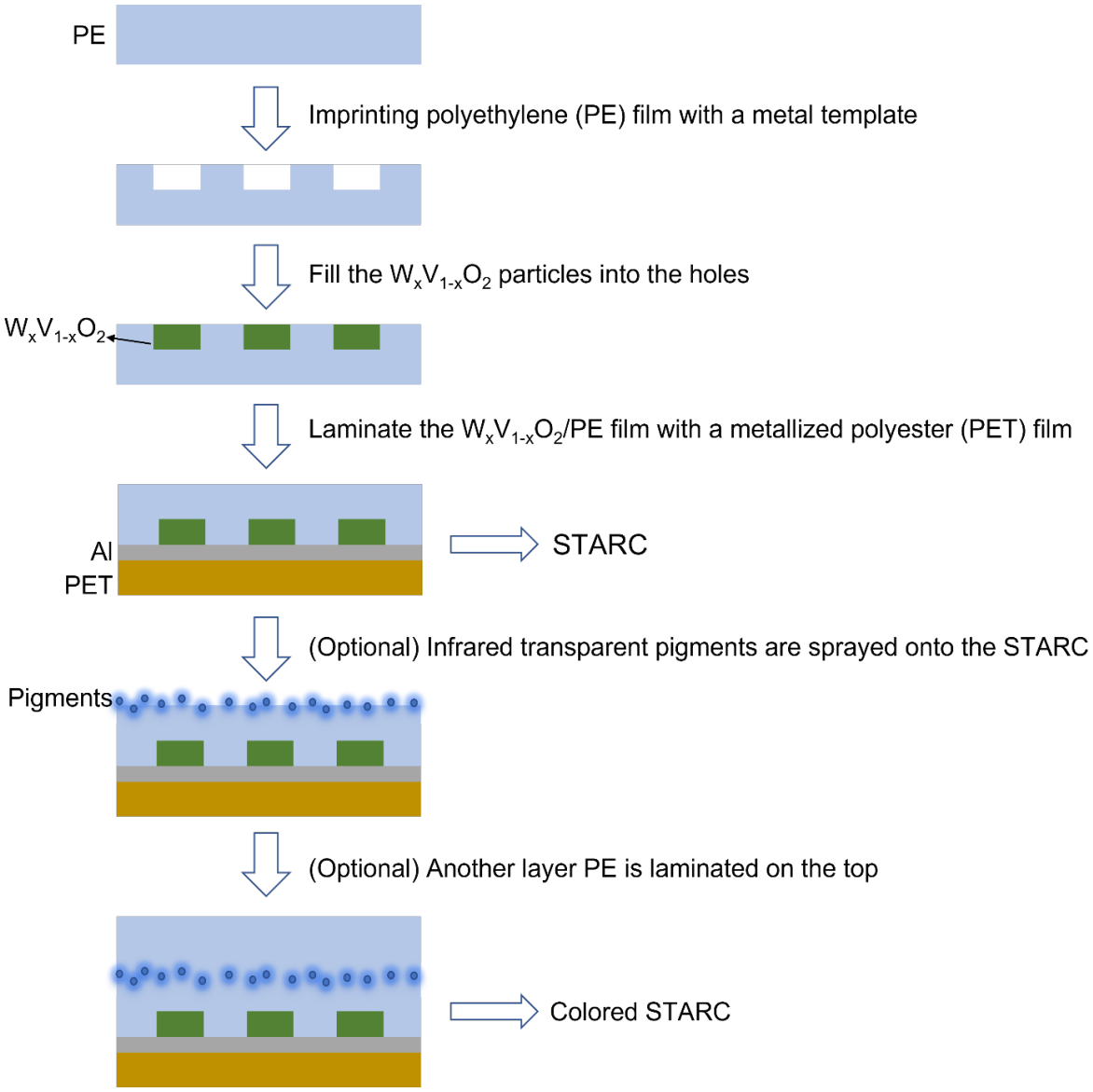
Climate zone	Location	Oldest (pre-1980)		Older (1980-1999)		New	
		β_h	β_c	β_h	β_c	β_h	β_c
1A	Miami, FL	0.000	0.219	0.000	0.216	0.000	0.282
2A	Houston, TX	0.000	0.243	0.000	0.238	0.000	0.302
2B	Phoenix, AZ	0.078	0.218	0.114	0.207	0.106	0.209
3A	Memphis, TN	0.003	0.277	0.000	0.269	0.000	0.268
3B	El Paso, TX	0.068	0.262	0.074	0.253	0.091	0.299
3C	San Francisco, CA	0.122	0.395	0.124	0.411	0.151	0.395
4A	Baltimore, MD	0.038	0.344	0.026	0.341	0.045	0.385
4B	Albuquerque, NM	0.081	0.323	0.076	0.315	0.082	0.399
4C	Seattle, WA	0.045	0.486	0.040	0.493	0.054	0.507
5A	Peoria, IL	0.025	0.380	0.017	0.375	0.028	0.438
5B	Boise, ID	0.039	0.352	0.035	0.351	0.036	0.440
6A	Burlington, VT	0.030	0.465	0.070	0.213	0.034	0.517
6B	Helena, MT	0.042	0.434	0.040	0.425	0.039	0.538
7	Duluth, MN	0.086	0.211	0.085	0.222	0.057	0.499
8	Fairbanks, AK	0.060	0.215	0.060	0.213	0.060	0.212

Table A.4. Regressed coefficients $\boldsymbol{\beta_h}$ and $\boldsymbol{\beta_c}$ (dimensionless) for single-family homes of different vintages in cities across the U.S.

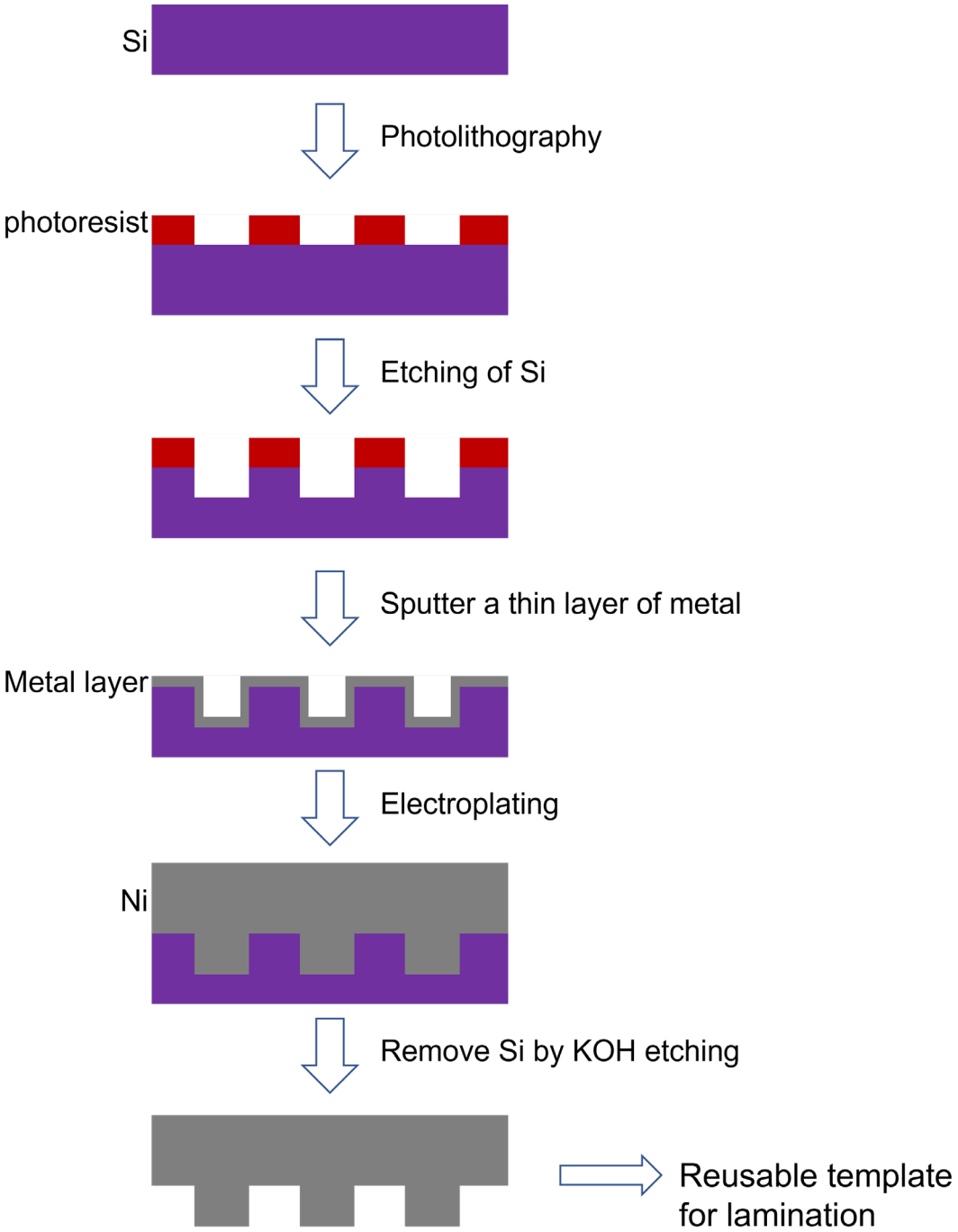
Climate zone	Location	Oldest (pre-1980)		Older (1980-1999)		New	
		β_h	β_c	β_h	β_c	β_h	β_c
1A	Miami, FL	0.000	0.210	0.000	0.186	0.000	0.261
2A	Houston, TX	0.000	0.216	0.000	0.206	0.000	0.264
2B	Phoenix, AZ	0.121	0.207	0.207	0.196	0.205	0.196
3A	Memphis, TN	0.012	0.259	0.051	0.221	0.017	0.239
3B	El Paso, TX	0.075	0.249	0.088	0.237	0.119	0.283
3C	San Francisco, CA	0.115	0.372	0.113	0.349	0.154	0.335
4A	Baltimore, MD	0.033	0.333	0.035	0.297	0.118	0.295
4B	Albuquerque, NM	0.079	0.312	0.079	0.289	0.102	0.353
4C	Seattle, WA	0.043	0.462	0.040	0.416	0.075	0.384
5A	Peoria, IL	0.035	0.348	0.042	0.297	0.089	0.310
5B	Boise, ID	0.038	0.345	0.033	0.324	0.043	0.383
6A	Burlington, VT	0.060	0.345	0.058	0.310	0.072	0.362
6B	Helena, MT	0.044	0.422	0.065	0.305	0.069	0.370
7	Duluth, MN	0.073	0.373	0.073	0.326	0.075	0.419
8	Fairbanks, AK	0.057	0.309	0.061	0.225	0.061	0.224

Table A.5. Regressed coefficients $\boldsymbol{\beta_h}$ and $\boldsymbol{\beta_c}$ (dimensionless) for apartment buildings of different vintages in cities across the U.S.

A.4. Schematic illustration of the manufacturing process for a STARC.



A.5. schematic illustration of the manufacturing process of the imprint template.



References

1. Engineering ToolBox, (2003). Emissivity Coefficients common Products. Available at: https://www.engineeringtoolbox.com/emissivity-coefficients-d_447.html
2. Thorn, R. J., & Simpson, O. C. (1953). Spectral emissivities of graphite and carbon. Journal of Applied Physics, 24(5), 633-639.
3. Satō, T. (1967). Spectral emissivity of silicon. Japanese Journal of Applied Physics, 6(3), 339.
4. Sully, A. H., Brandes, E. A., & Waterhouse, R. B. (1952). Some measurements of the total emissivity of metals and pure refractory oxides and the variation of emissivity with temperature. British Journal of Applied Physics, 3(3), 97.
5. Mandal, J., Fu, Y., Overvig, A. C., Jia, M., Sun, K., Shi, N. N., ... & Yang, Y. (2018). Hierarchically porous polymer coatings for highly efficient passive daytime radiative cooling. Science, 362(6412), 315-319.
6. Zhai, Y., Ma, Y., David, S. N., Zhao, D., Lou, R., Tan, G., ... & Yin, X. (2017). Scalable-manufactured randomized glass-polymer hybrid metamaterial for daytime radiative cooling. Science, 355(6329), 1062-1066.
7. Li, T., Zhai, Y., He, S., Gan, W., Wei, Z., Heidarinejad, M., ... & Hu, L. (2019). A radiative cooling structural material. Science, 364(6442), 760-763.
8. Rawat, M., & Singh, R. N. (2021). A study on the comparative review of cool roof thermal performance in various regions. Energy and Built Environment.
9. Tang, K., Dong, K., Nicolai, C. J., Li, Y., Li, J., Lou, S., ... & Wu, J. (2020). Millikelvin-resolved ambient thermography. Science advances, 6(50), eabd8688.
10. Tang, K., Wang, X., Dong, K., Li, Y., Li, J., Sun, B., ... & Wu, J. (2020). A thermal radiation modulation platform by emissivity engineering with graded metal–insulator transition. Advanced materials, 32(36), 1907071.
11. Qu, Y., Li, Q., Cai, L., Pan, M., Ghosh, P., Du, K., & Qiu, M. (2018). Thermal camouflage based on the phase-changing material GST. Light: Science & Applications, 7(1), 1-10.
12. Dong, K., Tseng, D., Li, J., Warkander, S., Yao, J., & Wu, J. (2022). Reducing temperature swing of space objects with temperature-adaptive solar or radiative coating. Cell Reports Physical Science, 3(10), 101066.

13. Tang, K., Dong, K., Li, J., Gordon, M. P., Reichertz, F. G., Kim, H., ... & Wu, J. (2021). Temperature-adaptive radiative coating for all-season household thermal regulation. Science, 374(6574), 1504-1509.
14. Wang, S., Jiang, T., Meng, Y., Yang, R., Tan, G., & Long, Y. (2021). Scalable thermochromic smart windows with passive radiative cooling regulation. Science, 374(6574), 1501-1504.
15. Whittaker, L., Patridge, C. J., & Banerjee, S. (2011). Microscopic and nanoscale perspective of the metal−insulator phase transitions of VO2: some new twists to an old tale. The Journal of Physical Chemistry Letters, 2(7), 745-758.
16. Kim, H., Cheung, K., Auyeung, R. C., Wilson, D. E., Charipar, K. M., Piqué, A., & Charipar, N. A. (2019). VO2-based switchable radiator for spacecraft thermal control. Scientific reports, 9(1), 1-8.
17. Lee, S., Hippalgaonkar, K., Yang, F., Hong, J., Ko, C., Suh, J., ... & Wu, J. (2017). Anomalously low electronic thermal conductivity in metallic vanadium dioxide. Science, 355(6323), 371-374.
18. Qazilbash, M. M., Brehm, M., Andreev, G. O., Frenzel, A., Ho, P. C., Chae, B. G., ... & Basov, D. N. (2009). Infrared spectroscopy and nano-imaging of the insulator-to-metal transition in vanadium dioxide. Physical Review B, 79(7), 075107.
19. Putley, E. H. (1973). Modern infrared detectors. Physics in Technology, 4(3), 202.
20. Tran, C. D. (2005). Principles, instrumentation, and applications of infrared multispectral imaging, an overview. Analytical letters, 38(5), 735-752.
21. Liu, X., & Padilla, W. J. (2016). Thermochromic infrared metamaterials. Advanced Materials, 28(5), 871-875.
22. Xiao, L., Ma, H., Liu, J., Zhao, W., Jia, Y., Zhao, Q., ... & Jiang, K. (2015). Fast adaptive thermal camouflage based on flexible VO2/graphene/CNT thin films. Nano letters, 15(12), 8365-8370.
23. Ji, H., Liu, D., Cheng, H., Zhang, C., Yang, L., & Ren, D. (2017). Infrared thermochromic properties of monoclinic VO 2 nanopowders using a malic acid-assisted hydrothermal method for adaptive camouflage. RSC advances, 7(9), 5189-5194.

24. Chandrasekhar, P., Zay, B. J., Birur, G. C., Rawal, S., Pierson, E. A., Kauder, L., & Swanson, T. (2002). Large, switchable electrochromism in the visible through far-infrared in conducting polymer devices. Advanced Functional Materials, 12(2), 95-103.
25. Salihoglu, O., Uzlu, H. B., Yakar, O., Aas, S., Balci, O., Kakenov, N., ... & Kocabas, C. (2018). Graphene-based adaptive thermal camouflage. Nano letters, 18(7), 4541-4548.
26. Kim, B., Koh, J. K., Park, J., Ahn, C., Ahn, J., Kim, J. H., & Jeon, S. (2015). Patternable PEDOT nanofilms with grid electrodes for transparent electrochromic devices targeting thermal camouflage. Nano convergence, 2(1), 1-7.
27. Park, J., Kang, J. H., Liu, X., Maddox, S. J., Tang, K., McIntyre, P. C., ... & Brongersma, M. L. (2018). Dynamic thermal emission control with InAs-based plasmonic metasurfaces. Science advances, 4(12), eaat3163.
28. Coppens, Z. J. (2017). Electromagnetic Metamaterials for Controlling Absorption and Thermal Emission (Doctoral dissertation).
29. Xu, C., Stiubianu, G. T., & Gorodetsky, A. A. (2018). Adaptive infrared-reflecting systems inspired by cephalopods. Science, 359(6383), 1495-1500.
30. Li, X., Yang, L., Zhang, S., Li, X., Chen, J., & Huang, C. (2018). VO2 (M) with narrow hysteresis width from a new metastable phase of crystallized VO2 (M)· 0.25 H2O. Materials Letters, 211, 308-311.
31. Chen, S., Liu, J., Wang, L., Luo, H., & Gao, Y. (2014). Unraveling mechanism on reducing thermal hysteresis width of VO2 by Ti doping: a joint experimental and theoretical study. The Journal of Physical Chemistry C, 118(33), 18938-18944.
32. Mounier, E. (2011, May). Technical and market trends for microbolometers for thermography and night vision. In Infrared Technology and Applications XXXVII (Vol. 8012, pp. 599-604). SPIE.
33. Rozlosnik, A. E. (2000, March). Bringing up-to-date applications of infrared thermography to surveillance, safety, and rescue. In Thermosense XXII (Vol. 4020, pp. 387-405). SPIE.
34. Lu, X., Liao, G., Zha, Z., Xia, Q., & Shi, T. (2011). A novel approach for flip chip solder joint inspection based on pulsed phase thermography. Ndt & E International, 44(6), 484-489.
35. Lahiri, B. B., Bagavathiappan, S., Jayakumar, T., & Philip, J. (2012). Medical applications of infrared thermography: a review. Infrared Physics & Technology, 55(4), 221-235.

36. Cheng, C. C., Cheng, T. M., & Chiang, C. H. (2008). Defect detection of concrete structures using both infrared thermography and elastic waves. Automation in Construction, 18(1), 87-92.
37. Mouillet, V., Lamontagne, J., Durrieu, F., Planche, J. P., & Lapalu, L. (2008). Infrared microscopy investigation of oxidation and phase evolution in bitumen modified with polymers. Fuel, 87(7), 1270-1280.
38. Voshell, A., Dhar, N., & Rana, M. M. (2017). Materials for microbolometers: vanadium oxide or silicon derivatives. Image Sensing Technologies: Materials, Devices, Systems, and Applications IV, 10209, 92-107.
39. Li, C., Skidmore, G. D., Howard, C., Han, C. J., Wood, L., Peysha, D., ... & Clarke, E. (2007, May). Recent development of ultra small pixel uncooled focal plane arrays at DRS. In Infrared Technology and Applications XXXIII (Vol. 6542, pp. 691-702). SPIE.
40. Kohin, M., & Butler, N. R. (2004, August). Performance limits of uncooled VOx microbolometer focal plane arrays. In Infrared Technology and Applications XXX (Vol. 5406, pp. 447-453). SPIE.
41. Niklaus, F., Vieider, C., & Jakobsen, H. (2008). MEMS-based uncooled infrared bolometer arrays: a review. MEMS/MOEMS technologies and applications III, 6836, 125-139.
42. Rogalski, A. (2017, October). Next decade in infrared detectors. In Electro-Optical and Infrared Systems: Technology and Applications XIV (Vol. 10433, pp. 128-152). SPIE.
43. Kandlikar, S. G., Perez-Raya, I., Raghupathi, P. A., Gonzalez-Hernandez, J. L., Dabydeen, D., Medeiros, L., & Phatak, P. (2017). Infrared imaging technology for breast cancer detection–Current status, protocols and new directions. International Journal of Heat and Mass Transfer, 108, 2303-2320.
44. Skidmore, G. D., Han, C. J., & Li, C. (2014, May). Uncooled microbolometers at DRS and elsewhere through 2013. In Image Sensing Technologies: Materials, Devices, Systems, and Applications (Vol. 9100, p. 910003). SPIE.
45. Schacht, R., Wunderle, B., May, D., Ras, M. A., Faust, W., Michel, B., & Reichl, H. (2008, September). Effective thermal modelling evaluation and non-destructive tests for thermal via-structures in organic multi layer PCBs. In 2008 2nd Electronics System-Integration Technology Conference (pp. 999-1008). IEEE.

46. A. Gupta, L. Yongmei, N. Zamora, T. Paddock, paper presented at the Thermal and Thermomechanical Proceedings 10th Intersociety Conference on Phenomena in Electronics Systems, San Diego, CA, USA, 30 May to 2 June 2006
47. D. May, B. Wunderle, R. Schacht, B. Michel, paper presented at 2012 13th International Thermal, Mechanical and Multi-Physics Simulation and Experiments in Microelectronics and Microsystems, Cascais, Portugal, 16 to 18 April 2012.
48. A. Stoynova, B. Bonev, N. Brayanov, paper presented at the 2018 41st International Spring Seminar on Electronics Technology (ISSE). Zlatibor, Serbia, 16 to 20 May 2018.
49. Breitenstein, O., & Langenkamp, M. (1998). Lock-in contact thermography investigation of lateral electronic inhomogeneities in semiconductor devices. Sensors and Actuators A: Physical, 71(1-2), 46-50.
50. Boudenne, A., Ibos, L., Fois, M., Majesté, J. C., & Géhin, E. (2005). Electrical and thermal behavior of polypropylene filled with copper particles. Composites Part A: Applied Science and Manufacturing, 36(11), 1545-1554.
51. Chen, X., An, M., Guo, R., Tang, N., Peng, Z., Feng, H., ... & Yang, N. (2017). Enhancement of thermal conductivity of polyvinyl alcohol membrane using nano-fiber. MRS Advances, 2(58-59), 3651-3656.
52. Chung, S. L., & Lin, J. S. (2016). Thermal conductivity of epoxy resin composites filled with combustion synthesized h-BN particles. Molecules, 21(5), 670.
53. Li, Y., Zhu, K. J., Peng, Y. G., Li, W., Yang, T., Xu, H. X., ... & Qiu, C. W. (2019). Thermal meta-device in analogue of zero-index photonics. Nature materials, 18(1), 48-54.
54. Sarvar, F., Poole, N. J., & Witting, P. A. (1990). PCB glass-fibre laminates: Thermal conductivity measurements and their effect on simulation. Journal of electronic materials, 19(12), 1345-1350.
55. Kim, T., Choi, B. I., Han, Y. S., & Do, K. H. (2019). Feasibility study of long-wave infrared thermometry technique for simultaneous temperature and heat flux measurement. High Temperatures--High Pressures, 48.
56. Cabrera, R., Merced, E., & Sepúlveda, N. (2013). Performance of electro-thermally driven VO_2-based MEMS actuators. Journal of microelectromechanical systems, 23(1), 243-251.
57. Bourgoin, J. P., Allogho, G. G., & Haché, A. (2010). Thermal conduction in thin films measured by optical surface thermal lensing. Journal of Applied Physics, 108(7), 073520.

58. Ng, E. Y. K., & Kee, E. C. (2008). Advanced integrated technique in breast cancer thermography. Journal of medical engineering & technology, 32(2), 103-114.
59. Lahiri, B. B., Bagavathiappan, S., Raj, B., & Philip, J. (2017). Infrared thermography for detection of diabetic neuropathy and vascular disorder. In Application of Infrared to Biomedical Sciences (pp. 217-247). Springer, Singapore.
60. Bitar, D., Goubar, A., & Desenclos, J. C. (2009). International travels and fever screening during epidemics: a literature review on the effectiveness and potential use of non-contact infrared thermometers. Eurosurveillance, 14(6), 19115.
61. Fikackova, H., & Ekberg, E. (2004). Can infrared thermography be a diagnostic tool for arthralgia of the temporomandibular joint?. Oral Surgery, Oral Medicine, Oral Pathology, Oral Radiology, and Endodontology, 98(6), 643-650.
62. John, H. E., Niumsawatt, V., Rozen, W. M., & Whitaker, I. S. (2016). Clinical applications of dynamic infrared thermography in plastic surgery: a systematic review. Gland surgery, 5(2), 122.
63. Arora, N., Martins, D., Ruggerio, D., Tousimis, E., Swistel, A. J., Osborne, M. P., & Simmons, R. M. (2008). Effectiveness of a noninvasive digital infrared thermal imaging system in the detection of breast cancer. The American Journal of Surgery, 196(4), 523-526.
64. Kandlikar, S. G., Perez-Raya, I., Raghupathi, P. A., Gonzalez-Hernandez, J. L., Dabydeen, D., Medeiros, L., & Phatak, P. (2017). Infrared imaging technology for breast cancer detection–Current status, protocols and new directions. International Journal of Heat and Mass Transfer, 108, 2303-2320.
65. Ng, E. Y. K., & Sudharsan, N. M. (2001). Numerical computation as a tool to aid thermographic interpretation. Journal of medical engineering & technology, 25(2), 53-60.
66. Urakov, A. L., Kasatkin, A. A., & Urakova, N. A. (2017). Change in local temperature of venous blood and venous vessel walls as a basis for imaging superficial veins during infrared phlebography using temperature-induced tissue contrasting. In Application of Infrared to Biomedical Sciences (pp. 429-436). Springer, Singapore.
67. De Cesaris, R., Grimaldi, A., Balestrazzi, M., Ranieri, G., Chiarappa, R., & Avantaggiato, F. (1985). Changes in blood pressure and thermographic values resulting from use of a

beta-blocker plus diuretic and of an alpha-beta-blocker plus diuretic. Drugs under experimental and clinical research, 11(10), 725-729.

68. Bagavathiappan, S., Saravanan, T., Philip, J., Jayakumar, T., Raj, B., Karunanithi, R., ... & Jagadeesan, K. (2009). Infrared thermal imaging for detection of peripheral vascular disorders. Journal of medical physics, 34(1), 43.

69. Flores, B., Susarrey, O., Yoguez, A., Gutiérrez, C., & Jiménez, J. (2017). Preliminary study on the evaluation of musculoskeletal risk of static-cycling instructors using infrared thermography. In Advances in Ergonomics Modeling, Usability & Special Populations (pp. 567-574). Springer, Cham.

70. Cherkas, L. F., Carter, L., Spector, T. D., Howell, K. J., Black, C. M., & MacGregor, A. J. (2003). Use of thermographic criteria to identify Raynaud's phenomenon in a population setting. The Journal of rheumatology, 30(4), 720-722.

71. Di Carlo, A. (1995). Thermography and the possibilities for its applications in clinical and experimental dermatology. Clinics in dermatology, 13(4), 329-336.

72. Kopsa, H., Czech, W., Schmidt, P., Zazgornik, J., Pils, P., & Balcke, P. (1979). Use of thermography in kidney transplantation: two year follow up study in 75 cases. Proceedings of the European Dialysis and Transplant Association. European Dialysis and Transplant Association, 16, 383-387.

73. Dolensek, N., Gehrlach, D. A., Klein, A. S., & Gogolla, N. (2020). Facial expressions of emotion states and their neuronal correlates in mice. Science, 368(6486), 89-94.

74. Bauer, E., Pavón, E., Oliveira, E., & Pereira, C. H. (2016). Facades inspection with infrared thermography: cracks evaluation. Journal of Building Pathology and Rehabilitation, 1(1), 1-7.

75. US Energy Information Administration. (2020). Annual Energy Review 2020. https://www.eia.gov/totalenergy/data/annual/

76. US Energy Information Administration. (2015). 2015 Residential Energy Consumption Survey. https://www.eia.gov/consumption/residential/

77. Gentle, A. R., & Smith, G. B. (2015). A subambient open roof surface under the Mid-Summer sun. Advanced Science, 2(9), 1500119.

78. Dong, M., Chen, N., Zhao, X., Fan, S., & Chen, Z. (2019). Nighttime radiative cooling in hot and humid climates. Optics Express, 27(22), 31587-31598.

79. Orel, B., Gunde, M. K., & Krainer, A. (1993). Radiative cooling efficiency of white pigmented paints. Solar energy, 50(6), 477-482.
80. Berdahl, P., Martin, M., & Sakkal, F. (1983). Performances thermiques des panneaux a refroidissement radiatif. Int J Heat Mass Transf, 26(6), 871-880.
81. Shi, N. N., Tsai, C. C., Camino, F., Bernard, G. D., Yu, N., & Wehner, R. (2015). Keeping cool: Enhanced optical reflection and radiative heat dissipation in Saharan silver ants. Science, 349(6245), 298-301.
82. Kou, J. L., Jurado, Z., Chen, Z., Fan, S., & Minnich, A. J. (2017). Daytime radiative cooling using near-black infrared emitters. Acs Photonics, 4(3), 626-630.
83. Zhai, Y., Ma, Y., David, S. N., Zhao, D., Lou, R., Tan, G., ... & Yin, X. (2017). Scalable-manufactured randomized glass-polymer hybrid metamaterial for daytime radiative cooling. Science, 355(6329), 1062-1066.
84. Mandal, J., Fu, Y., Overvig, A. C., Jia, M., Sun, K., Shi, N. N., ... & Yang, Y. (2018). Hierarchically porous polymer coatings for highly efficient passive daytime radiative cooling. Science, 362(6412), 315-319.
85. Li, T., Zhai, Y., He, S., Gan, W., Wei, Z., Heidarinejad, M., ... & Hu, L. (2019). A radiative cooling structural material. Science, 364(6442), 760-763.
86. Li, Z., Chen, Q., Song, Y., Zhu, B., & Zhu, J. (2020). Fundamentals, materials, and applications for daytime radiative cooling. Advanced Materials Technologies, 5(5), 1901007.
87. Berdahl, P. (1984). Radiative cooling with MgO and/or LiF layers. Applied optics, 23(3), 370-372.
88. Li, X., Peoples, J., Huang, Z., Zhao, Z., Qiu, J., & Ruan, X. (2020). Full daytime sub-ambient radiative cooling in commercial-like paints with high figure of merit. Cell Reports Physical Science, 1(10), 100221.
89. National Oceanic and Atmospheric Administration. (2019). The Atmospheric Window. https://www.weather.gov/jetstream/absorb
90. Ulpiani, G., Ranzi, G., Shah, K. W., Feng, J., & Santamouris, M. (2020). On the energy modulation of daytime radiative coolers: A review on infrared emissivity dynamic switch against overcooling. Solar Energy, 209, 278-301.

91. Goncharov, K., Orlov, A., Tarabrin, A., Gottero, M., Perotto, V., Tavera, S., & Zoppo, G. P. (2001). 1500 W deployable radiator with loop heat pipe. SAE Technical Papers.
92. Lashley, C., Krein, S., & Barcomb, P. (1998). Deployable radiators-A multi-discipline approach (No. 981691). SAE Technical Paper.
93. Zhao, H., Sun, Q., Zhou, J., Deng, X., & Cui, J. (2020). Switchable cavitation in silicone coatings for energy-saving cooling and heating. Advanced Materials, 32(29), 2000870.
94. Xia, Z., Fang, Z., Zhang, Z., Shi, K., & Meng, Z. (2020). Easy way to achieve self-adaptive cooling of passive radiative materials. ACS applied materials & interfaces, 12(24), 27241-27248.
95. Nagano, H., Nagasaka, Y., & Ohnishi, A. (2006). Simple deployable radiator with autonomous thermal control function. Journal of thermophysics and heat transfer, 20(4), 856-864.
96. Ono, M., Chen, K., Li, W., & Fan, S. (2018). Self-adaptive radiative cooling based on phase change materials. Optics express, 26(18), A777-A787.
97. Chen, M., Morsy, A. M., & Povinelli, M. L. (2019). Design of VO 2-coated silicon microspheres for thermally-regulating paint. Optics Express, 27(15), 21787-21793.
98. Taylor, S., Yang, Y., & Wang, L. (2017). Vanadium dioxide based Fabry-Perot emitter for dynamic radiative cooling applications. Journal of Quantitative Spectroscopy and Radiative Transfer, 197, 76-83.
99. Zhang, W. W., Qi, H., Sun, A. T., Ren, Y. T., & Shi, J. W. (2020). Periodic trapezoidal VO 2-Ge multilayer absorber for dynamic radiative cooling. Optics Express, 28(14), 20609-20623.
100. Ito, K., Watari, T., Nishikawa, K., Yoshimoto, H., & Iizuka, H. (2018). Inverting the thermal radiative contrast of vanadium dioxide by metasurfaces based on localized gap-plasmons. Apl Photonics, 3(8), 086101.
101. Nishikawa, K., Yatsugi, K., Kishida, Y., & Ito, K. (2019). Temperature-selective emitter. Applied Physics Letters, 114(21), 211104.
102. Sun, K., Riedel, C. A., Urbani, A., Simeoni, M., Mengali, S., Zalkovskij, M., ... & Muskens, O. L. (2018). VO2 thermochromic metamaterial-based smart optical solar reflector. ACS photonics, 5(6), 2280-2286.

103. Xue, X., Qiu, M., Li, Y., Zhang, Q. M., Li, S., Yang, Z., ... & Fan, S. (2020). Creating an eco-friendly building coating with smart subambient radiative cooling. Advanced Materials, 32(42), 1906751.

104. Morin, F. J. (1959). Oxides which show a metal-to-insulator transition at the Neel temperature. Physical review letters, 3(1), 34.

105. Wu, T. L., Whittaker, L., Banerjee, S., & Sambandamurthy, G. (2011). Temperature and voltage driven tunable metal-insulator transition in individual W x V 1− x O 2 nanowires. Physical Review B, 83(7), 073101.

106. Kim, C., Shin, J. S., & Ozaki, H. (2007). Effect of W doping in metal–insulator transition material VO2 by tunnelling spectroscopy. Journal of Physics: Condensed Matter, 19(9), 096007.

107. Barker Jr, A. S., Verleur, H. W., & Guggenheim, H. J. (1966). Infrared optical properties of vanadium dioxide above and below the transition temperature. Physical Review Letters, 17(26), 1286.

108. Ordal, M. A., Long, L. L., Bell, R. J., Bell, S. E., Bell, R. R., Alexander, R. W., & Ward, C. A. (1983). Optical properties of the metals Al, Co, Cu, Au, Fe, Pb, Ni, Pd, Pt, Ag, Ti, and W in the infrared and far infrared. Applied optics, 22(7), 1099-1119.

109. Dong, K., Hong, S., Deng, Y., Ma, H., Li, J., Wang, X., ... & Wu, J. (2018). A Lithography-Free and Field-Programmable Photonic Metacanvas. Advanced Materials, 30(5), 1703878.

110. Qazilbash, M. M., Brehm, M., Andreev, G. O., Frenzel, A., Ho, P. C., Chae, B. G., ... & Basov, D. N. (2009). Infrared spectroscopy and nano-imaging of the insulator-to-metal transition in vanadium dioxide. Physical Review B, 79(7), 075107.

111. Querry, M. R. (1998). Optical constants of minerals and other materials from the millimeter to the ultraviolet. Chemical Research, Development & Engineering Center, US Army Armament Munitions Chemical Command.

112. Johnson, P. B., & Christy, R. W. (1972). Optical constants of the noble metals. Physical review B, 6(12), 4370.

113. Kana, J. K., Vignaud, G., Gibaud, A., & Maaza, M. (2016). Thermally driven sign switch of static dielectric constant of VO2 thin film. Optical Materials, 54, 165-169.

114. Meitav, N., Ribak, E. N., & Shoham, S. (2016). Point spread function estimation from projected speckle illumination. Light: Science & Applications, 5(3), e16048-e16048.

115. Incropera, F. P., DeWitt, D. P., Bergman, T. L., & Lavine, A. S. (1996). Fundamentals of heat and mass transfer (Vol. 6, p. 116). New York: Wiley.
116. U.S. Department of Energy. EnergyPlus Weather Data. Downloaded from <https://energyplus.net/weather>.
117. Rosado, P. J., & Levinson, R. (2019). Potential benefits of cool walls on residential and commercial buildings across California and the United States: Conserving energy, saving money, and reducing emission of greenhouse gases and air pollutants. Energy and Buildings, 199, 588-607.
118. Qin, Y., & Hiller, J. E. (2013). Ways of formulating wind speed in heat convection significantly influencing pavement temperature prediction. Heat and Mass Transfer, 49(5), 745-752.
119. Zhao, D., Aili, A., Zhai, Y., Xu, S., Tan, G., Yin, X., & Yang, R. (2019). Radiative sky cooling: Fundamental principles, materials, and applications. Applied Physics Reviews, 6(2), 021306.
120. Jiji, L. M., & Jiji, L. M. (2006). Heat convection (p. 434). Berlin: Springer.
121. Tang, R., Etzion, Y., & Meir, I. A. (2004). Estimates of clear night sky emissivity in the Negev Highlands, Israel. Energy conversion and management, 45(11-12), 1831-1843.
122. Skartveit, A., Olseth, J. A., Czeplak, G., & Rommel, M. (1996). On the estimation of atmospheric radiation from surface meteorological data. Solar Energy, 56(4), 349-359.
123. Energy Information Administration, Forms EIA-457A and EIA-457C of the 2015 Residential Energy Consumption Survey, Table HC2.1: Structural and Geographic Characteristics of U.S. Homes by Housing Unit Type, 2015. Available at: https://www.eia.gov/consumption/residential/data/2015/hc/php/hc2.1.php
124. Guo, J., Xu, G., Tian, D., Qu, Z., & Qiu, C. W. (2022). A Real‐Time Self‐Adaptive Thermal Metasurface. Advanced Materials, 2201093.